Strategies of anomalies detection in bridges and tunnels as a tool for structural health management. New approaches and AI support.

Original
Strategies of anomalies detection in bridges and tunnels as a tool for structural health management. New approaches and AI support / Marasco, Giulia. - (2022 Nov 11), pp. 1-201.

Publisher:
Politecnico di Torino

Published
DOI:

Doctoral Dissertation
Doctoral Program in Civil and Environmental Engineering (34^{th}cycle)

Strategies of anomalies detection in bridges and tunnels as a tool for structural health management

New approaches and AI support

By

Giulia Marasco

******

Supervisor(s):
Prof. Bernardino Chiaia, Supervisor
Prof. Giulio Ventura, Co-Supervisor

Doctoral Examination Committee:
Marzia Malavisi, PhD, Referee, Movyon SpA, Italy
Marco Vannucci, PhD, Referee, Scuola Superiore Sant'Anna- Istituto TeCIP, Italy
Prof. Raimondo Betti, Columbia University, USA
Prof. Eloi Figueiredo, Lusofóna University, Portugal
Prof. Giuseppe Carlo Marano, Politecnico di Torino, Italy
Prof. Achille Paolone, Sapienza Università di Roma, Italy

Politecnico di Torino
2022

Declaration

I hereby declare that, the contents and organization of this dissertation constitute my own original work and does not compromise in any way the rights of third parties, including those relating to the security of personal data.

Giulia Marasco
2022

* This dissertation is presented in partial fulfillment of the requirements for **Ph.D. degree** in the Graduate School of Politecnico di Torino (ScuDo).

Abstract

The control of structural condition of civil infrastructure facilities, such as bridges and tunnels, is crucial to ensure safety and to shun grave waste of economic resources. The consequences of their degradation could have a substantial impact given the crucial role that them play in the nowadays society. The development of Structural Health Monitoring (*SHM*) strategies, aimed at identifying, localizing, and estimating the severity of potential damages for a successful decision-making process in infrastructures maintenance management, has become a research topic in the last twenty years. Significant resources have been allocated, mainly in developed countries, where the infrastructure assets are composed of facilities nearing the end of their useful life and, as a result, require more attention due to aging. Nowadays, advanced studies, exploiting even highly sophisticated artificial intelligence algorithms, have been carried out to structural conditions assessment. However, many issues need to be still addressed due to the difficulty of integrating expertise from many engineering sectors and achieving rigorous validation methodologies on real-world case studies.

This thesis aims at designing and validating methodologies for the control of large-scale infrastructures, considering the features and issues of the typology to which they belong, to obtain reliable information about the current structural state and predict its evolution.

Several methodologies have been devised based on infrastructural typology, construction material, and static scheme. Such features are directly related to the structural response and to specific issues that need customized strategies to be successfully coped. The analyses, involving both numerical simulations and real case studies, have been based on several data types (e.g., static and/or dynamic parameters, images) and different monitoring typologies (i.e., continuous or periodic monitoring). In detail, customized strategies have been drawn for highway tunnels and for bridges belonging to three service classes (highway, railway, and pedestrian).

As regard the tunnel, a multi-level assessment strategy has been proposed. It exploits the high capacity of Convolutional Neural Networks (*CNNs*) to classify potential damages. Ground Penetrating Radar (*GPR*) profiles and the associated structural phenomena have been used as input and output to train and test such networks. Image-based analysis and integrative investigations have been leveraged to define the structural conditions linked to *GPR* profiles and to generate the database. The degree of detail and attained accuracy are high. As a result, this method is useful to reduce the amount and invasiveness of testing, as well as the time and cost associated with highly qualified technicians.

As regard the bridges, unsupervised and supervised approaches have been applied. As concerns the structural condition assessment of an arch highway steel bridge, methodologies mainly based on dynamic behavior have been devised and a clustering based approach has been proposed as artificial intelligence (*AI*) support. On the other hand, plans for control of simply supported prestressed concrete railway bridges have been drawn up by means of two anomaly detection methodologies developed to be complementary and economically sustainable. The first, designed for a continuous control over time, is based on regression correlation models exploting supervised algorithm; the second, devised for a periodic control, combines the use of influence lines, genetic algorithm, and neural network. Further efforts have been made to validate strategies, based on transfer learning concept, suitable for the evaluation of bridge structure which are structural similar and replicated extensively, like pedestrian bridges in high-density cities.

The use of machine learning algorithms turned out to be of paramount importance to support all the proposed approaches to obtain highly accurate and automated solutions.

Contents

List of Figures

List of Tables

Chapter 1

Introduction

1.1 Structural Health Monitoring aided by Big Data and Artificial Intelligence

In recent decades, Structural Health Monitoring (*SHM*) strategies have been proposed to address the need for infrastructure asset control. According to several researchers, the main aims of such procedures are damage detection and structural condition assessment. [1–3].

Similar to the human body, which can be affected by diseases throughout one's life, facilities are complex systems that can degrade over time. Owing to deterioration processes, an infrastructure asset is always changing. Structural damage is usually described as a variation in the geometric or material features, boundary conditions, and element connectivity that has a negative impact on structural performance, safety, and reliability [4, 5]. It does not always represent a complete failure, but rather poor performance [6–8] that can lead to the failure state if no remedial action is performed. The type of damage determine the collapse mode. It can be gradual or abrupt [3, 9]. For example, corrosion and fatigue failures often are the result of a long process, whereas earthquakes and fire-induced damage can cause a complete collapse in a short period of time [10]. Human-induced and environmental factors [11, 12] make engineering structures, especially large-scale ones such as bridges and tunnels, more vulnerable to damage accumulation and propagation, reducing the structural life cycle [13].

By detecting, locating, and evaluating the extension of damage is possible to assess the remaining service life of the structure and develop a plan to increase it through maintenance. Structured data has substantial benefits in mitigating the risk of human and economic losses. De Sitter's "Law of Five" estimates the devastating impact of a lack of maintenance on overall costs [14].

Visual inspection has traditionally been used to discover defects on structure surfaces and analyze structural condition. Nevertheless, even for well-trained inspectors, visual examination is labor-intensive, time-consuming, and subjective, making it impossible to track condition changes in real time. To address the problem, *SHM* strategies have been developed and proposed in recent decades

SHM techniques can be divided into three categories based on the control time duration. The first is continuous monitoring, which points out changes in the global structural behaviour. The second consists of non-destructive periodic testing (*NDT*), which allows for structural local investigation. The third is accomplished by spot tests. Accurate results, reduced false and missed alarms, and shorter times to damage detection (*DT*) are all important features of strategies that have a positive impact from both an economic and safety standpoint. Early warnings of anomalies are critical for *SHM* techniques to allow for adequate prognostics and health management development (*PHM*). *SHM* has applications in mechanical, aeronautical, and civil engineering, and it needs synergy between several engineering sectors. Operational evaluation, data collecting, feature extraction, and statistical model creation are four procedures that can describe an *SHM* process [3]. Starting with the problem definition, the type and position of the sensors used to collect data are fundamental. This allows for the extraction of useful structural properties, such as those that are sensitive to possible damage. Then, to intercept and quantify the damage, statistical models are required.

Algorithms have been integrated into the *SHM* framework in the last decades owing to their capacity to analyze data and perform a real-time assessment for decision making [15]. Big data (*BD*) and artificial intelligence (*AI*) are two promising tools for a successful data interpretation and structural evaluation [16].

John Mashey coined the word "big data" in a speech in 1998 [17]. Ward and Barker later defined it as follows: “Big data is a term describing the storage and analysis of large and or complex data sets using a series of techniques including, but not limited to: NoSQL, MapReduce and machine learning" [18]. Big data analysis is the act of handling an exceptionally large dataset for any type of computing across several storage devices with independent processor units.

Artificial intelligence refers to an algorithm or intelligent agent that interprets data in order to take actions. John McCarthy coined the term in 1956 [19], and it has since spawned lots of new technologies, including computer vision, natural language processing, machine learning, and robotics. More in detail, *AI* is a branch of computer science that aims to create machines that solve problems and perform activities with human-like intelligence. The early uses of *AI* mostly focused on rule-based problems. Initially, this technique was only used to tackle rule-based issues successfully [20]. Although addressing the latter proven to be a useful aid in speeding up and standardizing some of the tasks previously handled by humans, the main challenge nowadays is to transfer common sense knowledge to modern *AI* systems so that they can solve problems that cannot be solved through rule coding simply [21]. In the broad field of artificial intelligence, the concepts of machine learning (*ML*) and deep learning (*DL*) have been introduced to successfully address and solve challenges connected to the knowledge-based approach. It allows for the acquisition of knowledge through training based on a large amount of data [22], avoiding explicit programming [23]. Owing their higher performance in a damage detection scenario, machine learning [24] and deep learning techniques [25, 26] have been gaining a lot of attention [27]. Machine learning approaches have become more feasible in engineering applications as computing power has increased and chip and sensor technology has advanced. Recent research has highlighted that machine learning approaches are more systematic and efficient to traditional ones, particularly when dealing with fuzzy, vague, or noise-contaminated data [28].

ML has been applied to solve multiple problems in structural engineering. Studies showing its applicability for a wide range of structural problems, can be found in [29–34]. As a result, research in this area is of interest, and new approaches can aid more established ones.

1.2 Aims and outline of the thesis

The goal of this thesis has been to develop and validate methodologies for the assessment of large-scale infrastructure, taking into account the characteristics and issues of the typology to which they belong, in order to provide accurate knowledge regarding the current structural state and forecast its evolution. Studies have been carried out to propose appropriate and economically viable methodologies, supported by the use of *AI* algorithm for widely repeated structures. This chapter gives a brief introduction of structural monitoring systems (Section 1.3), emphasizing the different types of data that can be recorded, the damage-sensitive features that follow, and the main approaches associated with them. Then, the focus shifts to the various methodologies utilized to analyze the data (Section 1.4), as well as the limitations and the open challenges that the current state of the art faces and the general methodology proposed in the work. Following that, the thesis is organized as follows: Chapter 2 focuses on methodologies supported by an unsupervised algorithm for the control of an highway steel arch bridge, Chapter 3 shows techniques suitable for pre-stressed concrete railway bridges based on both supervised and unsupervised algorithms, Chapter 4 investigates the use of domain adaptation techniques (transfer learning) for pedestrian bridges assessment, Chapter 5 presents the development of a multilevel methodology for the tunnels control, and Chapter 6 outlines the conclusions of the entire work.

1.3 SHM systems

Hardware and software components make up a typical structural health monitoring system. The sensing and data acquisition interface make up the hardware part. A wide range of instruments can be used to record measurements from which damage-sensitive features can be extracted (e.g., accelerometers, velocimeters, strain gauges, load cells, fiber-optic sensors, acoustic emissions, ground penetrating radar, ultrasonic, magnetic field, radiography etc.). On the other hand, the software component of a structural monitoring system is composed of signal-processing and pattern-recognition algorithms that convert the signals obtained by the sensing network into key information about the structure under monitored.

The following subsections will focus on some of the main instrumentation, damage-sensitive features, and methodologies aimed at non destructive testing (*NDT*) for structural condition assessment purposes. Emphasis will be placed on the different types of data that can be used. For this reason, first, monitoring systems based on dynamic and static measurements 1.3.1 will be discussed in detail. Subsequently, other approaches for a non-destructive evaluation that are succeeding in the field of *SHM* will be examined 1.3.2.

1.3.1 Vibration-based and static-based methods

Vibration-based methods

Sensors that record the dynamic behavior of structures, such as accelerometers, are widely used ones as damage is frequently identified by changes in dynamic behavior. In the literature, there are several studies on vibration-based methods [35–40]. Vibration-based damage detection systems have been developed on frequency-domain features. The latter entails frequencies, mode shapes, damping ratio, modal strain, modal strain energy, modal curvature, and modal flexibility. The modal parameters: natural frequency, damping ratio, and mode shape (in addition to the signal's own parameters such as peak acceleration/displacement) describe the evolution of structural behavior. Damage structural state is linked to changes in modal parameters. For instance, the development of a crack would imply a change in geometry and, as a result, a shift in stiffness, which could be easily caught by frequency variation. Further types of damage that can be detected by the change in modal parameters include scour of a bridge pier and loosening of a bolted connection.

The modal parameters are estimated by means of Operational Modal Analysis (*OMA*) and Experimental Modal Analysis (*EMA*) [41]. One of the most extensively utilized dynamic identification approaches is *OMA*. Such approach is output-only because excitation is not known and assimilated to white noise. It avoids using equipment to excite the structure (for example, vibrodyne and hydraulic actuators). This prevents the interference with the operations of the facility [42] and implies a saving in testing time and cost. The key to strengthening this method and making it effectively successful for *SHM* purposes is to perform dynamic identification procedures in a fully automated way [43]. Structural Health Monitoring dynamic approaches have been studied and developed for decades and are excellent tools. The following are just some examples of data analysis based on ambient vibration recording [44–46]. Particular attention should be required when using this methodology in situ. Damage detection based on frequency response [47, 48], mode shapes [49, 50], and damping ratios [51, 52] has revealed that data volume, monitoring time, uncertainty [53], and environmental effects all have a huge effect on damage detection since they generate data variance [54]. Several novelty detection approaches in the civil engineering field, in fact, are unable to distinguish between frequency variations caused by environmental/operational conditions and the ones caused by structural deterioration. There are methods for filtering data to remove disturbances, but this is a difficult operation that typically necessitates long-term monitoring and, consequently, a large amount of data storage. Besides, such methods have been revealed to be relatively unaffected by local damage in real structures. The drawbacks in addressing the negative consequences produced by these issues continue to stymie progress to real-world applications [50]. In addition, infrastructure managers often find it difficult to store dynamic data from continuous monitoring, and therefore prefer analyses using static data.

Static measurements-based methods

Sensors that record static features of structures, such as displacements [55], deformations [56], and curvatures [57], are frequently used because they make it easier to reach the second level of the hierarchical structure of the damage identification problem, i.e. the damage location. Higher degradation local sensitivity and easier damage localization are two benefits resulting from their utilization [58]. They are also usually simpler and more accurate than dynamic ones [59]. Insights into the use of static measurements in the field of *SHM* can be found in Chapter 3 of this thesis. Section 3.2, in particular, provides an overview of studies in the area of anomaly detection.

1.3.2 Techniques for non-destructive evaluation

It is thought required to focus on at least three of the most valuable non-destructive structural condition evaluation approaches in order to get a thorough overview of them. Digital image correlation methods, acoustic emissions-based techniques, and Ground Penetrating Radar-based approaches are the ones that will be deepened.

Digital image correlation methods

Digital image correlation (*DIC*) is a powerful technique to control the integrity of large scale civil infrastructure. It is a non-contact, full field, and optical measuring technique that utilizes digital cameras to determine surface geometry, displacement, strain [60], and the dynamic of a structure. Recent advancements in camera technology, optical sensors, and image processing algorithms have aided the emergence of this approach [61]. Recently, *DIC* systems have demostrated their effectiveness in providing accurate quantitative information. Some successful approaches have combined this technique with unmanned aerial vehicle to perform non-contact optically based measurements to monitor the health of bridges [62, 63].

Acoustic emission methods

Acoustic Emission (*AE*) is a non-destructive testing technique used to identify defects and damage in heterogeneous elements. Acoustic emissions are, in fact, ultrasonic waves generated by a rapid release of energy caused by discontinuities or propagation of cracks in materials subjected to states of tension or deformation. Such technique involves piezoelectric broadband sensors to detect the waves released by materials with frequencies typically between 50kHz and 1 MHz. It is, thus, employed in several disciplines of engineering that require quality control and structural monitoring; in particular, it is used in civil engineering to monitor crack propagation and estimate the extent of structural damage. It is also feasible to calculate the quantity of energy emitted during crack propagation and obtain information on structure durability. Recent studies have shown the application of this technique for structural integrity assessment [64–67].

Ground Penetrating Radar methods

Ground Penetrating Radar (*GPR*) is one of the most widely used non-destructive structural monitoring techniques for tunnel control [68]. It is a geophysical technique that uses high-frequency electromagnetic wave impulses. It boosts visual inspection techniques that are fit for detecting surface defects [69], providing an effective and fast interpretation of several tunnel lining defects [70]. Nonetheless, since data is typically manually scaled and interpreted or stored and then later analyzed off-line, the process of *GPR* data interpretation is generally computationally expensive [71]. Subsection 5.2.1 will provide more information and insight into this technique.

1.4 State of the art methodologies: model-based and data-based approaches

In this section, emphasis is placed on the type of approach used to process the information collected during the monitoring process. In detail, the focus is on the presence (model-based method) or absence (data-based method) of structural models and on the use of domain adaptation techniques (transfer learning).

1.4.1 Model-based methods

By updating model parameters with input-output measurements, the model-based method tries to develop an accurate finite-element model. Nevertheless, prior knowledge of the true model is needed for the estimated parameters to fall within an appropriate confidence interval; however, the parameters determined by a mathematical procedure may not be unique, resulting in less physical interpretability [16]. Among the optimisation techniques to update the model, one chooses to focus on genetic algorithms. This choice is due to the fact that the genetic algorithm (*GA*)is one of the most optimisation techniques used in the field of *SHM* to update structural models for damage detection. It produces good solutions for the parameters to be estimated from a population of individuals that changes through time [72, 73]. Once created a population of *npop* individuals, each solution is examined by means of a cost function. The best individuals are selected to generate new individuals (offspring) utilizing crossover and mutation operators. Then, merge and sort operations are conducted. The better *npop* individuals will make up the new generation. The process is finished when the set number of iterations is reached or the quality of the better solution is deemed satisfactory. Just the "best appropriate" individuals survive and reproduce, lowering future generations costs. The *GA*'s design needs the specification of several qualitative and quantitative parameters [74]. Operators such as selection, crossover, and mutation are instances of the former. The latter includes population size (*npop*), crossover rate (*CR*), and mutation rate (*MR*). The main organization of the algorithm is determined by the first set of parameters, called high-level parameters. Low-level parameters are the second set of parameters that are utilized to generate a version of the algorithm. The *GA* method has been used to address several damage identification problems. A lot of studies have been focused on comparing computed and measured dynamic structural responses (e.g., natural frequencies and mode shapes) [75–78]. They require a big number of sensors and a large amount of data to be successful. The findings of studies integrating both static and dynamic features [79] show an improvement. It is less frequent to utilize a combination of modal parameters and static displacements [79, 80], or static features solely [81].

1.4.2 Data-based methods

The data-driven approaches build a model in the form of statistical representations, such as the probability density function [82], and so can account for uncertainty in raw data. Data-driven methods do not require any prior knowledge because they immediately analyze data patterns of structural condition changes. In this way, damage detection may be converted into a statistical pattern identification problem [10]. Even though these methods have been extensively used in *SHM* data processing, there are still certain shortcomings in their common applications.

In the context of modern *AI* systems, data-driven methods leverage machine learning and deep learning algorithms. A set of operations, as depicted in the following flowchart (Figure 1.1), are frequently required before and after their application. Following the logical flow shown in the Figure just mentioned, particular attention will be paid to data pre-processing, data integration, feature extraction and selection, and pattern recognition in the remainder of this subsection .

Data preprocessing, which involves data cleaning, transformation, and dimension reduction, is used to ensure that data are suitable for further analysis [83]. Noise removal, trend or outlier removal, and missing value imputation are all part of data cleaning. The technique of reducing the number of variables in attempt to optimise pattern recognition performance is known as dimension reduction. The approaches for reducing dimensions can be linear or nonlinear (e.g., principal component analysis and non linear principal component analysis). After preprocessing operations, data integration methods are often needed. They combine dissimilar data from several sources [83]. Details on this technique can be found in [84, 85]. After data preprocessing and integration, engineering features capable of defining structural behavior must be extracted and selected [86]. Typical features used in different *SHM* issues can be found in Section 1.3. Another aspect that deserves further investigation is data normalization. Some insights can be found in Chapter 2 and Chapter 3. As it is possible to observe in the Figure 1.1, the most widely used machine learning algorithms can be of different type (supervised and unsupervised). In the following, particular attention will be paid to their differences and fields of application.

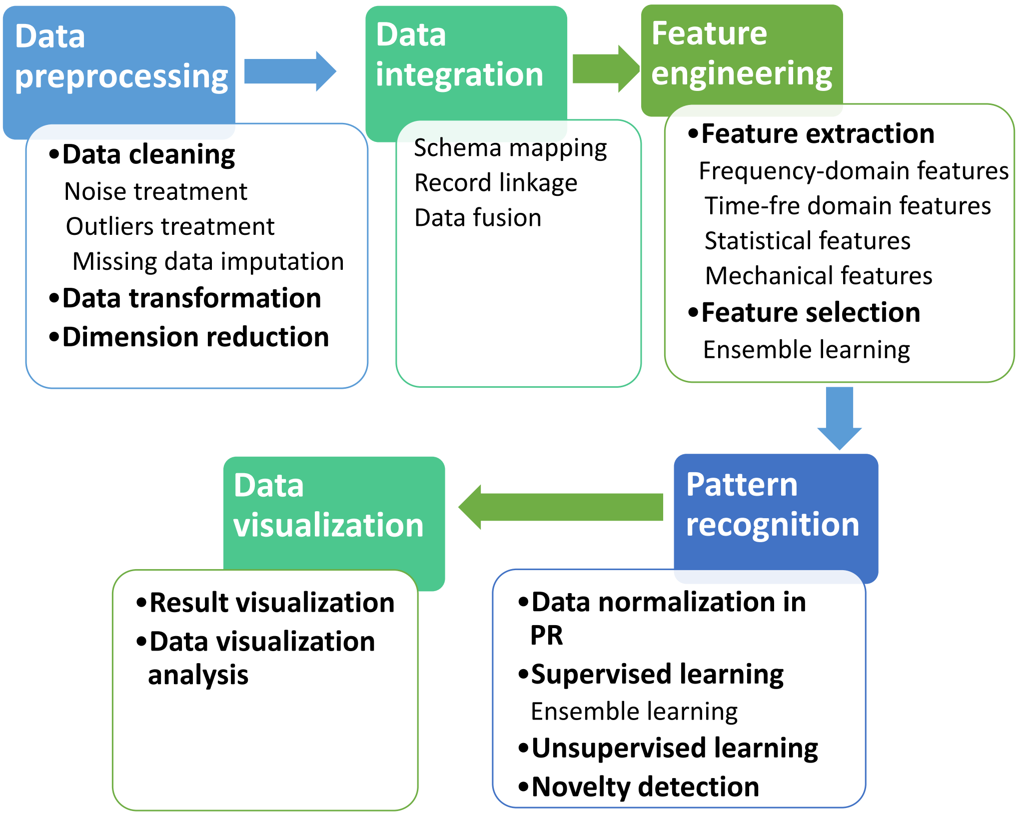

Fig. 1.1 Pipeline for BD analysis

Unsupervised learning algorithm

Unsupervised learning methods rely on not labeled data. They analyze the distribution of data in order to extract relevant information about its structure. Unsupervised learning approaches include clustering and association analysis.

Clustering divides unlabeled data into groups based on their internal structures. The main clustering algorithms are: K-means clustering [87], Hierarchical clustering, DBSCAN [88] , Fuzzy clustering [89], and Self Organizing Mapping.

The approach of discovering meaningful relationships, i.e., association rules, is known as association analysis [90]. Due to the high processing cost, association analysis is often employed with categorical data and is rarely utilized with numerical ones.

Supervised learning

Supervised algorithms need a dataset composed of human-labeled data for training and aim to extract the optimal mapping between input and output (or target) [22]. Classification and regression are part of supervised learning.

Classification algorithms use labeled data from the training set to train a classifier. Then, the model can accurately predict the labels of incoming input data. The following are some of the most widely used classification methods: Artificial Neural Network (*ANN*), Support Vector Machine (*SVM*), Naive Bayes, Bayesian Network, Decision trees, and K-nearest neighbor. Damage identification, load effect analysis, load pattern recognition, and structural retrofitting assessment are often faced by means of classification methods. Besides, also the image recognition issue is often formulated as a classification task in damage detection framework (see Chapter 5) . Convolutional Neural Network (*CNN*) and transfer learning approaches, in particular, have been used to improve performance by using pre-trained deep networks. The direct extraction of data features is one of the key advantages of such *AI* networks. The structure of the network is defined by hundreds of layers, which are akin to the biological structure of the visual cortex. Each layer picks up some characteristics from the images. Convolution, activation, pooling, and fully connected layers are the four types of layers that make up the network architecture [91]. The first contains neurons that are put in a feature map and are connected to adjacent neurons in the next layer through convolution kernels. The second is used to extract nonlinear features. The third minimizes the size of the convolved feature in order to improve algorithm performance and lowers computing costs. The last layer evaluates the previously extracted attributes and generates a vector with the probability of belonging to each class. The transfer learning approach allows for the usage of deep learning without a large dataset and a long training time. It entails retraining existing networks for different categorization scenarios using their dataset. Transfer learning for network fine-tuning is faster than training a network from scratch, and it shows outstanding accuracy even with less training data. Refs [92–97] show some examples of structural damage classification using transfer learning and convolutional networks. It's worth mentioning that the types of categorized defects in most literature research are fairly limited, and the data frequently refer to optimal laboratory conditions. Classification algorithm have some drawbacks in the *SHM* field. The main problem is linked to the presence of few real data matching the damage. For this reason, the abilities of classification algorithms are frequently examined using data not from real facilities. The use of data by numerical or experimental models, which by definition doesn't reflect the actual structural behavior, weakens this methodology.

The regression operation is similar to the classification one. What changes is the type of values predicted. Continuous values are predicted by regression, whereas discrete labels are predicted by classification. Correlation relationships between dependent and independent variables are described by regression techniques. Nonlinear regression, Support Vector Regression (*SVR*), and Autoregressive models (*ARX*) are some of the most commonly utilized regression approaches. In the field of *SHM*, studies linked to the usage of regression models can be found in [98–103].

Despite the availability of numerous algorithms, it is impossible to discover one that is ideal in all aspects; this phenomena is known as the "no free lunch theorem" in supervised learning [104]. An idea to solve the problem is ensemble learning, which combines many base learners to boost performance.The main ensemble methods are: Voting [105], Adaboost [106], Bagging [107], Random Forest [108], and XGBoost [109]. More details about XGBoost are provided in the section 3.2

Methodologies

One of the approaches worth focusing on for the development of *SHM* strategies is novelty detection. The first stage in novelty identification is to create a baseline model to reflect healthy structural condition; the second step is to compare new data to the baseline, with novelties being identified if they exceed specified thresholds. The novelty detection methodology is often used because there are very few scenarios where experimental data are accessible in damaged cases [10, 110]. However, data generated by models (e.g., the F.E.M. model) are not always valid for expressing the effective structural condition due to the great complexity of the systems, the intrinsic inaccuracy of the model, and the problems in development and implementation of damage scenarios. As a result, a created normal condition model is frequently used in damage diagnosis.

The representativeness of the training dataset is linked to the efficacy of the novelty detection algorithm [111]. Due to a lack of representativeness, a distinction between faults and operational conditions is lost, resulting in false alarms when novel operating conditions that were not seen during the training period are classified as defects [112]. To overcome this problem, approaches based on the concept of transferring information between systems with comparable properties but operating under different conditions [113, 111] have been developed. The extraction of significant features is another part of this process that needs great attention. This is particularly important in applications with a high dimensionality, namely when there are several factors monitored and used for damage detection. Promising approaches can be found in [114].

There are three main techniques for implementing this approach. The former uses probabilistic approaches; the second reconstruction-based techniques; the third clustering-based methods. As regard the first, literature references for deepenings can be found in [115–119]. As regard the second, it is worth noting that it use reconstruction errors, generated by algorithms like regression, to pinpoint novelties. The errors are normally assumed to be Gaussian and the confidence level can be used to set a threshold. Literature references for such approach can be found in [120–123]. Section 3.2 contains deepenings and a subsequent application of this approach. As regard the third, it is interesting to note that it is often used incrementally. Reference can be found in [124–128].

1.4.3 Transfer learning

A subfield of machine learning is transfer learning. It proposed a new tool to assess the structural state of bridges on the basis of data from one or a small number of them. This is gaining significance because bridge authorities can accumulate data from a small number of representative bridges, i.e., bridges that are not nominally identical but have structural similarities, to develop machine learning algorithms that can detect damage in bridges without long-term monitoring data. This may alter the way we execute *SHM*, allowing us to shift to population-based *SHM* and save money on both the investment and operation of persistent *SHM* equipment. [129–132] set the groundwork for population-based *SHM* in mechanical systems. Transfer learning is a technique for mapping feature and label distributions from various structures, labeled sources, and unlabeled target structures into a common space. As a consequence, classifiers trained in the source domain on a labeled structure will adapt to a distinct unlabeled target structure. The goal of transfer learning is to aid a learner develop in one domain by transferring information from a correlated domain. Domain adaptation is a type of transfer learning in which the goal is to minimize the distance between different data distributions in the source and target domains. [133] provide a concise history and comprehensive overview of transfer learning and domain adaptation. In the area of *SHM*, many authors have lately implemented transfer learning for damage identification. [129] used many laboratory case studies to illustrate three domain adaptation techniques: Transfer Component Analysis *(TCA)*, Joint Distribution Adaption *(JDA)*, and Adaptation Regularization based Transfer Learning *(ARTL)*. New solutions for handling the challenge of population-based *SHM* have been developed as a result of this effort. Nevertheless, no data from the real world has been utilized. Further in-depth studies focusing on the use of *TCA* can be found in [134, 135]. Further advantage related to the transfer learning would be the ability to use data from a laboratory-based experimental structure or numerical data from a finite element (*FE*) model to label data for any bridge, resulting in significant gains in applying *SHM* to the majority of bridges. *FE* model data has previously been used by several researchers to assess the reliability of domain adaptation [129]. Despite the fact that some laboratory applications [136] have already been shown, there are few publications related to data stemmed from real-world bridge.

1.5 Limits and open challenges

Although the literature in the topic of *SHM* is extensive, there are limitations and several open challenges that researchers in the field must address. These include the lack of criteria for selecting appropriate algorithms in specific tasks, the quantification of data and their typology needed for *BD* strategies in *SHM*, the difficulty in evaluating damage detection algorithms given that most bridges are in good condition, the development of economically sustainable methodologies on large scale.

This thesis merges studies that have aimed to develop *SHM* strategies suitable for specific structural typologies and by means of numerical simulations, but above all real case studies, has attempted to investigate and propose solutions to overcome certain issues. For example, the impact of data volume and monitoring time on the estimation of damage-sensitive features and their uncertainty has been investigated. On the other hand, the lack of some parameters has been underline as a factors decreasing the algorithm performance and solutions have been proposed and tested. Furthermore, approaches have been presented to reduce the calculation time and the need to record many parameters in order to fulfil the requirements of an economic and sustainable control system. Finally, methods to avoid the long-term monitoring of all the structures to be controlled, tested by means of damage simulations on real structure, have been investigated underlying their potential and limitations. Clearly, there are many challenges yet, but the results are promising.

1.6 Principles of the proposed methodology

The general methodology that such thesis proposed is composed by six main steps, summarized as follows:

- choice of main infrastructural typologies;
- for each selected typology, structural studies are carried out to highlight the critical structural elements and potential failure modes;
- definition of control parameters;
- definition of the monitoring architecture and sensors typology in an cost optimization and network robustness view;
- choice of the machine learning algorithm to automate the assessment process;
- validation on the procedure.

First of all, as previously mentioned, the most common construction materials and static schemes were considered as key factors to choice the main infrastructural typologies to be controlled. The similarity of the structural response derived from belonging to the same typology is the starting point for the extensive application of the proposed strategies.

Second, structural studies and consideration turned out to be pivotal for the choice of the sensors to be used and their position along the structure. For each case study the nature of parameters to be controlled was chosen on the basis of the evidence revealed by studies in the literature. Such choice was strictly linked to the economic sustainability and robustness of the system to be implemented.

A machine learning algorithm selection was then made in order to automate the process of structural condition evaluation using the chosen parameters/features. Due to the large number of variables that influence a choice's quality, this was a challenging undertaking. Data and problem type, computational time, and complexity are a few of them.

Finally, the developed strategies were validated with numerical and/or real scenario.

Chapter 2

Customised active monitoring system for a steel arch highway bridge control [1]

2.1 Problem definition

Steel arch suspended highway bridges belong to a structural typology that has been developed for a long time and presents some peculiarities. Notably, suspenders are one of the most vulnerable bridge components [137] under repeated traffic loads. [138]. Issues related to the combined effect of corrosion, axial forces, and unexpected bending stresses can lead to damage, especially in the lower ends of short bridge suspenders. Rainwater ingress is the primary cause [139], but there are also large secondary stresses [140] caused by relative movements between the cable and the girder. Hangers are particularly prone to fatigue phenomena. However, despite being a key parameter in the hanger's fatigue behavior, the fluctuation of axial forces in

---

[1] Part of the work described has been previously published in:
B. Chiaia, G. Marasco, G. Ventura, C.Z. Quirini. Customised active monitoring system for structural control and maintenance optimisation. Journal of Civil Structural Health Monitoring 10(2), 267-282 (2020).
B. Chiaia, G. Ventura, C.Z. Quirini, G. Marasco. Bridge active monitoring for maintenance and structural safety. In: Arêde, A., Costa, C. (eds) Proceedings of ARCH 2019. ARCH 2019. Structural Integrity, vol 11. Springer, Cham, 866–873 (2020).
G. Marasco, B.Chiaia, G.Ventura. AI based bridge health assessment. In: 9th International Workshop on Reliable Engineering Computing (REC 2021) is "Risk and Uncertainty in Engineering Computations. (2021)

them has received little attention [141]. Corrosion fatigue can occur as a result of these symptoms, resulting in faster wire deterioration, premature suspender fracture [142, 143], and bridge collapse [144, 145]. Criticality related to structural typology and material issues are accentuated in part by the service class to which they belong. Talking about highway bridges, in fact, there are many unknowns related to vehicular loads as it is not known exactly in a given time instant which is the distribution of such loads on the carriageway and their entity. As a result of all of the issues highlighted so far, a monitoring system has been designed whose architecture is composed of several types of sensors that are arranged so that the static and dynamic structural responses may be controlled in real time and automatically.

2.1.1 Description of the structure

The structure under examination is a highway suspended arch steel bridge with a span of 250 m. Its structural layout is a single arch connected to the inferior way by vertical steel cables. A chain beam and transverse cantilevers with an 8-meter spacing along the bridge axis constitute the bridge deck. The deck has two carriageways with a total width of 17.55 meters per way, including the docks. Depending on where they are along the arch, the steel cables are made up of 33, 37, or 43 strands. The chain beam is placed at a higher level than the road surface one to shield it from possible impacts with vehicles.

Fig. 2.1 General view of the viaduct

Fig. 2.2 Transversal view during construction

Figure 2.1 and 2.2 show some illustrations of the structure.

2.2 Monitoring and control system

This section describes the monitoring and control system devised by Prof. G. Ventura, which served as the foundation for the technique that has been developed afterward.

2.2.1 Active monitoring

The proposed application is the first implementation of the novel paradigm of *Active Monitoring* ideated by G. Ventura for ARCOS Engineering. Active Monitoring entails interpreting obtained data in real time, using a computational model of the structure, performing a real-time structural assessment, and detecting potential crisis mechanisms. It has been created with a clear objective. Capacity of executing a continuous automated structural health check for the structure going beyond the limits of traditional monitoring. Besides, it is a tool for the right suspension cable tensioning during construction. Indeed, being there is a strong closed loop connection between the cables and the structure, this is a nontrivial process for the specified bridge type. The methodology exploits a computational model to assess continually the correlation between the recorded physical data. A structural response that differs from what is expected could be an indicator of damaged structure. The methodology also considers environmental factors, thus mitigating the effect that variation in these factors could have in indicating possible damage. Consider a balance scale and the displacement at the weighing dishes (Figure 2.3), as well as the rotation of the beam, to show the general principle of Active Monitoring. We assume the two displacements at the weighing dishes to be equal and opposite during regular use of the balance, and that the rotation of the balance beam is linked to the displacement at the dishes via a trigonometric law. Such correlation between the acquired data is always present and, in Active Monitoring, it is assessed all the time.

Fig. 2.3 Book of Dead of Ani

Sensors are installed in a structural system, such as a bridge, to estimate loads and other physical features such as displacement, rotation, thermal deformation, and acceleration. After adequate elaboration, the sensor data is used as input to the finite element model of the structure, whose output is compared to sensor data, as shown in (Figure 2.4).

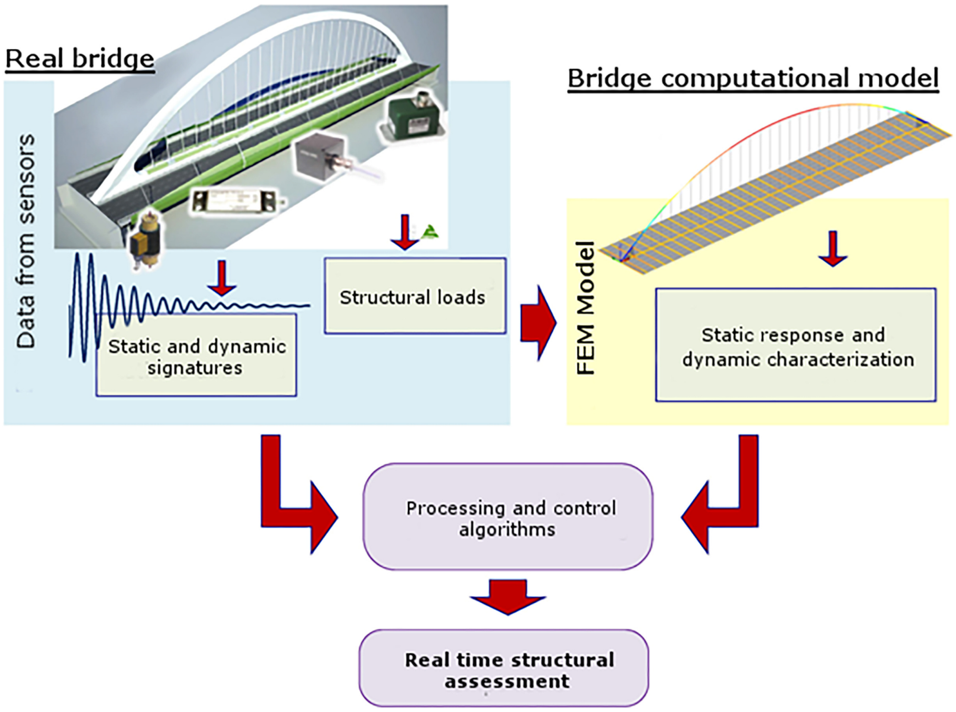

Fig. 2.4 Active Monitoring process

This gives the possibility of to determine whether the structure is behaving as expected and so validate its health condition. As a result, the strategy derived from the Active Monitoring paradigm differs significantly from traditional monitoring, in which absolute thresholds are checked and, in most cases, data is off-line elaborated by expert teams, resulting in increased cost and processing time. Obviously, an automated system like Active Monitoring cannot substitute an expert's analytical capacity in structural data analysis, but it can be a priceless tool for the activation of first-warning procedures (e.g., specialized counseling).

2.2.2 Monitoring architecture

As Figure 2.4 shows, the data recorded by the sensors are both static and dynamic. There are twelve measuring points in the monitoring architecture, the locations of which are illustrated in Figure 2.5.

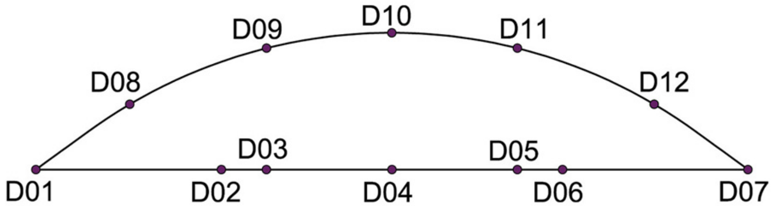

Fig. 2.5 Position of instrument groups in the structure

With reference to Figure 2.5, the following is the list of sensors and their locations:

- D01 and D07, high resolution servoinclinometrs;
- D04, D08, D10, D12, air temperature and humidity sensor;
- D03, D05, D09, D11, triaxial accelerometers;
- D08, D12, differential wind pressure transducer (probes are installed in between D08/D09 and D11/D12);
- D04 strain gages at runway cantilevers;
- Each suspension cable is instrumented with a load cell.

In addition to these, there are steel surface temperature sensors. In detail, there are 4 sensors per measuring point located at the four sides of the cross section (top, down, left, right). In Figure 2.6, these sensors are labeled with "TR". Each of these is fitted into a RACK's area.

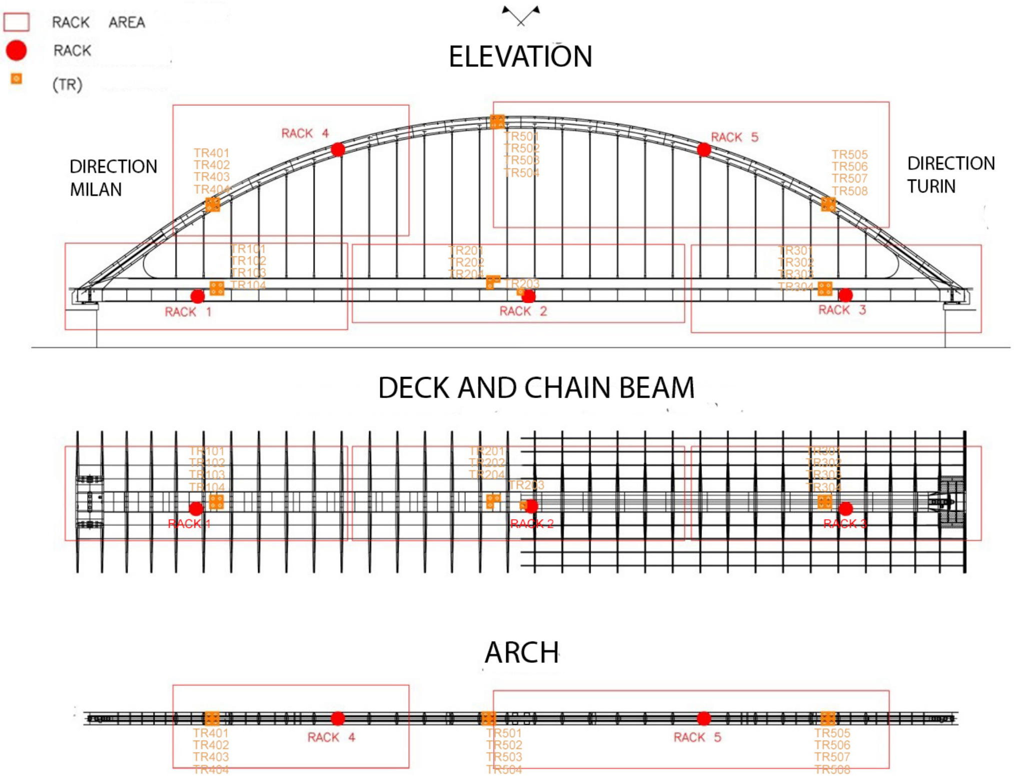

Fig. 2.6 Position of the surface temperature sensors in the bridge

A mounting steel plate has been used to provide a common mounting platform for the sensors and to ensure a standard installation methodology in all positions. Sensors have distributed differently on the plate based on the data acquisition point of the structure. The sensor placement just described is the result of knowledge of the structural typology to which the bridge belongs.

2.2.3 Data Acquisition

The data acquisition infrastructure is composed of five measurement stations connected by a fiber optic data network that reaches the monitoring control room, located at the east bridge end. The placements of the five measuring stations have been chosen to keep sensor connection cables length to a minimum. The hardware architecture for the measuring stations is composed of Industrial Programmable Application Controllers and high precision A/D modules, which have been selected for optimal durability and future spare part availability. The sensor values are sent to the data processing computer at a frequency of 5 Hz, which is suitable with the structure first frequencies of oscillation, which are much below 1 Hz.

2.2.4 Data Processing

For data acquisition and Active Monitoring processing, ARCOS Engineering has created a bespoke software. The software collects data, assess for proper communication with the data acquisition system, calls the finite element computational engine and processes the outcomes. It compares sensor and model data to check structural health and sends alarm messages and information about the system's effective functioning. The simplified model is composed by 228 nodes and 130 beam elements, with bar elements modeling the cables. Data processing follows acquisition with a small delay to minimize excessive wear on the processing computer hard disks. A total of 1,000 time steps are bundled together and sent to the finite element computational engine as loading conditions to be examined in a single run. This makes the computation highly fast and removes the need for intensive I/O disk operations. LUSAS Version 15 by FEA Ltd (http://www.lusas.com/) is the software for the finite element model. The program is driven by text data files, that the software generates, and returns a text results file that is analyzed to gather the analysis' findings. LUSAS has been selected for its dependability, speed of execution, and capacity to assign several load typologies (e.g., forces, thermal, acceleration, displacement, and rotation) in a quick manner. The simplified 3D model of the structure takes into account the loads in the list below:

- tension variation at suspension cables;
- temperature and temperature gradients in the entire structure (measured at steel surfaces and interpolated in between the measuring points);
- bending and torsional rotations;
- wind pressure;
- inertial forces. These are recorded at the four accelerometers in the structure and are extrapolated to the entire structure using the theory of influence lines.

The abovementioned loads are considered as variations in relation to an initial condition, because the sensor readings begin when the structure is already built.

Once the finite element model has produced its results, the measured quantities at the sensors are compared to the model's corresponding values, and if there is a mismatch, a warning is provided. The tension in a suspension cable, for example, is measured. The model is after loaded with the above list of loads, and the normal force at the cable is calculated. In principle, the measured and computed forces should be the same. The system generates graphs of measured vs computed quantities, and a synoptic view with semaphores is provided for a quick graphical representation of the findings of the comparisons (see Figure 2.7).

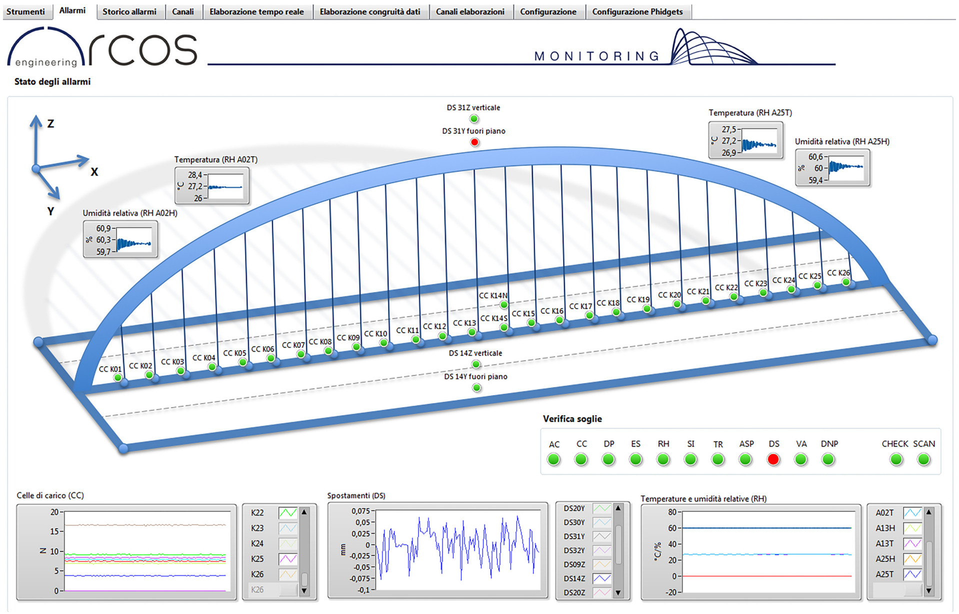

Fig. 2.7 Structural Health semaphores in the Active Monitoring System

2.2.5 Instrumentation

In this subsection an in-depth examination of the monitoring instrumentation is carried out. In detail, the main characteristics of strain gauges, inclinometers and accelerometers are outlined.

As straing gauge, the Magtrol KG-05 Extensometer has been used. It is designed to measure deformations of built or constructed objects while they are loaded. It can be utilized as either a load cell or a force transducer since the output signal is proportional to the applied load. When large transducers are ineffective for measuring strain, the KG-05 Extensometer is the best option. Its compact size and flat mounting make controlling deformations on steel structures simple. Table 2.1 shows its mechanical, electrical and environmental characteristics.

Table 2.1 Technical ratings

Mechanical characteristics	
Maximal Usable Load	1.5 × nominal load
Electrical characteristics	
Nominal Traction and Compression Deformation (ε)	$\pm 600.10^{-6}$
Nominal Sensitivity (at $\varepsilon = 600.10^{-6}$)	
	$\pm 600.10^{-6}$
Input Impedance	990 $\Omega to 1200\Omega$
Output Impedance	1000 ±10 Ω
Environmental characteristics	
Temperature Compensation	Steel: $\alpha = 11.10^{-6}$
Compensated Temperature	-10 °C to +40 °C
Operating Temperature	-30 °C to +70 °C
Protection Class	IP 66

As inclinometer, the Jewell Emerald series inclinometer has been chosen. It is a low cost, high precision inclinometer designed with higher accuracy than comparable MEMS devices. Table 2.2 highligths the electrical and the environmental characteristics. Table 2.3 lists further technical ratings.

Table 2.2 Inclinometer technical ratings

Electrical characteristics	
Number of Axes	1
Input Voltage Range, (VDC)	+15 to +30
Input Current, mA, max	40
Output Impedance, Ohms, nom	10
Noise, Vrms, maximum	0.002
Environmental characteristics	
Operating Temp Range	-55°C to +85°C
Storage Temp Range	-60°C to +90°C
Shock	500g, 1 msec, ½ sine

Table 2.3 Inclinometer technical ratings

Static/Dynamic					
Input Range, °					
±3	±14.5	±30	±45	±60	±90
Full Range Output (FRO -Note 1) VDC ±0.5%					
0-5	0-5	0-5	0-5	0-5	0-5
Nonlinearity (Note 2) % FRO maximum					
0.05	0.02	0.02	0.02	0.4	0.05
Scale Factor, Volts/g, nominal					
47.8	10.0	5.0	3.5	2.9	2.5
Scale Factor Temp. Sensitivity (SFTS), PPM /°C maximum					
100	100	100	100	100	100
Bandwidth (-3 dB), Hz nominal					
5.0	5.0	5.0	5.0	5.0	5.0
Output Axis Misalignment, ° maximum					
0.25	0.50	0.50	0.50	0.50	0.50
Pendulous Axis Misalignment, ° maximum					
0.25	0.50	0.50	0.50	0.50	0.50
0° Output Temp. Sensitivity, Volts /°C maximum					
0.0036	0.0010	0.0007	0.0005	0.0005	0.0005
Resolution and Threshold, radians maximum					
1	1	1	1	1	1

As accelerometers, the Model 4332 produced by the company Measurement specialties ^{TM} have been selected. It is a MEMS Triaxial accelerometer, with low noise, offering both static and dynamic response packaged in a rugged aluminum housing with an integral cable assembly. The Model 4332 is offered in ranges from ±2 ±5g and features gas damped MEMS sensing elements. The accelerometer has a set low-pass filter at 50Hz and an operating temperature range of -40°C to +85°C. The accelerometer is also certified to IP68 protection at 10m depth. The accelerometer is designed to be operated from 5-30Vdc excitation and provides a 0.5 to 4.5V full scale output. The output is DC-coupled and should be used in single-ended mode. A 2.5Vdc bias will be present on the output leads and the output of the accelerometer will be 0.5-4.5V full scale. The model 4332 accelerometer incorporates a LP filtered output for a high output signal. The noise specifications for this accelerometer are detailed in the Table 2.4.

Table 2.4 Noise specifications

Full scale rating (g-pk)	**Sensitivity (mV/g)**	± **5% ampl pass-band (Hz)**	passband noise ($\mu Vrms$)	spectral noise ($\mu g - rms/VHz$)	dinamic range (dB)
2	1000	50	80	8	88
5	400	50	50	13	92

2.3 Methodology and Validation

The Active Monitoring system described so far has made use of an in-depth study of the structural dynamic behavior in order to validate, during its tuning stage, the computational model used by its data processing software.

In addition to such validation, this study has allowed the definition of a scattering range of modal parameters identifying an undamaged structural state in the long term under the effect of environmental factors. On the other hand, critical issues related to the influence of the length of the accelerometric acquisitions and to the specific procedures followed in order to obtain a sufficiently accurate estimate of the dynamic characteristics have been emerged.

2.3.1 Dynamic monitoring

With the goal of obtaining the dynamic behavior of the bridge, an experimental output-only technique has been adopted. The possibility to continually monitor an infrastructure for long time, beginning with its construction and continuing during its life, has provided for the collection of relevant data on the change of its characteristics over time [146]. It has utilized environmental excitement, as is common in large civil structures [147]. Indeed, the other possible approach to this end, namely artificial excitation, is widely acknowledged as being more expensive and having a negative influence on facility service. Figure 2.8 shows the number of sensors, degrees of freedom, and position. Figure 2.9 illustrates some recordings on the bridge deck and arch.

Fig. 2.8 Numbered accelerometers and nodes application

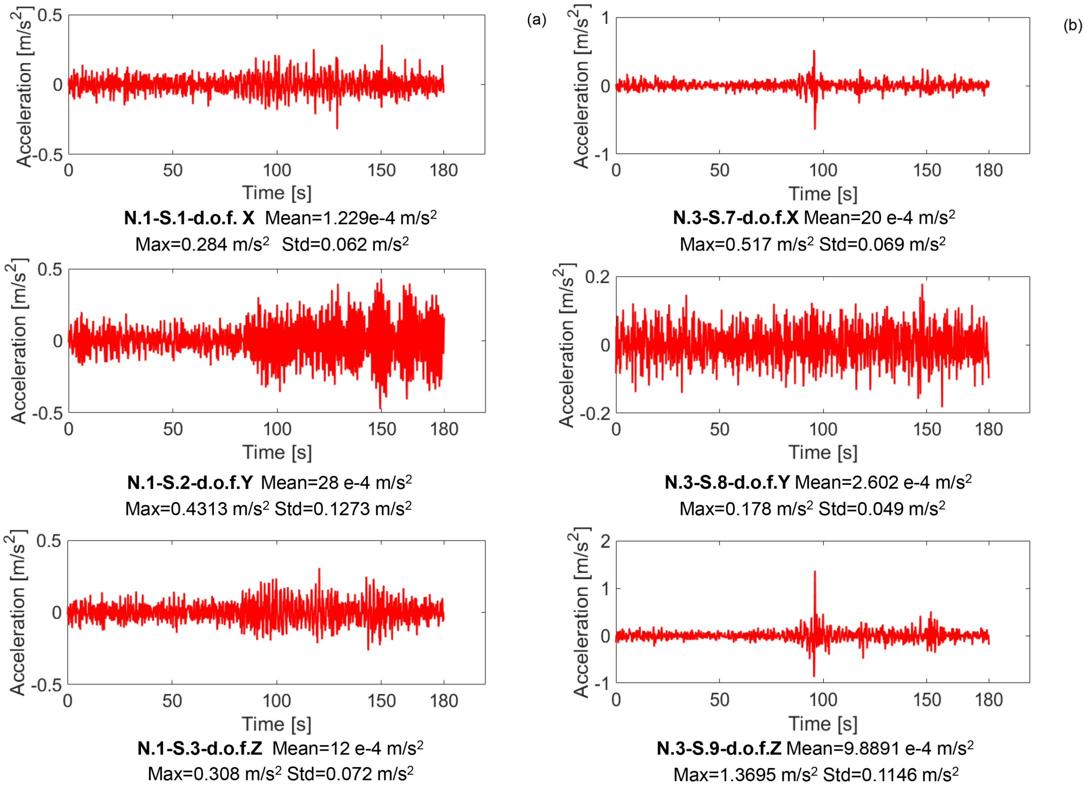

N.1-S.1-d.o.f. X Mean=1.229e-4 m/s²
Max=0.284 m/s² Std=0.062 m/s²

N.3-S.7-d.o.f.X Mean=20 e-4 m/s²
Max=0.517 m/s² Std=0.069 m/s²

N.1-S.2-d.o.f.Y Mean=28 e-4 m/s²
Max=0.4313 m/s² Std=0.1273 m/s²

N.3-S.8-d.o.f.Y Mean=2.602 e-4 m/s²
Max=0.178 m/s² Std=0.049 m/s²

N.1-S.3-d.o.f.Z Mean=12 e-4 m/s²
Max=0.308 m/s² Std=0.072 m/s²

N.3-S.9-d.o.f.Z Mean=9.8891 e-4 m/s²
Max=1.3695 m/s² Std=0.1146 m/s²

Fig. 2.9 Bridge measurements. a) Sensors on the arch b) Sensors on the beam

The software ARTeMIS [148] Modal has been used to accomplish the signal processing. ARTeMIS is a software that can perform a variety of analyses. Among them there is the Operational Modal Analysis (*OMA*). It has been also picked because of its processing speed and the ability to produce outcomes with a high degree of automation. In addition, to decrease the time of analysis, each measurement session's raw data can be processed with the same set of features from a previous session dubbed "Master Session." Furthermore, based on the structure of the measurements, several pre-treatment functions can be used before processing the data. The "detrend function" (to remove mean values and linear trends in the raw data), the "decimation function" (to narrow the frequency range to that of interest), the "projection channel function" (to minimize redundant information), and the "filter functions" (to chose the frequency range of interest) are the most outstanding. In Figure 2.10, an illustration of processed signals and decomposition in singular values of spectral densities is shown. Moreover, ARTeMIS computes the modal parameters uncertainty.

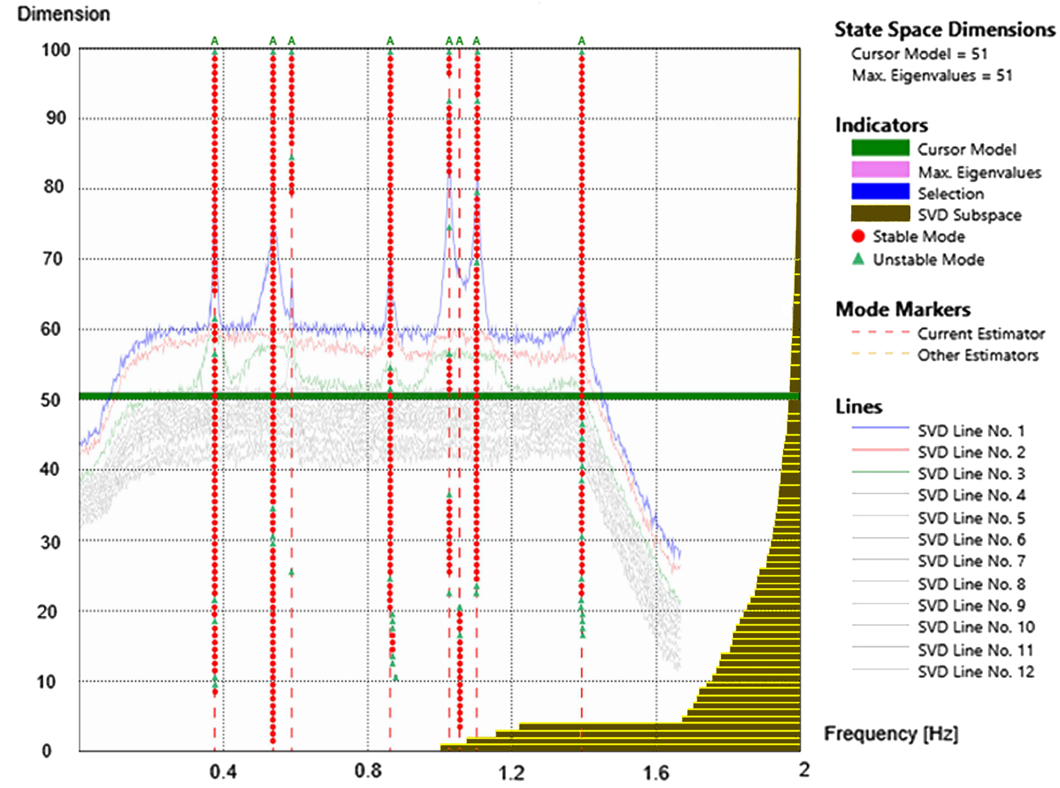

Fig. 2.10 Stabilization diagram

2.3.2 Theoretical and practical issues of data analysis

To emphasize the serial nature of the available records, the analyzed data sets will be defined by means the expression "measurement session" or simply "sessions." The algorithm *DD-SSI-UPCX* (Data Driven-Stochastic Subspace Identification-Extended Unweighted Principal Component) [149] [150] [151] has been chosen to analyze the recorded data sets. It utilizes a parametric model to fit the raw time series data. Such technique in ARTeMIS has also the gain of estimating the modal parameter uncertainties. Furthermore, the motivation for this choice is due to the method's dependability and robustness. It is incredibly useful for flexible structures with low natural frequencies and damping ratios, as well as modes that are closely spaced [152]. Recent researches have been carried out in this context to enhance the quality of outcomes in these scenarios [153]. An additional advantage is its use even with small data sets. However, it should be remembered that, in order to produce an error-free estimate, infinite measurements are required. Indeed, the assumptions that *SSI* models are founded on are as follows:

- Infinite amount of data;
- Linear system;
- White noise excitation.

The number of row blocks in the output Hankel matrix, essentially the sum of row blocks in the past and future output partitions, is a further factor to be taken into account. Each row block includes a portion of the total number of samples of the data set (e.g., j samples). When compared to the previous row block, the j samples inside each row block are shifted by one time-step, equal to the sampling time. To obtain lower frequencies, the number of row blocks must be increased, although this results in a significant increase in computing time/effort and memory usage [152] [154] [155]. However, if this number is excessively high, it will have a negative impact on accuracy due to the creation of spurious numerical modes. Furthermore, the maximum model order is tied to the number of row blocks. The model order can ideally be determined by singular value decomposition of the projection matrix. When dealing with noisy data, nearly all values become non-zero singular values, and the model order increases significantly [152]. As a result, there will be a large number of eigenvalues and most of them are related to spurious modes. Thereby , if the model order is excessively high, the quality of the estimate may decrease. The main principle of the *SSI* approach should be changed in order to increase the accuracy of modal parameter estimate. The projection of the row space of future outputs into the row space of past reference outputs, rather than the row space of past outputs, is an instance of reference-based stochastic subspace identification [147]. Past reference outputs should be identified as belonging to the "best sensors," i.e., those that can track motion better. Candidates for such role should be sensors installed in the best placements, which are those with the highest modal accelerations expected. Indeed, data from sensors near fixed boundaries or at the zeroes of modal shapes degrades the identification outcomes. The computational cost is reduced by selecting specific sensors as references and projecting the row space of future outputs onto past reference outputs. A potential disadvantage of this strategy is that if all modes are not present in the outputs of the chosen reference channels, the identification quality may decrease. The pre-treatment function "project channel" in ARTeMIS enables the implementation of this procedure and, as a result, the comparison of results produced with and without it. The estimated modes are validated in the software by means of a tool that acts in the frequency domain. The stabilization diagram is used to detect structural modes (Figure 2.10). It shows the natural frequency (from zero to the Nyquist frequency) on the horizontal axis and the dimensions of calculated state models on the vertical one. The stabilisation diagram is a useful method for highlighting bias errors, such as model bias due to physical reasons and over-estimation of the system order, and mode bias due to under-estimation of the system order [156] [53]. Singular values are shown by yellow horizontal lines in Figure 2.10. Their number represents how many eigenvalues there are in the data. For each model order, stable modes are chosen based on the following criteria:

- Maximum deviation, for natural frequency (Max Dev f) and damping ratio (Max Dev D), between a mode belonging to a model with an order n and the mode belonging to an order model $(n-1)$;
- Maximum deviation of modal assurance criterion (MAC) of mode shape vector between a mode belonging to a model with an order n and the mode belonging to an order model $(n-1)$;
- coefficient of variation (CV) for each natural frequency (CV f) and damping ratio (CV D), i.e. the ratio of the standard deviation to the mean value.

Such criteria' thresholds are user-defined and based on the problem at hand. There is an extensive literature that outlines the most commonly utilized thresholds for those criteria [157]. Table 2.5 lists the stabilization criteria that have been applied to the problem at stake.

Table 2.5 Stabilization criteria

Data set	**Max Dev f**	**CV f**	**Max Dev D**	**CV D**	**MAC**
	[Hz]	[-]	[%]	[-]	[-]
Small	0.00375	0.02	10	5	0.05
Large	0.0002	0.02	0.04	0.2	0.05

A common value has been utilized for the MAC maximum deviation, both for small and large data sets. The reasons for selecting the other limit values, which vary depending on the length of the dataset under consideration, are explained afterwards. Besides these criteria, the so-called "noise modes" should be avoided. Many factors can produce noise, including an insufficient number of measurements, low calculation accuracy, poor sensor accuracy, and erroneous modeling. The modes with damping ratios higher than 5% (not physical) and less than 0.1 percent (external periodic excitation) are excluded for this reason. All stable modes should be used to estimate final modal parameters. The actual structural modes are represented by the stable modes inside the obtained 'alignments,'. In this framework the term 'alignment,' refers to the vertical stripes in which the estimated modes that represent the same physical modes are clustered. The stable modes contribute by means of their average value, with a weight that is inversely proportional to their coefficient of variation, to compute the final estimate and the parameter's uncertainty. Lastly, the findings obtained using the *DD-SSI-UPCX*approach have been compared to those achieved using the *EFDD* method (enhanced frequency-domain decomposition). Thus, a comparison study has been conducted between a time-domain methodology and a frequency-domain one [158].

As well known, the expected accuracy of the estimate differs for each of the three modal parameters of the structure. The damping ratio errors are consistently bigger than the natural frequency and mode shape ones. Large error bounds in damping ratio estimate are due to his nonlinear behavior, estimator limitations, and the scarcity of measurements [152]. The number of data points in the records and the number of block rows are the two most important factors that determines the accuracy of the modal parameter in stochastic subspace identification. The second aspect has been explored in other research [152] using sensitivity analysis. The first factor will be exploited in the present study to reduce the modal parameter uncertainty.

2.3.3 Natural frequency and damping ratio: range of scattering

To determine a scattering range of modal parameters representing the undamaged structural condition, data acquired unevenly over a period of around one and a half years have been used and processed with the *SSI* method. The sampling frequency utilized in the measurements is 6.66 Hz.

The "Modal Parameter History Module" in ARTeMIS allows users to view the structure's modal parameters over time as a function of measurement sessions in a historical view. As "Reference Sessions," two measurement sessions, i.e. two data sets, are chosen. The software can calculate the mean values of modal parameters for the stable modes in these sessions (Reference Modes). The "Reference Sessions" stable modes comply with the following tolerances:

- The natural frequency should not differ by more than 10% from the prior session;
- In terms of MAC (minimum modal assurance criteria 0.8), the maximum deviation between mode shape extracted by a measurement session and that determined from the preceding may be less than 0.2.

Links/tracks in the graphical presentation of identification findings are drawn based on the reference modes. These links enable a real-time visualisation of the modes' evolution as sessions change. It is also feasible to reach fast assessments. An absence of connectivity between adjacent sessions, for example, is an indication of a change in modal parameters.

Narrow viewing windows

The data acquisition system reads and saves accelerometric data in 180-second sets. Only the "function- detrend" filter has been used to preprocess these single data sets. The outcomes of the calculated first natural frequencies for the available data sets are shown in Figure 2.10. These provide a qualitative representation of the value dispersion. It highlights a maximum value of 0.382 Hz and a lowest value of 0.365 Hz. Natural frequency has a relatively narrow range of variation. For the first-mode damping ratio, the same technique has been used. Figure 2.11 depicts the predicted damping ratios' flow over time. It has a maximum value of 4.57 % and a lowest value of approximately 0.25 %. Figure 2.15 shows the outcomes in terms of natural frequency and damping ratio in a blue histogram. The normal distribution has been used to fit the first natural frequency, whereas the log-normal distribution has been used to fit the first-mode damping ratio. Green curves, in the same illustration, are associated to large viewing windows and are will be explored afterwards. Tables 2.6 and 2.7 show the values of the position and dispersion indices for the two distributions, respectively.

Table 2.6 Indices of first natural frequency distribution (small data set)

Position indexes		**Dispersion indexes**	
Mean [Hz]	**Median [Hz]**	**Range [Hz]**	**Variance [Hz]**
0.3742	0.3742	0.0173	4.66 E-06

Table 2.7 Indices of first damping ratio distribution (small data set)

Position indexes			**Dispersion indexes**	
Mean [%]	**Median [%]**	**Mode [%]**	**Range [%]**	**Variance [%]**
1.61	1.38	1.01	4.32	0.93

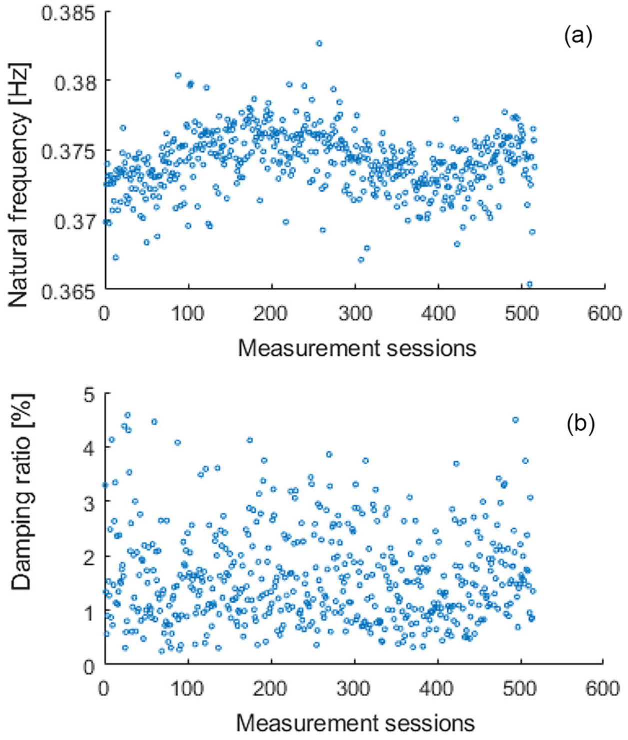

Fig. 2.11 Estimated modal parameters (narrow viewing windows)

Albeit with measuring sessions with a few recordings, the subspace stochastic technique demonstrates a moderate, but not very high capacity, in discovering stable frequencies. Obtaining accurate damping ratio estimates, on the other hand, is significantly more complicated due to a large inaccuracy (the coefficient of variation for the first mode is on the order of 10^{-1}). In the stabilization diagram, the estimated modes have the highest variation coefficient for damping ratio. As a result, exceptionally high CV and maximum deviation of damping ratio criteria (see Table 2.5) have been set. The construction of clusters based on damping ratio appears to be meaningless due to the inaccuracy of its estimation. On the other hand, due to the fairly good quality of the frequency values along the model order, a CV of 0.02 and a maximum deviation of 0.00375 Hz (about 1% of the expected first frequency) has been used. As a result, when compared to natural frequency, the estimation of the damping ratio is significantly less accurate. The frequency–damping diagram (Figure 2.12), which plots the mean value of the first-mode damping ratio against the mean value of the first natural frequency with a confidence ellipsoid, demonstrates this. In contrast to the damping ratio, natural frequency estimate has a very low level of uncertainty. Moreover, because the ellipsoid seems to be vertical, there is no correlation between the damping ratio and frequency.

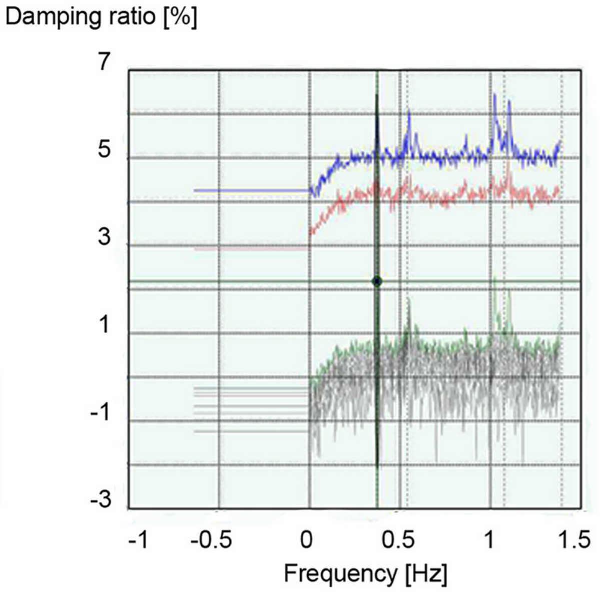

Fig. 2.12 Frequency-damping ratio diagram (first mode)

Although the better natural frequency behavior, the *SSI-UPCX* technique only estimates the first-mode modal parameters for a portion of the sessions for these single data sets (about 76%). Finally, the damping estimation is completely wrong, with an unrealistic scattering range, and the first frequencies do not meet the established criterion in around 24% of the measurement sessions.

Large viewing windows

Data sets are merged in this case to provide larger observation windows. After, it's looked at how much the accuracy of the modal parameter estimation increases. Monthly observation windows have been established for this purpose, and data collected from May to December have been exploited to assess monthly variations. Measurements from the same month have been concatenated, and the estimations for modal parameters (natural frequency, damping ratio, and mode shape) have been examined. Figure 2.13 depicts the extracted first natural frequencies and damping ratios.

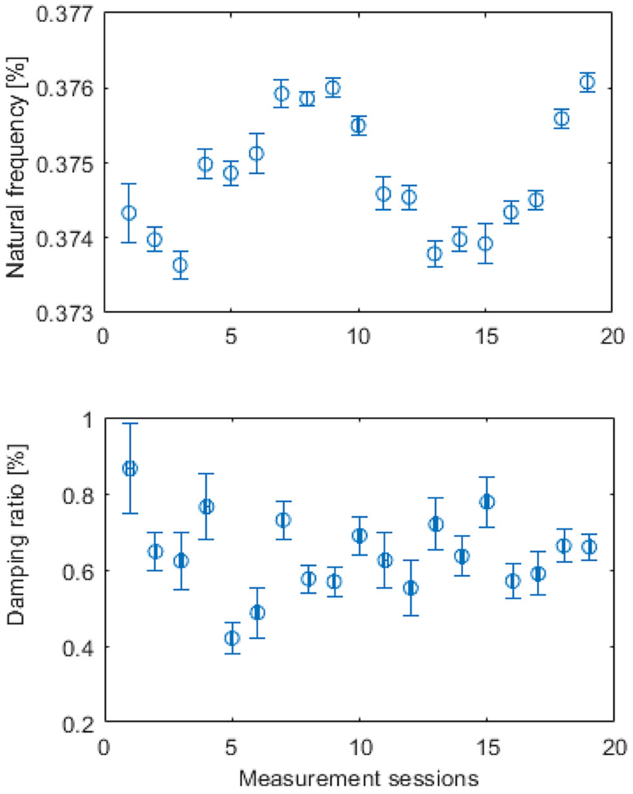

Fig. 2.13 Estimated modal parameters (large viewing windows)

It has been feasible to define an appropriate maximum coefficient of variation for damping ratios using these data sets. The use of damping ratio as a stabilization criterion is justified in this scenario due to the quality of the estimations along the model order. As a result, a modest maximum deviation of damping ratio threshold equal to around 0.04 % of the expected value for the first mode has been adopted (see Table 2.5). The limit values for frequencies, on the other hand, are made more restricted due to the improved quality of the data. In terms of coefficient of variation, the uncertainty drops significantly for both parameters. The maximum coefficients of variation of the final estimations for the first mode are about $10^{˘4}$ for natural frequency and about 10% for the damping ratio. The frequency–damping ratio diagram (Figure 2.14) for the first mode of a session is displayed to highlight how the confidence interval shrinks as compared to the previous case (Figure 2.12).

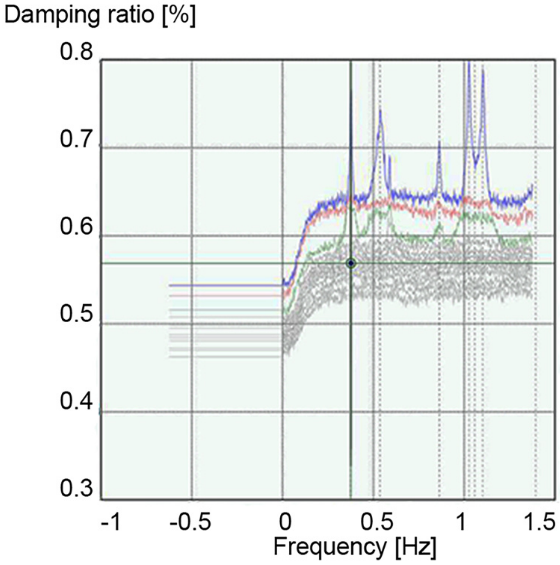

Fig. 2.14 Frequency-damping of a session (February 2018) for the first mode

This improvement enables a considerably more precise estimation and, as a result, a more realistic assessment of the damping ratio. This demonstrates that a minimum number of data points are required to achieve a reliable estimate. As in previous applications [159, 160], the use of small data sets results in substantial modal parameter errors. Other research [160] have defined a minimum threshold of points per data set equal to 4000 points to obtain accurate identification of both modal parameters when the structural frequencies are less than 1 Hz and damping ratio are less than 1%. This is supported by the findings thus far. Data sets with a small number of recordings (under 4000) show a response that is better than damping in terms of frequencies but still unsatisfactory. Indeed, the measurement sessions from which an estimate may be extrapolated represent for just a portion of the overall number of measurement sessions. The damping ratio values, on the other hand, are highly uncertain. Figure 2.15 shows the probability density function of modal

Table 2.8 Indices of first natural frequency distribution (large data set)

Position indexes		**Dispersion indexes**	
Mean [Hz]	**Median [Hz]**	**Range [Hz]**	**Variance [Hz]**
0.3748	0.3748	0.0024	6.58 E-07

parameters estimated for the first mode from narrow and large viewing windows, respectively, in blue and green.

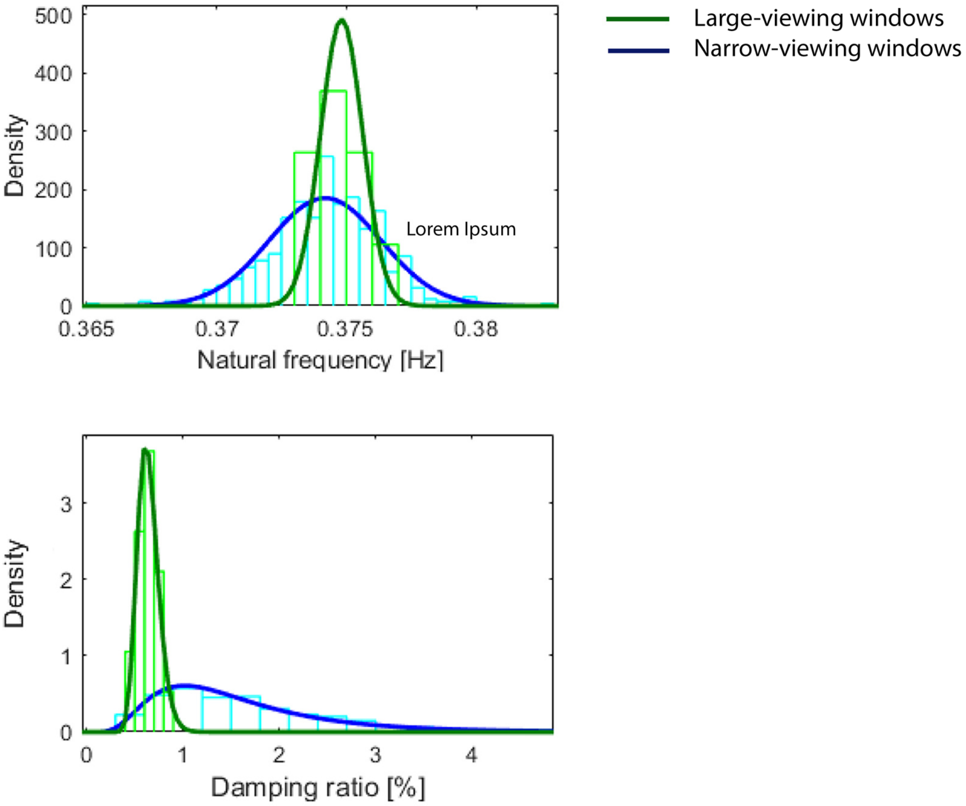

Fig. 2.15 Normal distribution (first natural frequency) and lognormal distribution (first damping ratio)

Table 2.8 and 2.9 show the position and dispersion indices for large viewing windows, which depict the distribution of natural frequency and damping ratio.

By enlarging the observation window, the Gaussian distribution of natural frequencies shirinks around the more frequent value, which is roughly invariant with respect to the length of the viewing window. This proves that the parameters have

Table 2.9 Indices of first damping ratio distribution (large data set)

Position indexes			**Dispersion indexes**	
Mean [%]	**Median [%]**	**Mode [%]**	**Range [%]**	**Variance [%]**
0.64	0.63	0.61	0.44	0.01

been correctly identified. The damping ratio distribution, on the other hand, becomes practically symmetric and shrinks around the smaller more frequent value. Furthermore, two observations can be done if the frequency stabilization criteria are modified to be more restricted for data sets with a few measurements. The first is that the number of sessions from which a parameter estimate is obtained is clearly smaller. The second is that the dispersion range of the two modal parameters is shrinking, and the more frequent value of the two distributions is being shifted to the one displayed for the data set with many recordings. The smaller the allowed uncertainty, the closer the two curves resemble each other. This is evidence of right identification. To sum it up, a larger number of measurements points provides for a more accurate estimate and a smaller scattering range for both parameters. The reference-based stochastic subspace identification, as described in the subsection "Theoretical and practical challenges of data analysis," is one technique to increase the accuracy of modal parameter estimation. The pre-treatment function "project channel" in ARTeMIS can be used to trigger this analysis. Short data sets have been analyzed, and the results reveal a drop in the amplitude of scattering range for both first-mode modal parameters. The amplitude of range is roughly 46 and 40% for first natural frequency and damping ratio, respectively, as compared to findings produced without this approach. Nonetheless, the damping ratio range remains large, and the uncertainty of each estimate in terms of CV appears to have decreased slightly for natural frequency and increased for damping ratio. Finally, the outcomes achieved using such technique for a narrow viewing window are insufficient. When the same investigation has been performed on large viewing windows, no relevant improvements have been found. In conclusion, the usage of a large set of data turns out to be essential for an high quality estimate and limited range of scattering. In this scenario, the minimum and highest range values for the first natural frequency are 0.3736 Hz and 0.3761 Hz, respectively. On the other hand, the first-mode damping ratio ranges from 0.4204 to 0.8656 %.

Validation

The results of the *SSI-UPCX* method have been validated by comparing them to the outcomes of the *EFDD* method for large data sets and first mode. The mode value of the natural frequency distribution increases by about 0.1 percent when using the latter. The damping ratio distribution's mode value, on the other hand, is subject by a 6 percent reduction. For natural frequency and damping ratio, the dispersion around the mean value is nearly the same for both methods. The modal assurance criterion has been used to compare the results achieved with the two approaches in terms of mode shapes. In every case, this index is greater than 90%. In 79 % of cases, it is greater than 99 %, between 97 and 99 % in 16 % of cases, and less than 97 % in 5% of cases. Finally, the findings are affirmatively validated since the differences between the outcomes of the two approaches are very small for all three modal parameters.

2.3.4 Dependence of structural modal characteristics on operational and environmental factors

It is helpful to evaluate the cause of the variability shown by the results. First and foremost, it is critical to determine whether or not each estimate has a high level of accuracy. It must be discarded from the analysis if its uncertainty is too high. Second, considering that considerable structural deterioration and/or degradation cannot occur because the bridge has been recently built and has no design issues, it is pivotal to determine whether the changes in modal parameters are related to environmental and/or operational variables. Environmental conditions (temperature, humidity, rain, and wind) cause normal changes in dynamic behavior, whereas structural deterioration causes abnormal alterations [161].

The recognition and subsequent filtering of environmental effects are of crucial relevance for large civil structures, such as bridges, where output-only analysis is widely used [162], notably for identifying closely spaced modes. Temperature is the most crucial environmental factor for steel structures like the one at stake. As a result, the behavior of modal parameters in relation to it has been studied. For many case studies, the literature [163] reported its effects on bridges. Although the fact that the impact of temperature on materials and structural systems is well understood, reliable quantitative evaluation is challenging, especially given the uneven distribution of temperature in the bridge structure. Temperature and environmental factors can, in fact, cause considerable changes in the recorded properties, i.e., on a magnitude equivalent to or greater than damage. As a result, physical model development is frequently neglected through preference of a black box system identification method. The usage of *SVM* for the Ting Kau Bridge [164] and the implementation of the *ARX* model for the Z24-Bridge [161] are two examples in this regard. It is essential to evaluate the shifting of modal parameters caused by temperature fluctuations in order to carry out a true structural health identification and prevent erroneous condition assessment [48]. Since mode shapes are known to be the least sensitive to environmental changes of the three modal factors, their behavior with regard to temperature variations has been not investigated. Natural frequencies, on the other hand, are the most sensitive [165].

Preliminary study: annual trend

An annual trend has been used to conduct a preliminary investigation to determine how temperature influences structural modes. To begin, each accelerometric acquisition has been assigned to a temperature. The linear interpolation of the bridge surface temperatures that the system measures at 1-hour intervals has yielded the temperature at the moment of the accelerometric data. Then, the measurements' monthly average temperature has been computed. The average monthly temperature (diamonds) and the temperature at the time of accelerometric observations (circles) are shown in Figure 16.a. Figures 16.b and 16.c show the estimated modal parameters of the first mode as well as the estimation errors for the *SSI-UPCX* approach.

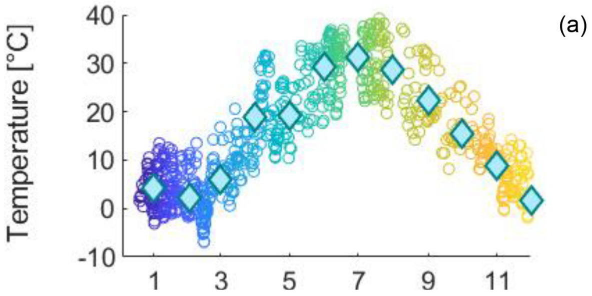

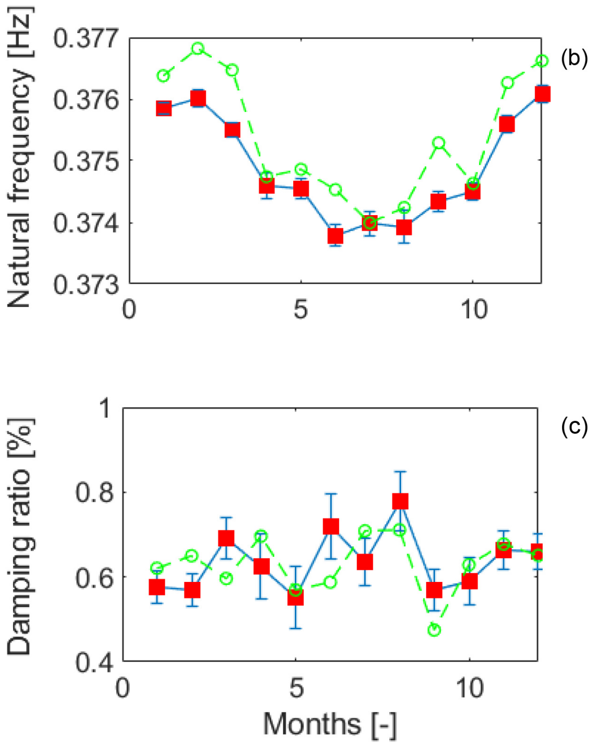

Fig. 2.16 a Temperature in time and average monthly temperature. b, c Monthly modal parameters and estimation error for the first mode

It is noticeable that the first natural frequency has an inverse relationship with temperature. As a result, the colder months have the greatest natural frequencies, and vice versa. The highest variation in the values of the first natural frequency found in this case is on the order of 0.6 percent, which is significantly less than the expected variation (5–10 percent) for large span (100 m or longer) highway bridges [48]. In fact, this latter variation is frequently significant enough to overcome the changes caused by damages [166]. The damping ratio has a complex correlation with temperature, presumably because to its intrinsically more uncertain estimate. Indeed, the average-damping ratio has an oscillating tendency, and the results are essentially superposed when the error estimates are taken into account. In Figure 2.16, the plot in green represents the results achieved with the *EFDD* technique, whereas the blue graph shows the findings obtained with the *DD-SSI-UPCX* method. The results of the *EFDD* approach are qualitatively comparable to those of the *DDSSI- UPCX* method: the relationship of the first frequency with the temperature is validated, whereas damping has a hazy link.

Study of structural behavior for temperature

A more in-depth investigation has been performed based on the preliminary outcomes achieved so far on the correlation between the vibrational first-mode frequency of the structure and temperature. Specifically, the behavior of the first natural frequency and damping ratio for temperature ranges has been studied with 23 temperature bands used to investigate the signals' trend. Each band has a temperature range of around 3 degrees Celsius. Figure 2.17 displays two plots vs the mean temperature of each band and a linear weighted fit of the trend, one in terms of natural frequency and the other in terms of damping ratio. Weights equal to the reciprocals of estimation variances have been employed to consider the accuracy of the points.

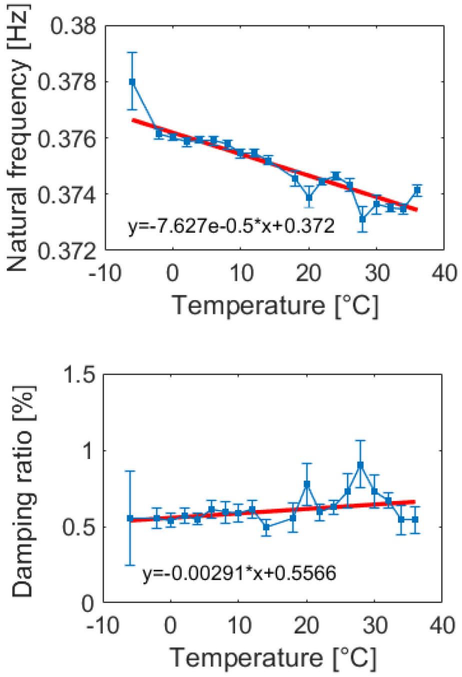

Fig. 2.17 Trend of the first modal parameters over 23 ranges of temperature

The statistic indices concerning the linear fit are summarized in Tables 2.10 and 2.11. For the fit of first natural frequencies, the indices *SSE* (Sum Squared Error, which measures the total deviation of the actual values from the fit) and *RMSE* (Root Mean Squared Error or Standard Error, which is an estimate of the standard deviation of the random component in the data) are significantly lower. As a result, with a slope of 0.0762, the first natural frequency trend can be judged to be obviously declining as the temperature rises. When the temperature is below freezing, this effect appears to be more severe. This behavior is consistent with what has been observed in other investigations [167, 168, 102]. The damping ratio behavior, on the other hand, cannot be deemed effectively rising since the departure from the linear trend line, as indicated by the indices, is too great.

Table 2.10 Indices of linear fit for first natural frequency

SSE	R^2	$AdjR^2$	**RMSE**
0.0107	0.8964	0.8907	0.0244

Table 2.11 Indices of linear fit for first damping ratio

SSE	R^2	$AdjR^2$	**RMSE**
1.4026	0.1989	0.1544	0.2791

Determination of modes

Natural frequency values range from 0.3 Hz to 3 Hz. Nevertheless, the fundamental structural modes are concentrated in the first half of this range. It is feasible to quantify the resemblance between distinct modal shapes using the Modal Assurance Criterion (*MAC*) [49]. The natural frequencies of interest have been zoomed in on. The *MAC* index emphasizes the fact that higher modes have a more complex mode shape, as they resemble lower modes.

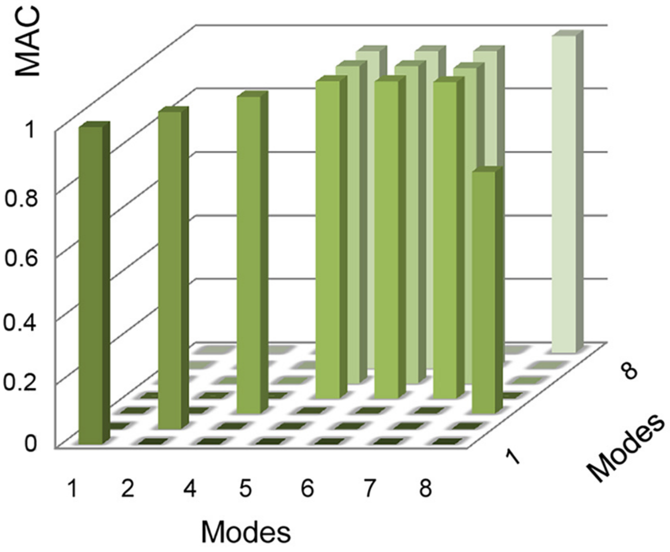

Fig. 2.18 Modal assurance criterion

The similarity of some mode shapes relating to modes with different natural frequencies can also be surmised by observing the tracks of modes depicted by red lines in Figure 2.19. In fact, there is a cross-trend among such tracks/links. The resemblance between the fifth and sixth modes stands evident in large data sets, Figure 2.18. This figure refers to the second large data set in Figure 2.19, which is devoid of the third mode. Yet another finding can be made by looking at the *MAC* graph of a session where the third mode is identified (e.g., sixth session in Figure 2.19). The **MAC** index demonstrates substantial correspondences between this and the first mode in this example.

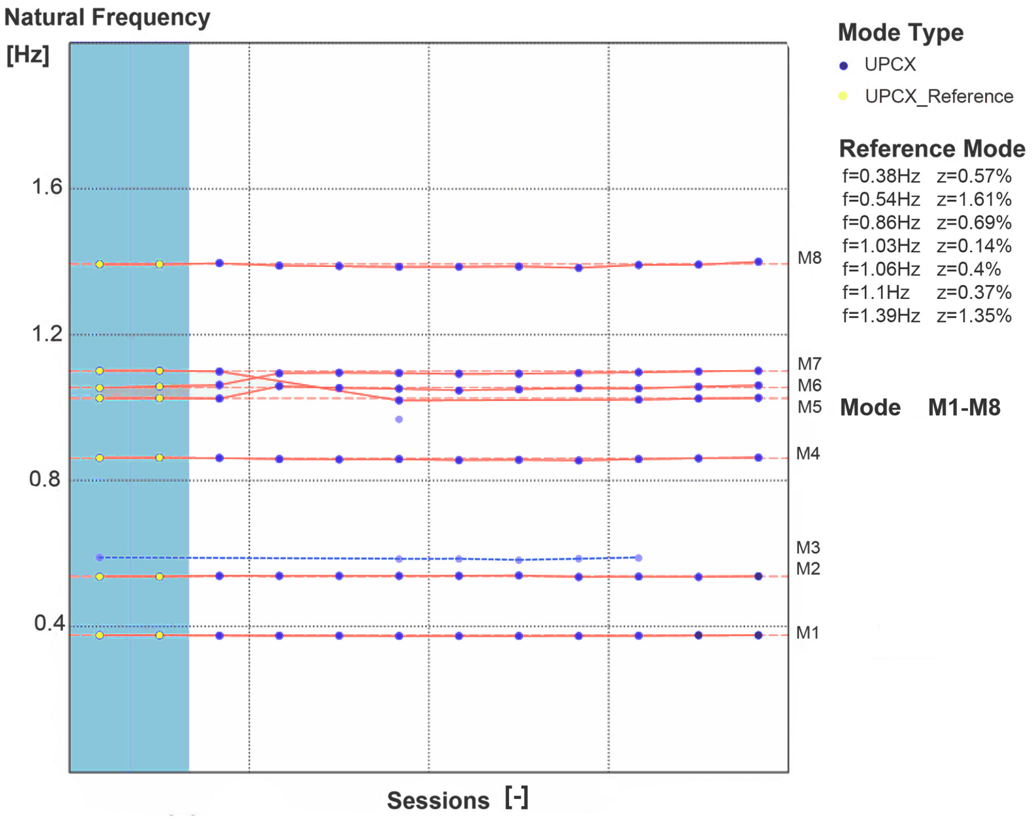

Fig. 2.19 Natural frequency history (12 sessions from the same year)

The components of mode shapes have a real and an imaginary part, by definition. The proportional nature of the damping ratio is reflected in real values. The complex part is caused by:

- non-proportional damping;
- poor measurements or/and poor modal parameter estimation;
- uneven data.

The complexity plot can be used to determine which components of the mode shape are real and which are imaginary. This graph depicts each component of the mode shape with a tip of a vector starting at zero in the complex plan. The real part of the component is represented on the horizontal axis, while the imaginary part is displayed on the vertical axis. The vertical component defines the complexity. All modes, excluding the third, which is emphasized, and the fourth and eighth, which are medium, have a very low factor of complexity for large data sets. As a result, the most of modes are almost fully real, indicating that they are not the result of numerical issues. Figure 2.19 shows the behavior of the natural frequencies of interest as a function of the available sessions, with the natural frequency and the damping ratio of reference modes. With completely visible dots, the graph depicts the modes that are part of the track (continuous red line). The dots in transparency, on the other hand, are not connected to the track. A posteriori, the dashed blue line has been adopted to simply highlight the dots of the third mode.

Furthermore, due to the system's imperfect synchronization of the accelerometer readings (estimated at max 10 ms), an assessment of the potential phase error effects has been performed. The resulting findings have been compared by evaluating several combinations of the available channels, as indicated by the names of the nodes in Figure 2.5. The findings from the channels on the nodes listed below have been evaluated and compared to the results from all channels.

- N.1.;
- N.1. and N.2.;
- N.1. and N.4.;
- N.1. and N.3..

Mode 6 is only obtained if all channels are utilised, according to this investigation. When a portion of the channels is used instead of all of them, the frequency of the first mode increases, with a maximum relative variation of 1.77 per thousand.The fourth digit after the comma is subject to absolute variation. In terms of standard deviation, this order of magnitude is equal to the frequency uncertainty. The average ratio of absolute variation to standard deviation is 3. Concerning the damping ratio of the first mode, the first digit after the comma is subject to absolute variation. On average, the ratio of absolute variation to standard deviation (related to the results of combination with all channels) is equal to 3. According to the dispersion range of the first mode calculated utilizing all channels for the 12 data set (Figure 2.16b, c), it is observed that:

- The highest frequency achieved by employing part of the channels is slightly higher (fourth digit after comma) than the maximum of such range;

- The minimum damping ratio achieved by using only a portion of the channels is extremely near to the minimum of such range.

To summarize, the error owing to imperfect synchronization can be deemed small for accurately identifying vibration modes. Figure 2.20 depicts the trend of the first natural frequency and damping ratio in function to the sessions and the above mentioned channel nodes.

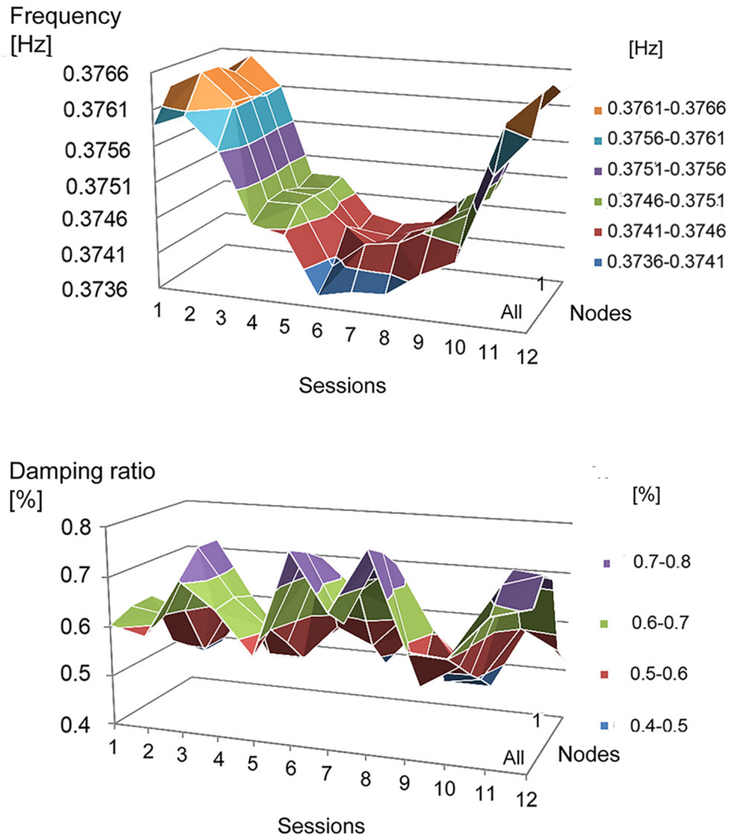

Fig. 2.20 First natural frequency and damping ratio based on measurement sessions and used channels

Figure 2.21 shows the mode shapes for the modes indentified by ARTeMIS, with the exception of the third (since it has high complexity) and the sixth (present only when all channels are used, showing remarkable similarity to the modal shape of the fifth mode but not corresponding to a clear peak of the singular value decomposition).

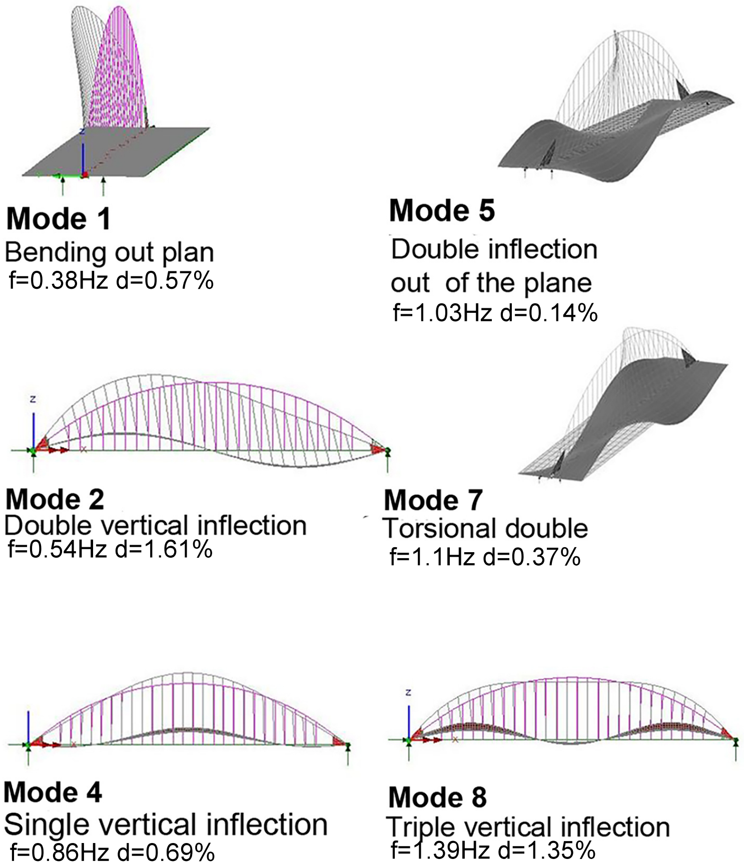

Mode 1
Bending out plan
f=0.38Hz d=0.57%

Mode 5
Double inflection
out of the plane
f=1.03Hz d=0.14%

Mode 2
Double vertical inflection
f=0.54Hz d=1.61%

Mode 7
Torsional double
f=1.1Hz d=0.37%

Mode 4
Single vertical inflection
f=0.86Hz d=0.69%

Mode 8
Triple vertical inflection
f=1.39Hz d=1.35%

Fig. 2.21 Vibration modes (Reference modal parameters from SSI-UPCX method)

2.4 Detection of anomalous behaviour

It has been possible to construct a range that encompassed the environmental variability having the structural response in time in terms of modal parameters. The range of variability of six frequencies are shown in the Table 2.12. The modes under consideration are depicted in the Figure 2.21. Hereafter the term "Mode" will be abbreviated to the letter M.

Table 2.12 Nominal conditions: range of frequency scattering

Vibration Mode	**Bending out of plane**	**Double vertical inflection**	**Single vertical inflection**	**Out of plane double inflection**	**Torsional**	**Triple vertical inflection**
Frequency	**F1**	**F2**	**F4**	**F5**	**F7**	**F8**
min [Hz]	0.373	0.532	0.856	1.044	1.091	1.383
max [Hz]	0.3772	0.540	0.866	1.065	1.105	1.400
Var rel [%]	1.069	1.398	1.167	1.979	1.239	1.238

The nominal conditions boundaries are expressed by the values, maximum and minimum for each range. A deviation from these values indicates an anoumalous behavior. This approach is straightforward but have a critical limitation. The extracted features may appear inside the healthy range in the presence of very small damages (e.g., during the early stages of degradation development). This may be due to environmental factors (temperature, solar radiation, wind velocity, and humidity), operational factors (intensity of traffic flow and potential traffic jam), and errors due to poor data set and limits of processing techniques [169]. The probability density functions of the damaged and undamaged states could, in fact, overlap. The variation owing to *EOVs* (environmental and/or operational variations) is smaller for the analyzed bridge than for other highway bridge case studies [166], but not negligible. Techniques for removing/mitigating *EOVs*, such as regression modeling and machine learning approaches, should be employed to improve the effectiveness of this strategy, however it has been established that successful results can only be produced with a robust data normalization. This is only conceivable in the presence of a big volume [170] and high accuracy of experimental data, both of which are lacking in this case study, hence reliable results cannot be obtained using these approaches. The modal parameters have been extracted by widening the observation window of the signals. This has been the strategy adopted for reducing the variability of the features. The observation window under consideration included 31 signals in all. This has allowed for a more precise estimation of modal parameters, as well as the deletion of several highly uncertain values at the range's boundary. Furthermore, very lengthy records already contain temperature variability which have allowed the structural behavior in the studied temperature range to be smoothed. For very small damage (weak signals), the percentage of signals that do not result in an alarm can be exceedingly high. More over half of the damaged signals, as illustrated below, will not exceed the nominal condition limitations. This means that half of the damaged signals would not be considered damaged, and the damage detection method would be far less sensitive. The percentages of false and missed alarms have been obtained by analyzing signals from intact and damaged structural states. Defining N_d and N_{ud} as the number of data identified as damaged and undamaged and $N_{test\,ud}$ and $N_{test\,d}$ as the number of tested undamaged and damaged data, False (FA) and Missing Alarm (MA) have been computed by means of Equations 2.1 and 2.2, respectively.

$$FA = \left(\frac{N_d}{N_{test\,ud}}\right)100 \tag{2.1}$$

$$MA = \left(\frac{N_{ud}}{N_{test\,d}}\right)100 \tag{2.2}$$

Once define FA and MA, the total error (TE) can be define. It is possible to calculate the total error as the sum of these two terms.

Three potential damaged states have been simulated imposing variations in the acceleration signals. Many of the most harmful structural events, such as cracks, foundation settlements, bearing device dysfunction, and connection losses, imply a change in structural stiffness. A change in the signal frequency is caused by a change in this structural property, which might occur locally or globally. When a stiffness reduction occurs there is a resulting increment of the signal period. Therefore, to simulate damaged signals, a structural response delay (time axis stretching) has been introduced. Other real-world bridge analyses [171, 172, 170], both with real and simulated damages, have been used to determine the magnitude order of a realistic frequency shift caused by a hypothetical structural damage. Notches, in particular, that can simulate minor damage caused by object collisions, corrosion, or overload, result in a natural frequency shift of the order of 0.1-0.5 percent on average. The response in natural frequency that is first investigated is that linked to Modes 1, 2, 4, and 8, see Table 2.13.

Table 2.13 Errors for each natural frequency

Damage Levels	**Severity Degree**	**Signal Variation**	**Error**	**F1**	**F2**	**F4**	**F8**
LD7	LOW	$\sim 0.33\%$	MA[%]	75.0	97.9	62.5	70.8
LD8	MEDIUM-LOW	$\sim 0.66\%$	MA[%]	41.6	75.0	27.1	39.6
LD9	MEDIUM	$\sim 1.0\%$	MA[%]	2.1	35.4	2.1	8.3

The percentage of detected false alarms is zero for all frequencies, except for F2 which shows a value of 12.5 %. To improve damage detection efficacy, a combination criterion based on the alarm trigger when one of the features is outside the ranges indicated in Table 2.12 has been utilized. The contribution of the second mode frequency is the worst in terms of false and missed alarms. When a combination of the four frequencies is evaluated, the second mode contributes to lowering the missing alarm, as shown in Table 2.14.

Table 2.14 Errors for combination F1-F2-F4-F8.

Combination F1-F2-F4-F8	**MA [%]**	**FA [%]**	**TE [%]**
LD7	56.3	12.5	69.0
LD8	14.6	12.5	27.1
LD9	0.0	12.5	12.5

Table 2.15 shows the findings for a combination of F1, F4, and F8 in terms of missing, false, and total errors.

Table 2.15 Errors for combination F1-F4-F8.

Combination F1-F4-F8	**MA [%]**	**FA [%]**	**TE [%]**
LD7	58.3	0.0	58.3
LD8	18.8	0.0	18.8
LD9	0.0	0.0	0.0

Due to the lack of false alarms, the total errors is reduced. Nonetheless, the missing error increases by around 30%, especially for LD8. A large portion of the observed frequencies turns out to be into the healthy condition range for the lowest damage level (LD7). Of course, as can be seen from the comparison of Tables 2.13, 2.14, and 2.15, the percentages of missing alarms fall when the alarm is emitted if only one of the features is outside of the limit values. For the damage level LD8, the drop in missing alarm percentages is more pronounced. To summarize, for this structure and for the specific type of damage, the traditional approach may detect quite well anomalies induced by a damage level equal to or more than LD8, i.e. medium-low damage.

2.5 AI support: K-means algorithm

For very low damage levels, the traditional approach is weakened. Nonetheless, it can evaluate the structural status even when the damage location is unknown a priori and the deteriorated portion is not accessible, making it a useful supplement to visual examination and non-destructive testing.

To satisfy the need for better potential structural damage diagnosis, a special clustering technique has been applied. When the data does not contain labels, a cluster analysis is used to look for groupings of data, or clusters. The data in one group should be comparable (or connected) to each other, but different (or unrelated) from the data in other groups. The K-means algorithm has been chosen and used to solve the problem at hand.

Damage-sensitive features are required for accurate damage detection. As a result, it has seemed appropriate to leave out features that are more sensitive to environmental/operational factors. For several reasons, the contributions of the second, fifth, and seventh natural frequencies have been deemed irrelevant for damage identification. In detail, the fifth frequency has a high relative variation already in the nominal conditions (see Table 2.12), the fifth and seventh modes are closed space modes and therefore readily misidentified, and the second frequency is the least damage-sensitive as highlighted by Table 2.13.

The flowchart in Figure 2.22 depicts the steps of the clustering process, which uses the K-means method to assign a structural "health/damaged" condition to the signals.

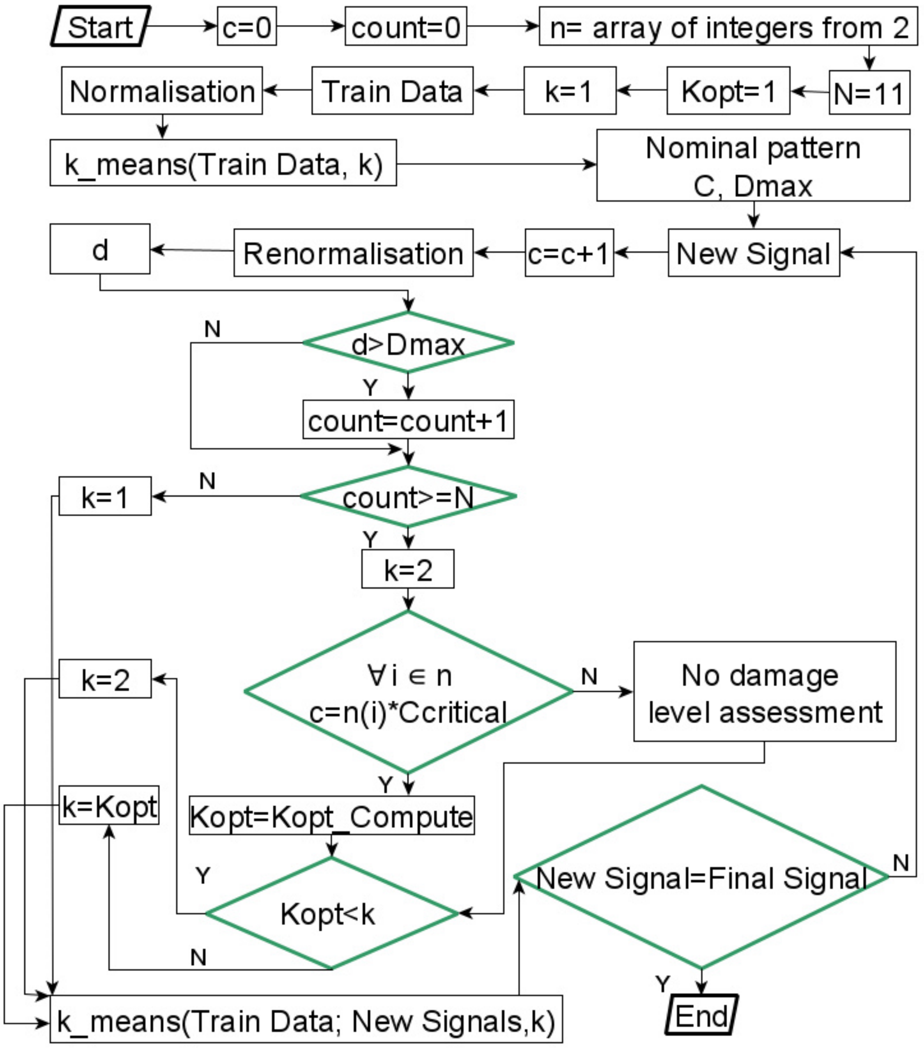

Fig. 2.22 Damage identification flow chart based on the k-means method

K-means is a partitional clustering strategy that is categorized as an unsupervised learning system. It divides data, which is represented by a vector of features, into non-overlapping subsets (clusters). This approach allows for the visualization of similar data in clusters using a specific metric. Its goal is to build data groupings based on the feature vector distances. The requirements for creating clusters include high homogeneity among data from the same group and low homogeneity across data from other groups. Once the number of clusters has been determined, k centers must be located in order to minimize the intra-cluster distance. This algorithm necessitates a significant amount of computation time [127]. Several iterative approaches to quickly converge on an optimum have been developed. One of them [173] has three basic steps:

- Selection of k point centers (k centroids);
- Assign each data/signal to the cluster centroid nearest to it;
- Compute the new k point centers.

As long as convergence is obtained, the last two steps are repeated. The K-means method minimizes the intra-cluster distance at each iteration [127]. A matching matrix can be used to evaluate the algorithm's performance. There are three things that can have a detrimental impact on performance. Indeed, when clusters are of different sizes, densities, and non-globular geometries, K-means performs poorly. Many clusters are commonly utilized to overcome these limits. Another disadvantage of this method is that different initial centers can result in different clusters being generated. It is a good idea to repeat the algorithm numerous times to overcome this difficulty. The most key aspects about the K-means theory can be found in [87]. From the standpoint of *SHM*, the traditional K-means approach allows for the analysis of acquired data/signals and the distinction of two clusters. In the case of a single damage source, one will belong to a healthy condition and the other to a damaged state. This can offer a "snapshot" of the structural condition, but it hinders tracking structural changes over time and possible damage evolution from its early stages before it reaches a critical scale [127]. The procedure proposed in the flowchart (see Figure 2.22)can be used to detect early damage indicators. The first step is to create an undamaged state using *Td* training data, which is represented by one cluster (k=1). The benchmarks that define this nominal condition are its centroid (*C*) and the maximum distance (*Dmax*) from it. Then, one by one, additional signals are analyzed. The counter *c* is updated for each new signal, and the distance (*d*) between the new signal and the nominal centroid is determined. When this value exceeds *Dmax*, the counter (*count*) is increased, highlighting an anomaly. The number of clusters k is set equal to 2 when this value (*count*) equals a persistence number (*N*). To mitigate false alerts, the features of the undamaged pattern and the persistence number are utilized. Indeed, if the K-means algorithm with a number of clusters greater than 1 was used every time a new signal was acquires or when a very small number of signals were showed $d > Dmax$, the number of false alarms would be extremely high, and the data would most likely appear divided into two groups that were not related to healthy/damaged condition but to warm/cool one. When critical time units are reached, a check of the optimal number of clusters is performed to track the evolution of the damage level. *Ccritical* is the number of signals included in a critical time unit. As a result, the critical time unit is a control unit that allows the analysis process to be speeded up by using a discretized computation of the optimal value of k (*Kopt*). On the other hand, it relates to a period of time during which just one level of damage can grow. The initial hypothesis is that the potential damage level in a first critical time unit is one, and there is no verification of the ability of the algorithm to develop a data underlying structure model with a different value of k that is best for the task at hand. The concept that only one level of damage can be present in the first critical unit before verification (e.g. for c=2**Ccritical*, c=3**Ccritical*, etc.) is based on the fact that for the first critical units, the evaluation of some factors such as materials properties, environmental impact, and load is simpler, and the hypothesis made turns out realistic. To sum up, the value of k in the proposed procedure is equal to:

- 1 if $count < N$;
- 2 if ($count >= N$ and $Kopt <2$);
- *Kopt* calculated for $n*Ccritical$ if ($count >= N$, $n*Ccritical < c < n+1\ Ccritical$, and $Kopt >2$), with n natural number starting from 2;

The Matlab program has been used to implement the algorithm. The K-means++ algorithm has been utilized to select the k initial cluster centroids (first step of the iterative process described in the current Section), which optimize the running duration and the final solution [174]. The second and third steps of the iterative approach described above correspond to the so-called *batch updates phase*, which tries to reduce the sum of point-to-centroid distances. This phase can fail to arrive at the correct solution, and it is occasionally followed by the so-called *online updates phase*. The *batch updates phase* is sufficient for the problem at hand, and it is consequently the only one implemented. As a result, the procedure is quick. Among the several distance metrics available, Squared Euclidean distance has been chosen. Furthermore, the default value in Matlab (100) has been selected as the maximum number of iterations to achieve convergence. The empty clusters have been deleted, but the method has been set to keep track of them presence. It's a good idea to repeat the method numerous times with different initial centers to optimize the inter-cluster distance. The argument 'Replicates' has been set to 10 in this case. Data normalization is another crucial factor that should not be overlooked [175]. This is a pivotal pre-processing task since scaling data in a given range ensures that each feature has the same weight. A Min-Max normalization has been used for this particular case. In addition to the issues discussed so far, it is important to dwell on the fact that outliers can distort the right positions of the k point centers, making K-means clustering particularly susceptible to them [176]. The deletion of the outliers has yielded no benefits in the analyzed case. The number of clusters has been set to 1 to learn the undamaged pattern. Table 2.16 shows the normalized location of the centroid as well as the greatest normalized distance (*Dmax*).

Table 2.16 Normalized centroid and maximum distance from it for nominal conditions

M1	**M4**	**M8**	**Dmax**
0.51	0.42	0.47	0.58

When a number *N* of signals has a distance from the normal condition centroid greater than the defined threshold (*Dmax*), the number of clusters k is updated to two. Moreover, some criteria may be used to determine if structural alterations have occurred, which, in the case of early-stage damage recognition, can suggest the progression of negative phenomena over time. They enable the ideal number of clusters (*Kopt*) to be calculated, indicating the presence of a possible damage progression. If this number rises, the damage level is likely to rise as well. The Calinski-Harabasz clustering criterion [177], the Silhouette index [178], the Davies-Bouldin criterion [179], and the gap statistic criterion [180] are among the criteria presented in the literature. The Calinski-Harabasz relies upon the sums of Squared Euclidean distance between the feature vectors and the centroids of the predicted clusters and the optimal value of k corresponds to its maximum value. The Silhouette index evaluates the difference between intercluster distances and intra-clusters distance and the optimum value of k must maximize this index. The Davies-Bouldin criterion utilizes the intra and the inter-clusters distance as well and, for this criterion, the optimal value of k corresponds to its minimum. Finally, the Gap criterion calculates the logarithmic mean of the pairwise distance. In this case the optimum value of k is correlated to the maximization of this criterion. With such procedure, there will not be the need to select damage level thresholds.

The matching matrix has been used to evaluate the accuracy of the proposed methodology and determine whether there are any improvements over the traditional approach. The ability of the algorithm to correctly identify the structural state can be gauged by comparing real and predicted clustered signals. The real and predicted classes of the signal are represented by the rows and columns of the matching matrix, respectively. A combination of test undamaged dataset ($Test_{UD}$) and datasets corresponding to the levels of damage described before have been used for the analysis. Since the amount of signals in all three scenarios is fewer than the assumed *Critical* threshold, the number of clusters utilized is equal to two. The division of the data (signals) for each studied Dataset is shown in Figures 2.23, 2.24, and 2.25. Cluster 1 contains signals from the undamaged state, while Cluster 2 the ones from the damaged state. Both are, of course, connected with a centroid.

- Dataset 1: ($Test_{UD}$) and LD7

  Table 2.17 shows that the total error is similar to that produced by the traditional method (variation of roughly 3%). The error caused by a missed alarm is cut in half at the expense of the false alarm. As a result, despite the error level is still high, the clustering technique results on the safe side.

Table 2.17 Matching matrix Datasets 1

Real Class	**Healthy predicted**	**Damaged predicted**	**TE**
Healthy	68.8%	31.2% (FA)	60.3%
Damaged	29.1% (MA)	70.1%	

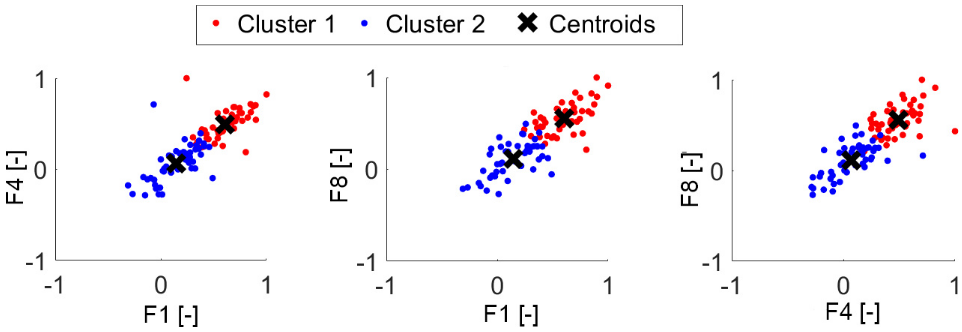

Fig. 2.23 Clustered data (Dataset 1)

- Dataset 2: ($Test_{UD}$) and LD8

  The total error in the shift from Dataset 1 to Dataset 2 is clearly reduced, as shown by the comparison between Table 2.17 and Table 2.18. The total error is increased (by about 50%) as compared to the previous approach, however it is worth noting that the error due to missed alarm is dropped by more than four times. Because around 1/5 of the undamaged signals are labeled as damaged, this strategy is more expensive than the traditional approach in this scenario. The drastic reduction in missing alarm, on the other hand, puts this strategy on the safe side.

Table 2.18 Matching matrix Datasets 2

Real Class	**Healthy predicted**	**Damaged predicted**	**TE**
Healthy	77.1%	22.9% (FA)	27.0%
Damaged	4.1% (MA)	95.9%	

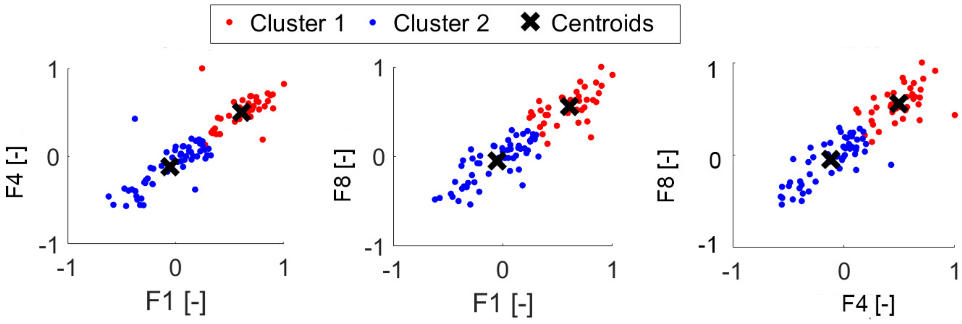

Fig. 2.24 Clustered data (Dataset 2)

- Dataset 3: ($Test_{UD}$) and LD9

  In this case, the cluster strategy performs excellently, although somewhat worse than the traditional approach.

Table 2.19 Matching matrix Datasets 3

Real Class	**Healthy predicted**	**Damaged predicted**	**TE**
Healthy	100.0%	0.0 (FA)%	2.1%
Damaged	2.1 (MA)%	97.9%	

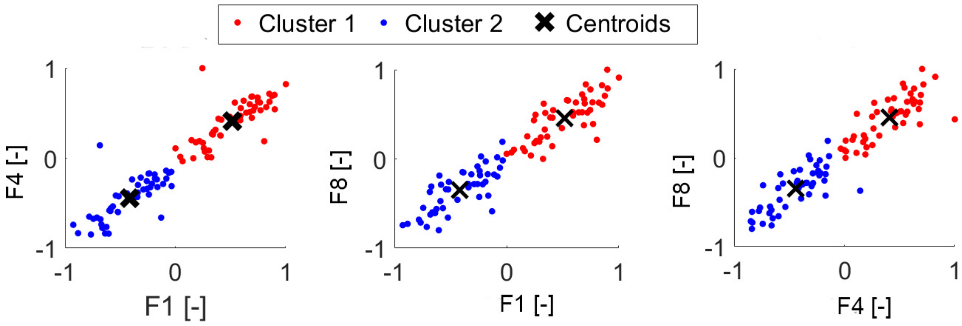

Fig. 2.25 Clustered data (Dataset 3)

When the largest value among the optimal values, computed by means of the three criteria, is employed as the number of clusters, better results in terms of missing alarms have been attained for all three damage levels. The smallest damage level, LD7, has the most significant absolute improvement. Indeed, with LD7, the percentage of errors due to missing alarms drops to 6.25 percent. In comparison to the previous scenario, there is a fourfold reduction. The obtained total error is lower than the previous one, with a value of 52.05 percent. Obviously, the number of false alarms grows. Nevertheless, this growth is much lower compared to the missing alarms errors reduction. These considerations lead to the conclusion that, if the structure is new and the first assumed damage level is low (e.g., LD7 - LD8), the calculation and application of *Kopt* would be reasonable even if the number of signals is less than 2**Ccritical*. Due to the presence of environmental factors, it may be more than 2. The undamaged states measured at high temperatures and the damaged states observed at low temperatures may be similiar. In scenarios where a higher level of damage is promptly present (LD9), however, using the highest value of k results in the worst performance of the algorithm because a little gain in terms of missing alarms is offset by a large rise in false alarms.

To summarize, the K-means algorithm produces promising results, especially for very low damage levels. Its use means a significant reduction in errors caused by missing alarms. It already gives adequate results from a safety standpoint for the damage level LD7. It avoids several missing alarms, at the expense of an increase in false alarms. It is preferred over the traditional strategy for early-stage damage levels because it provides more safety.

The proposed methodology enables the detection of progression and growth of damage phenomena. The optimal value of k is computed when the crucial unit of time is achieved. In the succession of control units, a greater value of k could indicate an increase in the extent of structural deterioration. It is feasible to test the capacity of recognition of rising damage by using the three criteria for calculating the optimal value of k in the analysis of data encompassing all three damage levels (LD7-LD8-LD9). Figure 2.5 shows the findings for the first three time units.

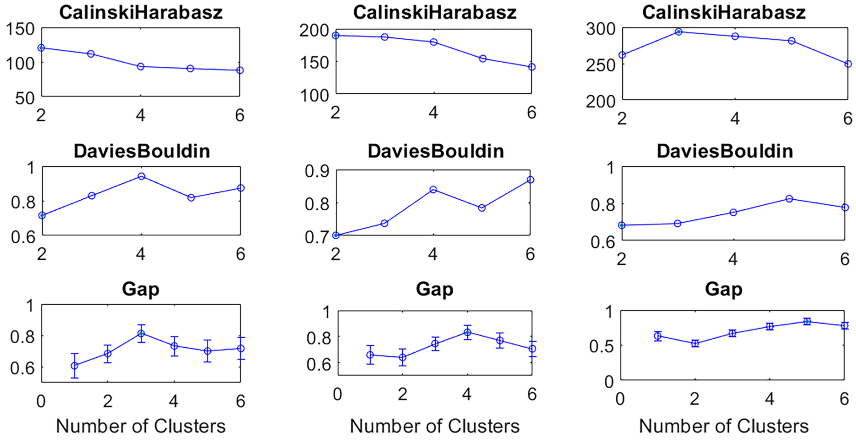

(a) (b) (c)

Fig. 2.26 a) First unit, b) second unit, and c) third unit

2.6 Discussion and results

In this chapter, dynamic data provided during the initial calibration period of a long-term monitoring system on a suspended arch steel bridge has been examined to allow a further validation of the innovative *Active Monitoring* techniques and to lead to operational observations for the purpose of developing successful control strategies. Subsequently, advantages and disadvantages of the two proposed approaches for damage detection have been highlighted.

The merging of the extraction of damage-sensitive features with their accuracy have turned out to be essential. Specifically, one of the factor most affecting the estimation of the features and their uncertainty is the length of the analyzed data set, expressed in terms of number of records. The uncertainty of the features is pivotal because is reflected in the dispersion range of the parameters indicating the undamaged condition of the structure, which can then be utilized to detect damage.

Small errors can be seen in the frequency estimation, but huge errors can be seen in the damping one. According to the literature, errors are bigger for smaller datasets, confirming that having a large number of points per observation is required to produce a narrow range of scattering.

The study of the effect of temperature on modal parameters has certainly highlighted its strong influence on these parameters. Such influence is reflected in the effectiveness of damage detection methods.

Natural frequencies have been chosen for the damage identification purpose because of their low uncertainty. The analysis have aimed to compare the performance of two methods for damage detection using a test sample that incorporates variability induced by environmental effects. The following are the key findings, observations, and conclusions derived from this survey:

- For very small damage levels, the standard technique produces significant errors. Such errors are caused entirely by the worst part of the total error, which is the absence of alarms;
- The clustering strategy outperforms the other method for the studied small damage levels. It greatly reduces the error due to missing alarms but increases the one due to false alarms. From the engineers' perspective, this move is unquestionably beneficial. It is preferable to remedy a false positive through inspections than to fail to detect damage. Of course, false alarms must also be avoided because of the high economic impact. Developments in this direction are planned through the accumulation of a larger volume of data that will allow more accurate results and mitigate environmental effects;
- An additional computational effort in the determination of the optimum value of cluster numbers in the application of the K-means algorithm produces a further improvement in terms of missing alarm errors for very small damage levels. If a high level of safety is required, this clustering strategy is preferred. Another advantage of this method is the ability to track the evolution of the appropriate number of clusters for calculating damage increases. Indeed, a growing value of optimal k over time can be used to infer a change in the data and a probable increase in damage severity;
- Greater data consistency, completeness, and quality would suggest that the clustering algorithm's already excellent performance may be improved. In

crucial cases for the K-means algorithm (clusters with sizes and densities that differ significantly), the importance of the persistence number (*N*) and the optimal number of clusters (*Kopt*) is critical in reducing the expected rise in error in terms of FA and MA;

- The uncertainty in choosing the optimum value of clusters due to the not-perfect correspondence among all the values given by different criterion is a feature that needs to be improved when using the clustering method. Undoubtedly, this, as well as the not-perfect connection between each optimal value and the actual number of data groups, indicates that more performant features be investigated as a future direction for this work. Both the explored approaches would benefit from more effective features. For instance, the Spectral Moments (*SMs*) could be used as damage features with higher signal quality. The high ability of these features, covering the entire frequency range, in identifying small changes between normal and distorted signals has been demonstrated in [176]. Furthermore, the adoption of modal shape indicators such as *MAC* and *COMAC* could be explained by the fact that they are less sensitive to other factors. However, combining various factors could result in more damage-sensitive features.

2.7 Further developments: a numerical modeling for comparison with different damage scenarios

Further developments of the study presented so far concern the quantification and correlation between different real damage scenarios and the changes in the signal resulting from their presence. A numerical model of the structure was used for this purpose and the effect of four different damage scenarios was investigated. Three of them represent local damage and one global damage. Following is a brief description of the numerical model and the obtained results.

2.7.1 Numerical modeling

The finite element model is developed using LUSAS software. Figure 2.27 shows the developed model highlighting some features, among them the constraints. Table

2.20 displays the material and the modeling type element for each structural element. The Young's modulus used for the steel and concrete, the two materials of which the structure is composed,is equal to 209 E3 N/mm^2 and 30E3 N/mm^2. The structural self weight was taken into account for analyzing the structural vibration modes.

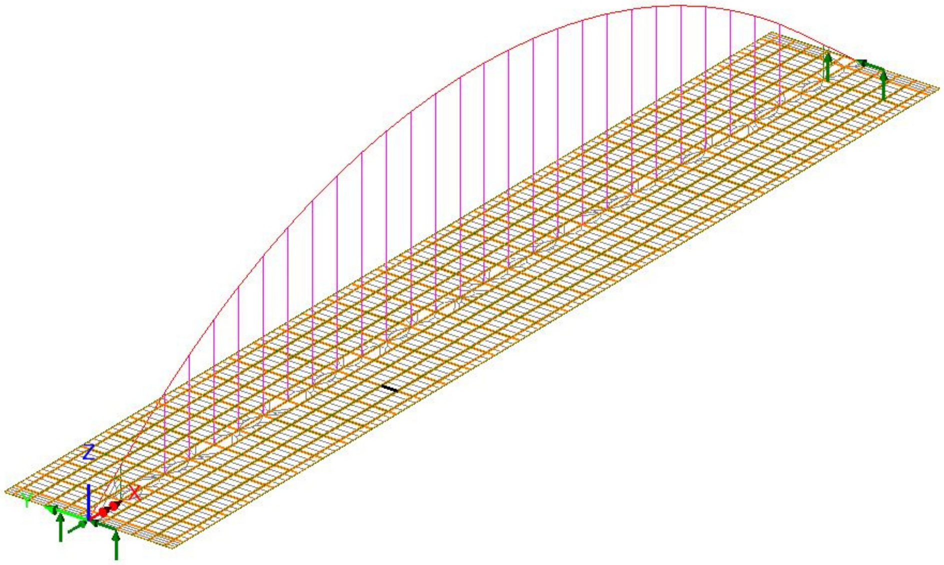

Fig. 2.27 Finite element model

Table 2.20 Model specifications

Structural element	Element type	Material
Hanger	Bar	Steel
Chain beam	Thick beam	Steel
Arch	Thick beam	Steel
Transverse cantilever	Thick beam	Steel
Deck	Thich shell	Concrete
Arch-Chain connection	Thich shell	Steel

2.7.2 Damage scenarios

Four damage scenarios (DS) were explored in depth. Each of them was simulated with a reduction in the Young's modulus of the material of the assumed damaged components. In this way, it is possible to consider two phenomena. The first is the presence of cracks, due for example to the overcoming to the cracking moment owing to excessive loading. The change of Young's modulus, affecting the bending stiffness, will simulate a reduction of the moment of inertia. The second is the presence of corrosion. As reported in [181, 182], there is a degradation of the Young's modulus if the corrosion is presence. In more detail, the pitting phenomenon is particularly impacting.

Equation 2.3 links the Young's modulus of the undamaged material (E_{ud}) with that of the damaged material (E_d) through the factor *perc*. For each scenario, the variation (var) of the frequencies used as damage indicators in the subsection 2.4 with respect to the undamaged scenario was plotted. The results in terms of frequency variation achieved are also discussed with respect to the three damage levels (LD7, LD8, and LD9) simulated in section 1.4.

$$E_d = percE_ud \tag{2.3}$$

The first damage scenario is related to the reduction of the stiffness of the arch-beam chain connection. For the structural type at issue, this type of damage is among the most significant. This is the first investigated local damage problem. Figure 2.28 highlights the greater sensitivity of the fourth frequency (f4) to this type of damage. The impact of such local damage is quite low. Only f4 is able to achieve a frequency shift comparable to the one produced by the lowest level of damage (LD7) simulated in Section 2.4.

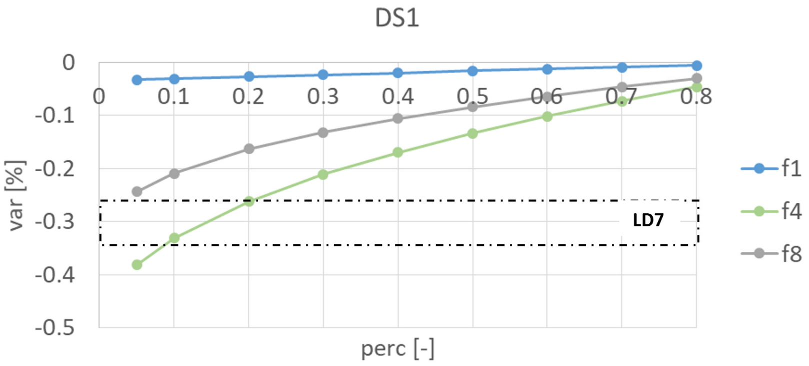

Fig. 2.28 DS1: degradation of arch-beam chain connection

The second damage scenario (DS2) is conceived as an extension of the previous (DS1). It involves not only the arch-chain beam connections but also one hanger per side. The first frequency (f1) shows the same behaviour as in the previous case (DS1), see Figure 2.29. In this scenario, values of the *perc* factor ranging from 0.4 to 0.2 allow the fourth and eighth frequencies (f4 and f8) to attain the damage level LD7. The frequency f8 in the case of almost complete damage (*perc* equal to 0.05) reaches the damage level LD8.

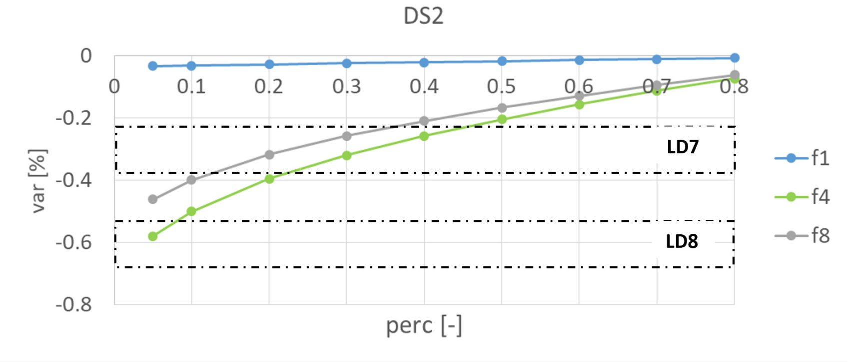

Fig. 2.29 DS2: degradation of arch-beam chain connection and near hangers

The third damage scenario (DS3) concerns damage of three hangers located in the middle of the bridge. As can be seen in Figure 2.30, in this case it was possible to reduce the extent of the damage (the *perc* constant varies from 0.5 to 0.9) and achieve a much higher frequency variation. The fourth frequency (f4) is able to reach the damage level LD9.

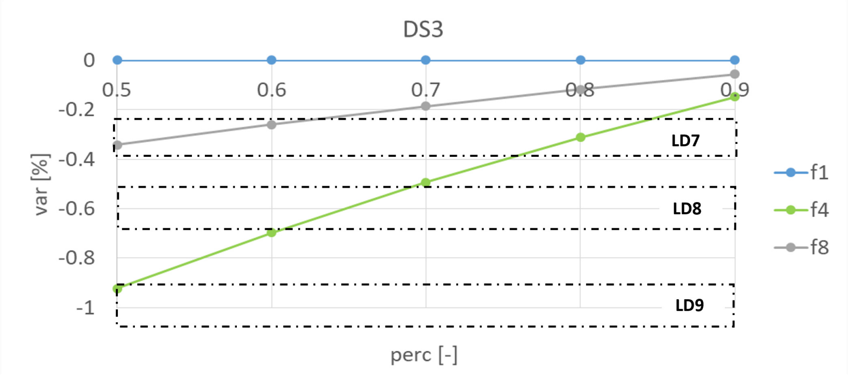

Fig. 2.30 DS3: degradation of central hangers

The fourth explored damage scenario (DS4) concerns about the deterioration of all hangers. Thus, it represents damage that is widespread rather than localised. As can be seen in Figure 2.31, such scenario involves a frequency variation much more marked. The damage level LD9 is achieved by the fourth frequency (f4) with a value of *perc* equal to 0.9 and by the eighth frequency (f8) with a value of **perc** equal to 0.86.

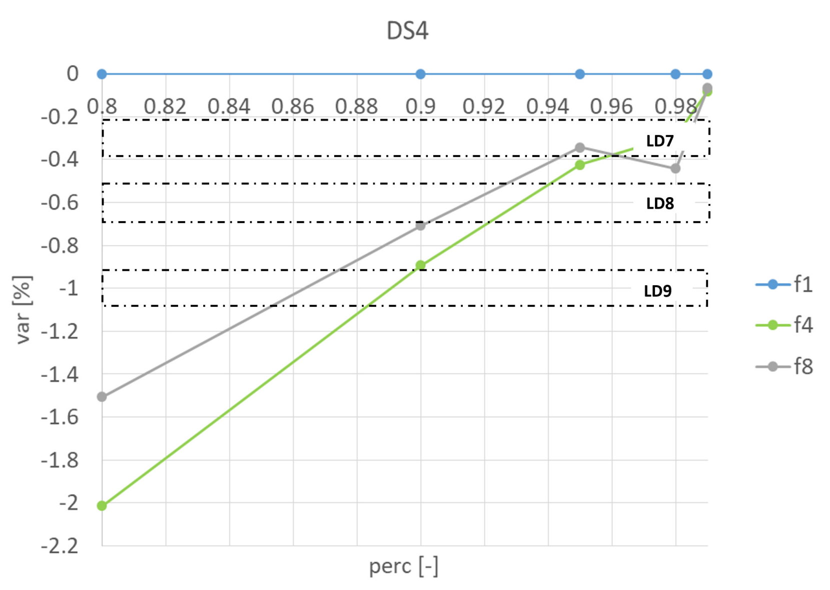

Fig. 2.31 DS4: degration of all the hangers

Chapter 3

SHM strategies for simply-supported prestressed concrete railway bridges assessment[1]

3.1 Problem definition

The most of railway viaducts built in Italy since the second half of the twentieth century are prestressed concrete simply supported bridges. Despite the fact that these are simple structures having verified durability, many degradation phenomena, chemical (carbonation, salt, and acid actions) and/or physical (freeze-thaw cycle, overloading, shrinkage) can occur over time, reducing structural safety.

The taxonomy and classification of degradation processes [183] underline the crucial structural criticalities. Deformation, discontinuity, displacement, loss of material, deterioration [184], transverse and longitudinal cracking, water infiltration, defects in concrete along the cable track, and defects in prestressing cables are just some of the phenomena often occurring in concrete railway bridges. Some of the them are depicted in Figure 3.1. As can be observed, the degree of deterioration

---

[1] Part of the work described has been previously published in:
G. Marasco, G. Piana, B. Chiaia, G. Ventura. Genetic Algorithm Supported by Influence Lines and a Neural Network for Bridge Health Monitoring. Journal of Structural Engineering. (2022).
G. Marasco, F. Oldani, B. Chiaia, G. Ventura, F. Dominici, C. Rossi, F. Iacobini, A. Vecchi. Machine learning approach to the safety assessment of a prestressed concrete railway bridge. Structure and Infrastructure Engineering. (2022)

can be severe, resulting in significant changes of the beam cross-sections geometric parameters.

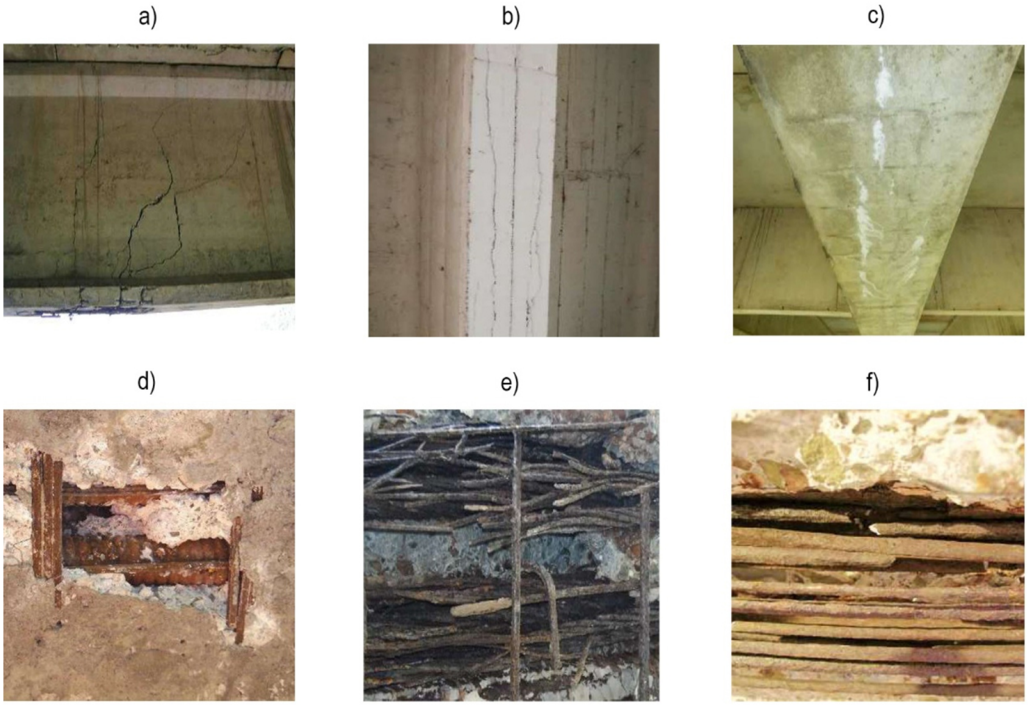

Fig. 3.1 Prestressed bridge damage occurrence: (a) transverse cracks; (b) longitudinal cracks; (c) traces of humidity with efflorescence on the intrados; (d) cavity on the intrados; (e) cables with strands interrupted at the intrados; and (f) corroded and broken wires. (Images courtesy of ANAS Gruppo Ferrovie dello Stato Italiane.)

Some structural components of the deck are more prone to deterioration based on the source of damage. The corrosion phenomena, for example, is more severe and widespread in some sections near elements (e.g., joints, niches, and ducts) where both water and deicing salts are present. To determine which parameters and sections must be monitored, a structural analysis is required. The type, position, and entity of the damage will influence the failure structural modes [185]. Shear failure mode can occur in the worst-case scenario [186], resulting in sudden and brittle collapses.

The challenge that rail infrastructure italian owners face is characterized not only by the high level of attention required by such infrastructures, especially those designed for the passage of high-speed and capacity trains due to the obvious catastrophic consequences that would emerge if malfunctions occurred, but also by the large number of such bridges that require control. As a result, standardized techniques that are both valid for the whole typology and economically viable must be developed. For an effective data-driven decision-making operation and maintenance, ($O\&M$) such techniques should have high precision and low detection times [54]. As stated following, the monitoring architecture and acquisition processes have been created to suit both safety and cost-effectiveness requirements.

The structure under investigation, as well as two approaches that have been proposed, will be discussed following. Both have involved static data and have been designed to be complementary. The first has been developed for a long-term monitoring (Section 3.2); the second for a periodic one (Section 3.3).

3.1.1 Description of the structure

The Oglio Viaduct, a railway bridge near the A35 BreBeMi highway in northern Italy, has been the subject of the investigation. It allows the railway line to travel above the homonymous river. It is part of the Brescia-Treviglio high-speed-high-capacity rail route, which is one of the Mediterranean Corridor parts that will connect Western and Eastern Europe. It is 1287 meters long and is composed of 43 spans of around 30 meters each. Figure 3.2 depicts a general view of the bridge. Each bridge span is a grillage with four longitudinal 2.5 meter high prestressed beams and five diaphragms that are simply supported by the piers. Two overhangs with service paths may be seen on the top slab.

Fig. 3.2 General view of the Oglio Viaduct

The viaduct piers have a circular shape with a diameter of 4 meters and are connected at the top with a pier cap on which the spans rest. To avoid scouring at the foundation, the foundation pile caps are buried. Figure 3.3 shows an elevation view of the span between viaduct piers 3 and 4.

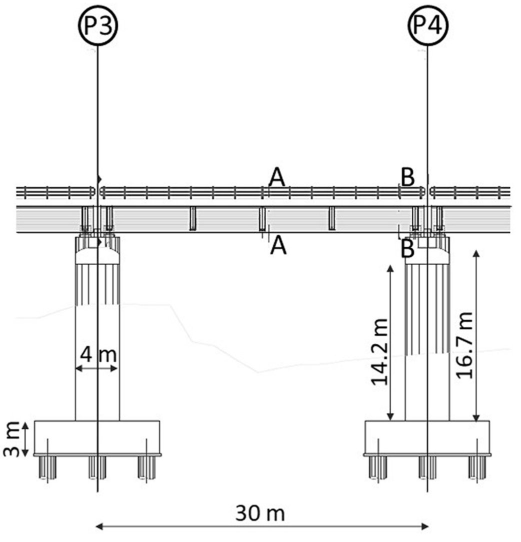

Fig. 3.3 Elevation view of the Oglio viaduct

3.2 Data anomaly detection for a continuous condition assessment

To face the problem described in the Section 3.1, a data anomaly detection methodology for a continuous condition assessment has been proposed. The use of a monitoring capable of capturing potential structural anomalies through parameters recorded at a non-high frequency is part of an economically viable, widely deployed, reliable, and repeatable approach to continuous infrastructure assessment.

Data anomaly detection and condition assessment are interconnected engineering concept. In the field of anomaly detection by data analysis, many approaches can be found in the literature. A brief survey of the approaches proposed in the literature to date is given here to highlight the contributions in this field, their strengths and limitations, especially with respect to the case study addressed here. It’s worth highlighting some recent and interesting research using dynamic features for anomaly identification and condition assessment [187–189]. They have been challenged with detecting six different forms of anomalous data patterns (e.g., missing, mirror, outlier, square, trend, and drift). The first utilizes a Random Forest classifier with a "Shapelet transform," the second uses GAN and CNN, and the third employs CNN for image classification. All of the approaches achieve high accuracy. Nevertheless, they may not be appropriate in all cases (e.g., different structural typologies, materials, and recorded parameters). Catching drift, for example, will not suffice in the case discussed in this chapter because the occurrence could be caused by both anomalous phenomena and not. In addition to studies performed in a dynamic field, the literature includes research based on static measurements, albeit on a smaller scale. [57]. [190] presented a system that uses high frequency recorded strain data to catch the passage of vehicles. As a baseline for structural assessment, it establishes live load stresses, load distribution factors, and neutral axis position in healthy conditions. This intriguing approach is not applicable to the case study discussed here, because it optimizes and stores data over time using a much lower sample rate. In a similar manner, for a steel girder assessment, [191] proposed to capture the structural response to load passage rather than the one to environmental conditions. Time series strain data, on the other hand, has been utilized to map the strain responses with temperature. For a tied arch bridge built 14 years before the monitoring system installation, [120] has utilized a linear regression model. There are no time-delayed structural phenomena, and no pre-processing approaches are needed, as in the current investigation. Correlation models between temperature and static stresses of a steel truss arch bridge have been used to define the healthy condition for damage detection goals in [192]. Time-delayed phenomena are also negligible in this investigation, and there are no methods necessary to ensure data repetition. The use of CV and ML-based methodologies must be included for a complete up-to-date summary [24]. Although they are capable of accurately detecting multipattern anomalies in *SHM* data, their applications are limited due to the existence of extreme condition and damage data.

The proposed methodology and the monitoring architecture exploited to solve the specific issues highlighted by the case under study, representing the structural typology to which it belong, will be illustrated in the following sections.

3.2.1 Monitoring architecture

Rete Ferroviaria Italiana (RFI) has devised and implemented a long-term structural health monitoring system for the Oglio Viaduct. Its goal is, in particular, to use static measurements to show the bridge's temporal evolution under environmental conditions and to issue warnings for abnormal values of recorded parameters. It is not intended to capture the effects of train transit because its aim is not to record the structural response associated with operation loads, which would necessitate a high signal sampling rate. To measure important characteristics in different areas of the structure, sensors such as strain gauges, displacement meters at supports, clinometers, surface and air thermometers have been utilized. In the hierarchical monitoring scheme depicted in Figure 3.4, they are labeled level 4. The UAD (Data Acquisition Unit), the PPF (Fixed Peripheral Places), and the PCS (Satellite Central Place) are the higher levels of the hierarchy.

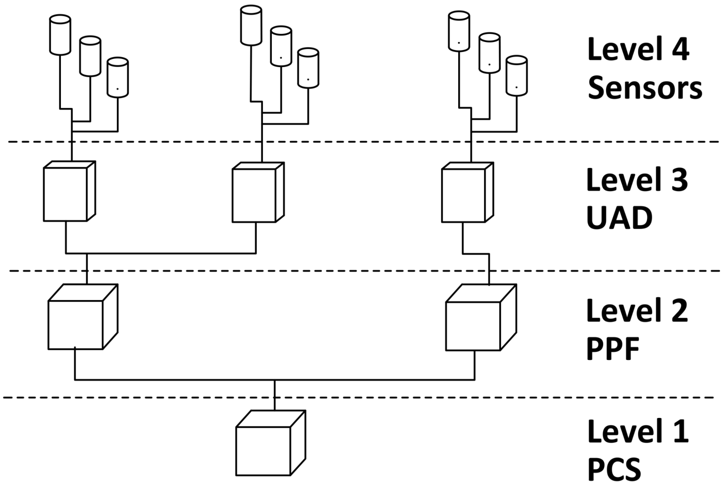

Fig. 3.4 Hierarchical monitoring architecture

After the system installation, the recorded data from sensors has been compared in real time to expected values determined by structural monitoring experts, and design thresholds (DT) have been established. The further step, developed and presented in this chapter, is the definition of correlation models to outline the real structural behaviour to define data-driven undamaged condition thresholds (UCT). The structure, which has been in operation for nearly six years, was tested using modular railway trains with a maximum axle load of 40 tons to simulate the maximum action that the viaduct can withstand. Moreover, diagnostic trains traveling at 300 km/h were used to test the railway superstructure. The viaduct is periodically inspected in the railway superstructure with diagnostic trains and visual inspections throughout its life. Evidence from periodic and supplementary checks is fed into the Domus-Inrete 2000 information system, which also monitors and point out the structural state. The data recorded on the structure has been correlated with an healthy structural condition due to the lack of the observed structural anomalies. The data used to create the correlation models, see Figure 3.5, are related to sensor places in two specific meaningful sections: A-A (midspan) and B-B (support).

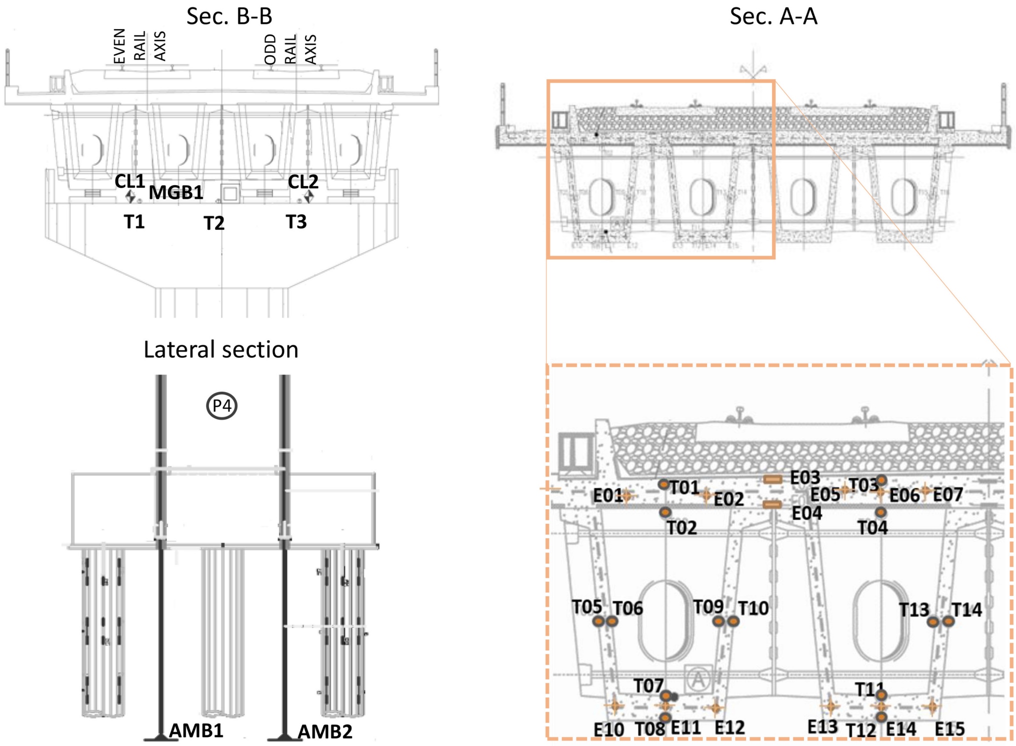

Fig. 3.5 Network of sensors

The symbols used to label the sensors are listed in Table 3.1.

Table 3.1 Symbols

Symbol	**Sensor**
T	Thermometer (temperature of the material or of the air)
E	Strain gauge
CL	Clinometer
MGB	Biaxial support displacement
AMB	Single-base Measurer of settlement

The main features of the employed sensors is provided below. As regards the strains measurements, vibrating wire strain gauges that may be mounted using mounting blocks with rebar-bolts on concrete surfaces have been used. In addition to being cast into concrete structures, such immersing strain gauges are also provided as "shot crete" models with movable tensioning collars. When pulled, a tensioned wire vibrates at its resonance frequency. The strain in the wire is linked to the square of such a frequency. The vibrating wire strain gauge is made to keep a wire in tension between two end blocks that are anchored to the structure. The wire is pulled by an electromagnetic coil assembly, which subsequently sends a frequency signal back to the readout devices. The tension of the wire and its resonance frequency are affected by the structure's deformation, which changes the distance between the two end blocks. The transmitted signal is then scaled to microstrain units. Besides, a built-in thermistor in the strain gauge offer temperature information for understanding potential thermal effects. Table 3.2 summarize some of the main characteristics of such sensors.

Table 3.2 Technical specifications of strain gauges

Description	**Value**
Resolution	$< \pm 1.0 \mu\varepsilon$
Coil resistance (nominal)	150 ohm
Embedded thermistor type	NTC (Negative temperature coefficient) 3kΩ
Embedded thermistor accuracy	$\pm 1C$ ($\pm 0.5C$ within 0-50 °C)
Power supply	Automatically selected by readout (max 40V)
Coefficient of thermal expansion	12×10^{-6}/°C
Temperature range	-20°C+80°C
Max. cable length to logger	1000 m

As regards temperature measurements, thermometers encased in an impact-resistant stainless steel body to be immerged in concrete have been used. Table 3.3shows their technical specifications.

Table 3.3 Technical specifications of thermometers

Description	**Value**
Resolution	0.1°C
Material	stainless steel
Temperature range	-30 °C+80 °C with standard cable
IP Class	IP68 up to 2.0 MPa

As regards the rotations, MEMS analogue surface clinometers have been utilized. They are instruments designed for point inclination measurements in civil works requiring high performance. The used clinometers boast exceptional performance both in terms of accuracy and in terms of stability and thermal variation. Table 3.4 reports their main technical specifications.

Table 3.4 Technical specifications of clinometers

Description	**Value**
Resolution	0.01 % FS
Sensor mechanical bandwidth	
Offset temperature dependency (from -20°C to +70°C)	$\pm 0.003°C/C$
Power supply	from 18 to 30 Vdc
Temperature operating range	(from -30 °C to +70 °C)

Finally, as regards the joint expansion, crackmeters have been used. They are designed to track motions across surface joints or cracks, primarily in concrete buildings or rocks. A vibrating wire or potentiometer displacement transducer is what makes up a crackmeter. It is enclosed in a stainless steel telescopic housing with two fixing connections. Such connections have self-lubricating ball joints that enable lateral movements of up to 10 degrees in orthogonal planes (Y-Z axis) without affecting how the jointmeter functions.

3.2.2 Methodology

In the work presented in this chapter the sensor data have been analyzed using the novelty detection approach [193] for data anomaly detection. Two factors support the decision to perform the analysis using such method. First of all, no real data about the structural damage is available. Second, the development of damaged structural data through simulation can be unreliable in terms of the types of potential structural anomalies. Indeed, if a classification model is trained to recognize only some types of anomalies, it may be unable to detect others. As a result, the models are designed to detect anomalies of any typology, and damage types are not classified. The used method is based on training machine learning regression models on a data set related to health conditions in order to determine the correlations between parameters designated as independents (inputs) and the ones designed as dependents (outputs). The independent and dependent parameters are chosen based on physical cause-and-effect relationships. These models are validated using another set of data for the undamaged structure (the error validation set), after the training. The model predicts the outputs starting from the inputs of such a dataset, and the error (residual) can be calculated as the difference between the measured and predicted outputs. The window of error dispersion is thus characterized by its mean (μ) and standard deviation (σ). The alarm threshold (UCT) are defined by the expression $\mu \pm k\sigma$, where k represents a controlling parameter. Such thresholds, produced using the methods discussed above, reflect the intact structural status and are highly dependent on the parameter k, whose value is determined from a range of statistically significant values depending on the type of problem. The range of k values used ranging from 2 to 3. Values out of "healthy condition error range" are considered anomalies. If the residual had been used as a damage index, as in the standard signal reconstruction approach, there would be a lot of false positives. The moving median of the residuals with respect to the seven preceding days has been used to solve this problem. With such method, an anomaly is identified if at least 50% of the signals in the previous week show an error that falls outside the threshold. Seven days is deemed a long enough period to filter out false alarms but short enough to report timing anomalies. Under certain conditions, this approach is a highly effective filter for reducing false positives when residuals oscillate in sign beyond the stated thresholds. Such damage index smooths the peaks of residuals, making structural health monitoring more helpful for real use and lowering maintenance costs.

It's worth mentioning the pre-processing procedure, which relies on z-score normalization with regard to a moving time window. The min-max, z-score, and decimal scaling are three of the most frequent data transformation normalization methods. The z-score method stands out as it figures out the issue of not knowing the series' minimum and maximum values, but it can only be used on stationary series. Most structural quantities time series are non-stationary, as in other areas such as finance and economics [194]. This behavior is amplified for specific materials, such as concrete, which show delayed phenomena (e.g., fluage). A sliding window approach has been used to successfully tackle non-stationary problems. In this scenario, the input and output time-series values (v) have been normalized using the formula 3.1, where (μ) and (σ) and are the mean and standard deviation derived on the data from the preceding temporal window, respectively. Following the use of the normalized value v' in the machine learning algorithm, the data have been rescaled in their original range 3.2 using an inverse z-score normalization post-processing technique.

$$v^{'} = \frac{v - \mu}{\sigma} \tag{3.1}$$

$$v = \sigma v^{'} + \mu \tag{3.2}$$

3.2.3 Correlation model

Three regression correlation models have been created based on data acquired during the initial service years of the structure to assess such main aspects: unloaded deck strains, pier displacements and rotations, and deck-support displacement in response to environmental variables. For each problem, many machine learning algorithms (e.g., Extreme Gradient Boosting Machine, Multi-Layer Perceptron, LSTM, Bayesian Ridge Regressor) have been investigated. Due to the continuous nature of the data, the problems are formulated as regression models. They are designed to connect inputs and outputs recorded at the same time rather than forecast outcomes at later times. Those that produced the best regression model on the error validation set in terms of Mean Absolute Error and Symmetric Mean Absolute Percentage Error have been chosen and displayed in the following subsections. For two of the three tasks, such methods have been shown to be remarkably successful (subsection 3.2.4 and 3.2.5).

Following is a brief overview of the models that have produced the best outcomes. The Extreme Gradient Boosting Machine (*XGBoost*) is the first model. The term 'boosting' refers to a set of methods that help weak learners become strong, as introduced in the subsection 1.4.2. Boosting is an ensemble strategy for improving any learning algorithm's model predictions. The approach is non-parametric, therefore it can handle huge, complex datasets without imposing a complex parametric framework. Gradient Boosting works by adding predictors to an ensemble in a sequential order, each one correcting the preceding one and attempting to fit the new predictor to the residual errors created by the prior predictor. *XGBoost* is a special version of the Gradient Boosting approach that uses the strengths of the second order derivative of the loss function, L1 and L2 regularization, and parallel computing to give better approximations. The Multi-Layer Perceptron (*MLP*) is the second model. McClelland and Rumelhart proposed it in 1986 [195]. It's a type of artificial neural network, that is made up of artificial units accepting several inputs from data or other neural network units, and that can model exceedingly complex functions. Equation 3.3 describes the process that occur to each unit. The output (y) of the MLP neuron is obtained after a weighted sum plus bias ($W$is the set of weights in the layer and b is the bias vector) and the application of an activation function (f).

$$y = f(Wx + b) \tag{3.3}$$

The output is subsequently transmitted to another unit in the subsequent layer of the network. The network's weights and thresholds must be tuned to reduce the network's prediction error defined by the loss function. The training methods, which employ stochastic gradient backpropagation as an iterative methodology, play this role.

3.2.4 Assessment of the midspan strain of the unloaded deck

Problem definition and data analysis

The evaluation of the strain state of the deck is critical for avoiding some structural issues. Deformations are, in fact, an indication of likely cracks or pretension losses. The parameters recorded in the midspan section have been used to create the correlation model for the healthy condition 3.5.

Table 3.5 Input and output parameters for correlation model

Input	**Output**
Air temperature (T1, T2, T3)	Strains at intrados of the midspan section
Mean$_{ET}$= mean [T01, T02, T03, T04]	
Mean$_{IT}$=mean [T7, T8, T11, T12]	
Tot$_G$=Mean$_{ET}$-Mean$_{IT}$	
E$_G$= mean [T01, T02]-mean [T7, T8]	
I$_G$=mean [T03, T04]-mean [T11-T12]	
$[T01-T02]$	
$[T03-T04]$	
$[T7-T8]$	
$[T11-T12]$	
Additional temporal features	

The definition of independent parameters has been the first stage in developing a correlation model that connects strain values to factors that produce them in an undamaged structural status, based on the designed monitoring system. Temperature, temperature difference (gradient), pier rotations, and train transit all contribute to the strain data. The last element has not been considered for a multitude of reasons. High-speed train strains are characterized by a high frequency and a smaller magnitude than those induced by absolute temperature and temperature gradient [192]. Aside from that, the monitoring system, as pointed out in Section 3.2.1, is not designed to measure the effects of train passage, as records are made every 2 or 4 hours. The influence of pier rotations has also been overlooked. This is due to the limited amount and quality of available data. There are three categories of input: raw, processed, and additional. The term raw refers to unprocessed sensor readings (e.g., air temperature). The term processed refers to the result of combining several raw inputs (e.g., mean sensor data). Additional refers to features that are not directly related to sensor readings. Additional temporal features are the hour of the day (Equation 3.4 and 3.5) and the week of the year (Equation 3.6 and 3.7) when the data were recorded.

$$h_s = sin\left(2\pi\frac{h}{24}\right) \tag{3.4}$$

$$h_c = cos\left(2\pi\frac{h}{24}\right) \tag{3.5}$$

$$w_s = sin\left(2\pi\frac{w}{52}\right) \tag{3.6}$$

$$w_c = cos\left(2\pi\frac{w}{52}\right) \tag{3.7}$$

Those properties are encoded using sine and cosine functions of the values to ensure time data continuity and periodicity. The hours (h) values are in the range [0-24[, whereas the weeks (w) values are in the range [1-52]. The model uniquely identify such two parameters by applying Equations 3.4 and 3.5 to hours and Equations 3.6 and 3.7 to weeks. Figure 3.6 shows the sine and cosine values for the 24 hours of the day, as well as an example of the values (h_s and h_c) generated for a chosen hour (e.g., 10 a.m.).

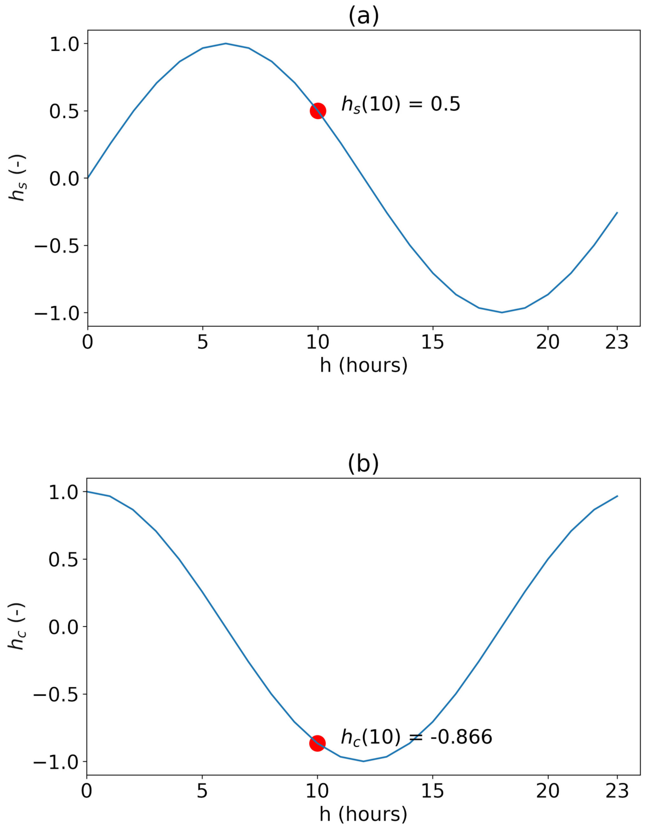

Fig. 3.6 Functions for getting the additional temporal features (e.g., hour of the day). a Sine function; b Cosine function

Only raw outputs have been used as outputs of the system. The input-output data trends are shown in Figure 3.7.

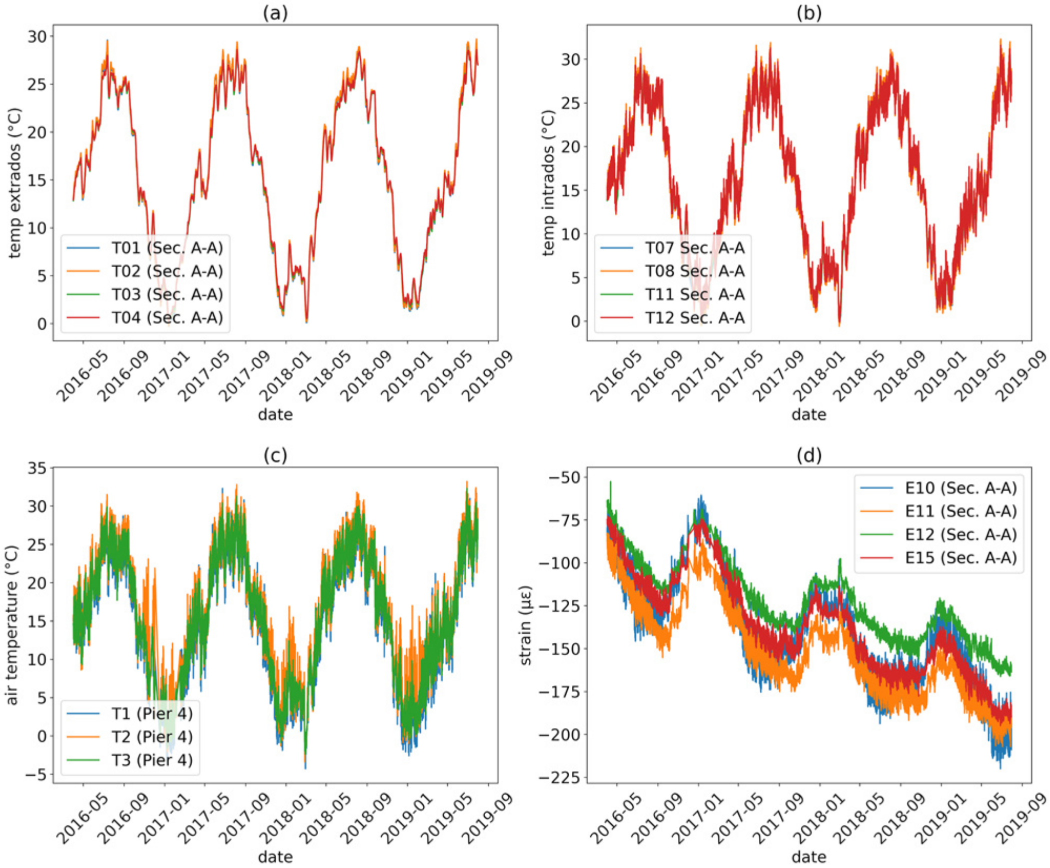

Fig. 3.7 The correlation model's input and output parameters. a Temperature extrados; b Temperature intrados; c Air temperature; d Strain

It is helpful to look at the change of the strain over time from a structural standpoint. Seasonal changes cause significant time fluctuations, as predicted. Furthermore, the seasonal impacts of the thermal inertia of the deck (for example, the effects of a hot summer are reflected until early autumn periods) are observable because strains follow a sawtooth wave pattern. In fact, the behavior of the strain is roughly opposite that of the temperature, but during time intervals in which the temperature is sufficiently high (summer), the reduction of strains manifests itself as a very modest downward trend, practically constant. As a result, the observed strains in autumn are lower than those recorded in spring at the same temperature. This is why the temporal features, which indicate the hour of the day and the week of the year, have been provided as inputs of the correlation model. Of course, there are other phenomena that occur over time: shrinkage and creep [196–198]. They justify the downward trend of the strains. Other complementary effects, such as those caused by non-ideal mobile supports and sensor drift over time, should also be addressed, but these are typically difficult to determine.

Model and pre-post processing operations

A z-score normalization for input and output time-series with respect to the previous 60 days has been executed as a pre-processing operation. The normalization period has been set to account data seasonality. This has allowed the data to obtain repetition in time. As seen in Figure 3.8, the moving window normalization has led the creation of a stationary time series.

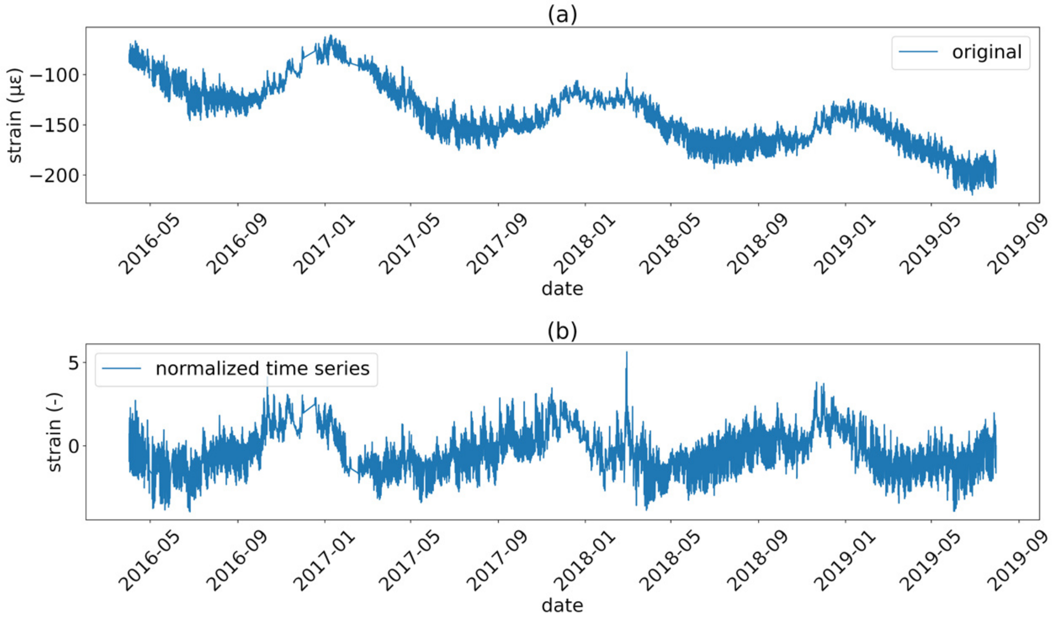

Fig. 3.8 Signal E15. a original series; b normalized series

Then, as regression models, many supervised learning techniques have been used. The best results have been attained by two of them (Extreme Gradient Boosting Machine and Multi-Layer Perceptron). The Extreme Gradient Boosting model [199] has been implemented using decision trees with a maximum depth of 6. To improve model accuracy, the Gradient Boosting approach has been utilized with a learning rate of 0.3. The Multi-Layer Perceptron, on the other hand, has been made up of two hidden layers, each with 30 and 20 neurons. As a criterion, the Mean Square Error (*MSE*) has been used. The Adam algorithm has been utilized as an optimizer. The learning rate has been set to 0.001 and the maximum number of epochs has been set to 400, with a batch size of 16. After that, the data have been rescaled in their original range using an inverse z-score normalization as a post-processing operation. Figure 3.9 shows the strain values over time and the whole set being divided into three parts: train (50 percent), validation error (20 percent), and anomaly test (30 percent).

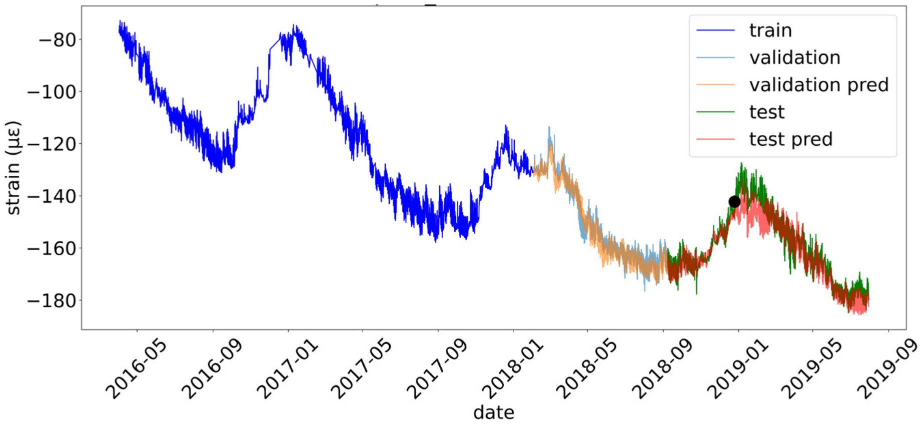

Fig. 3.9 Strain. Signal E15. Subdivision into train, validation error and test anomaly set

After the model has been trained, the validation error set has been used to compute the mean and standard deviation of the residual, which have been then used to establish the healthy condition error range using UCT thresholds. The residual is calculated as the difference between the measured (x_r) and predicted (x_p) outputs after the post-processing step. Table 3.6 shows the values of three indices calculated from the validation error set for both the Extreme Gradient Boosting Machine and the Multi-Layer Perceptron in order to assess model accuracy.

MAE (Mean Absolute Error), SMAPE (Symmetric Mean Absolute Percentage Error), and R^2 (Coefficient of determination) are the indices employed . They have been used to determine which signals have been better forecasted and to measure the reconstruction accuracy. Low MAE and SMAPE values, as well as high R^2, are related with better model performance.

Equations 3.8, 3.9, and 3.10 provide their formulations.

$$MAE = \frac{1}{n}\sum_{1}^{n} abs(x_p - x_r) \tag{3.8}$$

$$SMAPE = \frac{\sum_1^n abs(x_p - x_r)}{\sum_1^n (x_p + x_r)} \tag{3.9}$$

$$R^2 = 1 - \frac{\sum_1^n (x_p - x_r)^2}{\sum_1^n (x_r - \overline{x})^2} \tag{3.10}$$

The predicted value is x_p, the measured (actual) value is x_r, and the average of the values is $\overline{x}$.

The Gradient Boosting approach has achieved higher results on average, by combining numerous decisional trees, in comparison to the Multi-Layer Perceptron and other regression models (e.g., LSTM, Bayesian Ridge Regressor). Due to the general poor outcomes, the latter ones were not included in this chapter.

Table 3.6 Models evaluation metrics (validation error set)

	MLP			**XGBOOST**		
Sensors	MAE ($\mu\varepsilon$)	SMAPE (%)	R^2 (-)	MAE ($\mu\varepsilon$)	SMAPE (%)	R^2 (-)
E10	3.560	1.046	0.794	**3.022**	**1.020**	**0.965**
E11	2.956	0.844	0.667	**2.217**	**0.770**	**0.951**
E12	1.744	0.613	0.764	**1.545**	**0.610**	**0.97**
E15	**1.829**	**0.558**	0.701	1.879	0.600	**0.966**

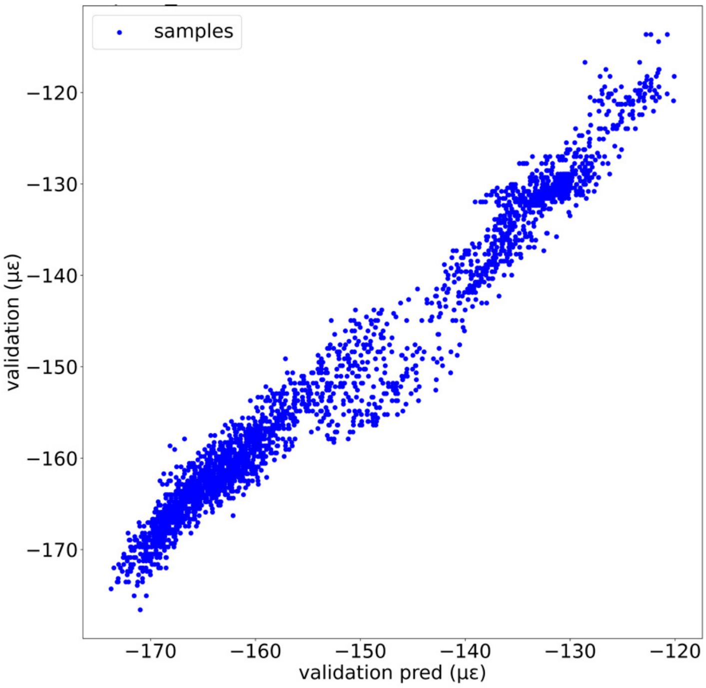

Fig. 3.10 Scatter plot E15. (validation set)

The following investigations have been concentrated on the sensors with a Coefficient of Determination near to 1 (greater than 95 percent). Figure 3.10 shows a scatter plot of predicted and real values from one of these sensors (E15), which helps to display the accuracy of the prediction.

Simulation of anomalies and damage identification

To evaluate the damage detection ability of suggested method, simulated anomalies have been used. They have been created by simulating sensor values with a given offset. In the first instance, the order of magnitude of the range of variation of the anomalies was estimated by considering a widespread deterioration of the materials that may be accentuated by prestressing losses that could bring the intrados into a tensile state. This offset starts from zero and increases linearly in time up to the given value in three considered different time spans (168h, 336h, and 720h). As a result, each anomaly is defined by two parameters: its amplitude (offset) and the time it takes to reach that offset. The dependability of the proposed approach has been tested by changing the starting point of the anomaly. A total of fifteen points from the test anomaly set have been used.

The anomaly plot (Figure 3.11 a) depicts the imposition of an offset equal to 10 $\mu\varepsilon$ on the signal of the sensor E15 achieved in 168 hours. The black dot represents the beginnings of the anomalous signal. Figure 3.11b zooms in on the test set to illustrate the biggest discrepancy between the signal and its forecast near the anomaly's beginning point. The residual plot (Figure 3.11c) shows the trend of the residual (red line), the damage index (median), and the "healthy condition error range" (orange band) for the test anomaly set. The residual error has a Gaussian distribution with a mean close to zero, and is stated as the difference between the measured output and the predicted one after the post-processing operation. To establish the extremes of healthy range (UCT), the value of k has been fixed to two for the sensors E10, E11, E12, and E15. The blue dashed circle in the residual graph indicates the identification of the anomaly. The damage index in that area exceeds the healthy condition error range's control limit.

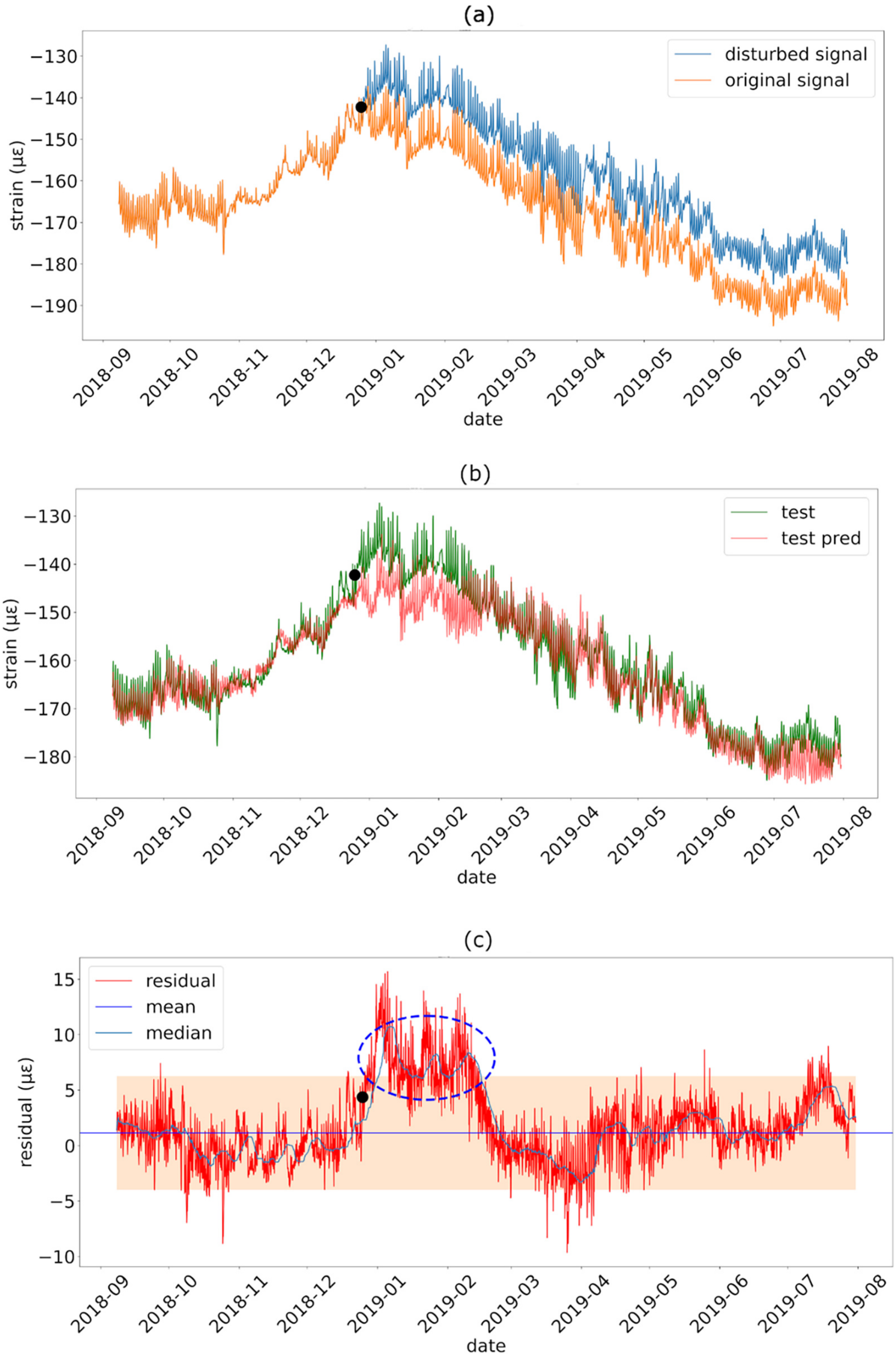

Fig. 3.11 a Anomaly plot; b Test set; c Residual plot

Tables 3.7 and 3.8 summarize the findings in terms of detected anomalies, which are expressed as a function of their amplitude and time period, using a ratio between the number of detected anomalies and the total number of evaluated anomalies (15).

Table 3.7 Percentages of detected anomalies. Damage detection range definition: [80%, 100%]. [40%,80% [, [0%-40% [. Damage detection colours definition: green, yellow, red.

	E10				**E11**		
Amplitude $[\mu\varepsilon]$	Peak reach time [h]			Amplitude $[\mu\varepsilon]$	Peak reach time [h]		
	168	336	720		168	336	720
2	0%	0%	0%	2	0%	0%	0%
10	53%	46%	40%	10	100%	80%	67%
15	93%	80%	60%	15	100%	100%	100%
20	100%	100%	87%	20	100%	100%	100%

Table 3.8 Percentages of detected anomalies. Damage detection range definition: [80%, 100%]. [40%,80% [, [0%-40% [. Damage detection colours definition: green, yellow, red.

	E12				**E15**		
Amplitude $[\mu\varepsilon]$	Peak reach time [h]			Amplitude $[\mu\varepsilon]$	Peak reach time [h]		
	168	336	720		168	336	720
2	0%	0%	0%	2	0%	0%	0%
10	100%	100%	87%	10	93%	87%	73%
15	100%	100%	100%	15	100%	100%	93%
20	100%	100%	100%	20	100%	100%	100%

The approach successfully highlights anomalies corresponding to about 10% of the average signal value. Small anomalies that evolve over a long period of time are clearly difficult to recognize. It's worth noting that, aside from the ability to detect anomalies, there are no false positives. With the exception of E11, no false positives were found. There is a systematic inaccuracy for E11, most likely due to significant irregular local volatility (heteroscedastic time series). Starting from the results, it is possible to classify the damage detection capability as: good, mediocre, or poor (see Tables 3.7 3.8) The tables caption provide the percentage range and color corresponding with each of these categories.

The capacity of the undamaged condition-based thresholds (UCT) to detect early-stage anomalies has been proved to be better to the design-based thresholds (DT). These latter are determined by factors stemming from the expected structural behavior. The design alert values are set to 100% of the calculation value chosen as the limit based on the maximum stresses during the service phase. The alarm values are the 120% of such limit value. For the sensors E10, E11, and E12, the design specifies alert and alarm thresholds of $103.5\mu\varepsilon$ and $124.2\mu\varepsilon$, respectively. For the sensor E15, the such thresholds are set to 230.25 $\mu\varepsilon$ and $276.3\mu\varepsilon$. The improvement in detection capability achieved using this approach is evident. Ideed, the detected anomaly by the UCT is of the order of $10\mu\varepsilon$. Figure 3.12 turns be out very useful to compare the anomaly detection capacity of the two methods. An anomaly (violet signal), characterized by a 15 $\mu\varepsilon$ offset and a 168-hour time span, is imposed on the signal captured by E15. As can be seen, the red and yellow horizontal lines that show the design-based alarm and alert levels are beyond the disturbed signal. Therefore, they would not have detected such anomaly. The damage index used for the second approach, instead, exceeds the UCT thresholds, allowing the anomaly to be detected. As a result, the data-driven strategy is much more successful.

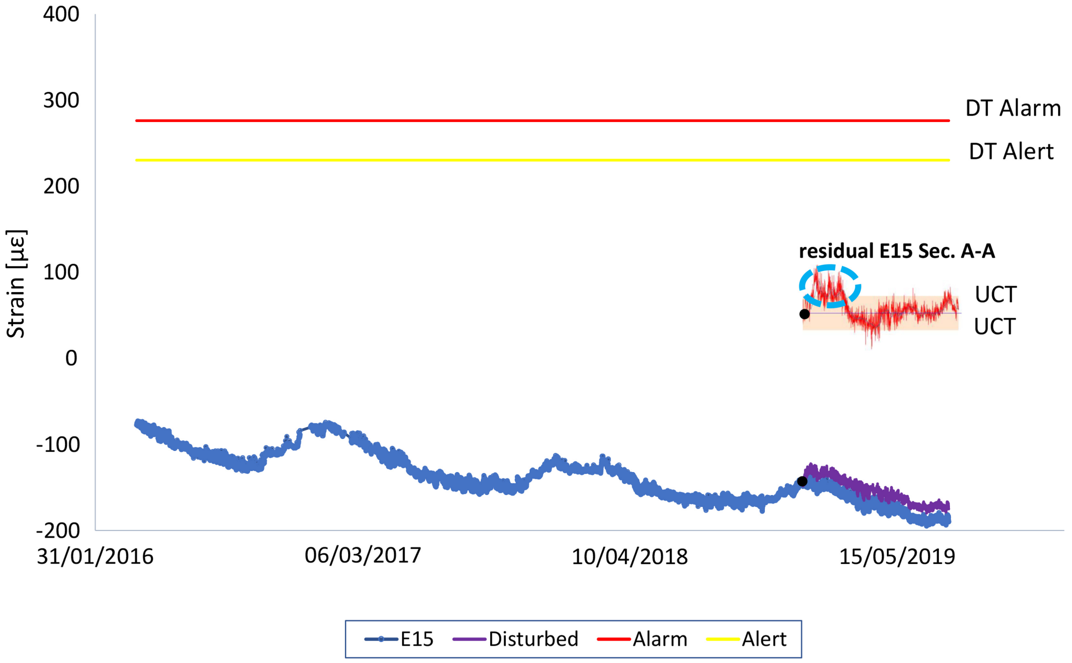

Fig. 3.12 Design thresholds (DT) and undamaged conditions thresholds (UCT)

3.2.5 Assessment of pier rotations and joint expansion

Problem definition and data analysis

Understanding the occurrence of unusual pier movements and anomalous motions in the deck plane requires a thorough examination of pier rotation and deck-support displacement. The development of correlation models for the healthy condition have begun with the assumption that clinometers and measurements of deck-support displacement reflect the temperatures in an unloaded structural condition.

The average air temperature, the rotations recorded by the clinometers, and the hour of the day corresponding to the recorded parameters are all used as inputs in these models. In more detail, the acronyms CL CHA and CL CHB correspond to rotation in the longitudinal and transverse directions, respectively, on clinometers CL1 and CL2 (Figure 3.5). Due to poor signal quality, recordings of channel CL1 CHA were not considered as model input.

Figure 12 depicts the longitudinal rotation recorded by the CL2 CHA sensor. As output data, the correlation models use the data collected by the biaxial joint gauges.

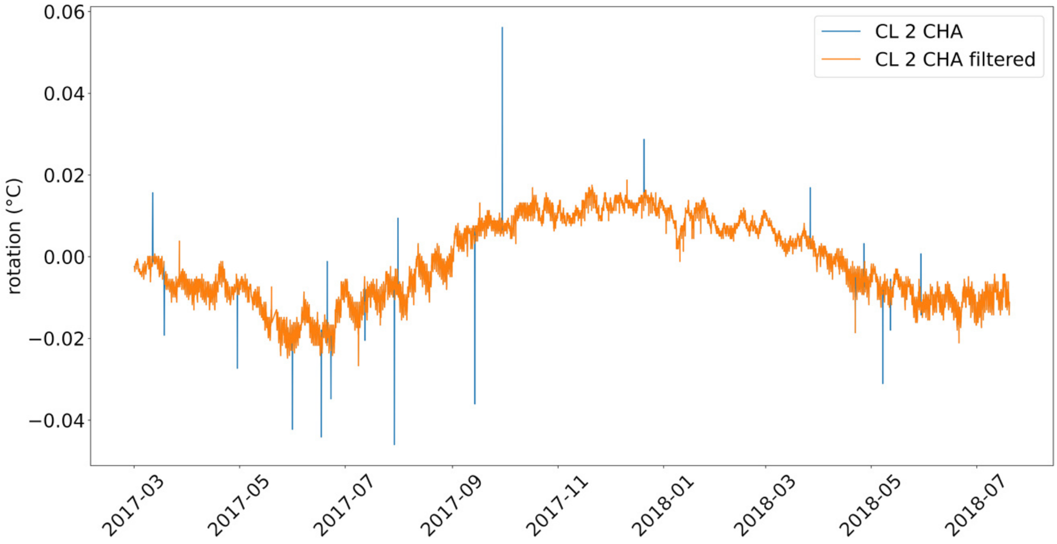

Fig. 3.13 Longitudinal rotation CL2 CHA: original (blue) and filtered (orange) signal

Table 3.9 shows the parameters that have been used to create the correlation models in the healthy state.

Table 3.9 Input and output parameters for correlation model

Input	Output
Mean air temperatures (T1, T2, T3)	
CL1 CHB	MGB1L
CL2 CHA	or
CL2 CHB	MGB1T
Additional temporal features	

Figure 3.14 shows the time trend of the signals from the sensors MGB1L (longitudinal) and MGB1T (transversal), as well as the three-part partition of the dataset. It should be noted that from an engineering point of view the two sensors are different. The first measures the displacement of the deck to the support in the direction of the viaduct axis. The second one in the transverse direction. The latter shows measurements with a very small range of variation due to the layout of the constraints on the internal beam supports which block transverse displacements.

Model and pre-post processing operations

A data cleaning procedure has been performed on the data to remove outliers in the signals (see Figure 3.13). Subsequently, for input and output time-series, z-score normalization based on the previous 60 days has been executed as pre-processing operation. Subsequently, several regression models have been utilized. The Extreme Gradient Boosting Machine and the Multi-Layer Perceptron were among the best-performing ones. To optimize the findings, two sub-models related with the Multi-layer Perceptron have been used to predict the signal recorded by the transversal sensor (MGB1T) and the longitudinal one (MGB1L). The use of different parameters for such two sensors is the mirror of their distinct characteristics. The learning rate and the maximum number of epochs are two hyperparameters that distinguish these two sub-models. They have been fixed to 0.001 and 400, and 0.002 and 100 for the transversal and for longitudinal sensors, respectively. The output data have been subject to an inverse z-score normalization, as post-processing operation, after using the regression model. Table 3.10 compares the two models with better metrics (the corresponding sub-models of the MLP and the Extreme Gradient Boosting Machine).

Table 3.10 Models evaluation metrics (validation error set)

	MLP			**XGBOOST**		
Sensors	MAE (mm)	SMAPE (%)	R^2 (-)	MAE (mm)	SMAPE (%)	R^2 (-)
MGB1L	**0.003**	**0.042**	0.0666	0.666	0.075	0.533
MGB1T	**0.002**	**1.435**	0.806	0.002	1.875	**0.903**

The Multi-Layer Perceptron performs better in this scenario.

Simulation of anomalies and damage identification

The methodology to set the healthy condition error range, to simulate the anomalies and to assess the ability to detect them in terms of percentages has been the same described in the subsection (3.2.2) and subsequently deepened and applied in the subsection (3.2.4). The value of k used to fix the healthy error range boundaries, namely the UCT, has been set equal to 2.5 for MGB1T and 3 for MGB1L. This is owing to the ability of the system to detect little anomalies, albeit a larger healthy condition error range that allows for the minimization of false positives. There were zero false positives for both sub-models utilized for the problem at hand. Table 3.11 displays the results in percentages of detected anomalies as a function of amplitude and time span. The findings indicate a good, mediocre, or poor ability to detect damage. The table caption provides the percentage range and color corresponding with each of these definitions.

Table 3.11 Percentages of detected anomalies. Damage detection range definition: [80%, 100%]. [40%,80% [, [0%-40% [. Damage detection colours definition: green, yellow, red.

MGB1T				**MGB1L**			
Amplitude [mm]	Peak reach time [h]			Amplitude [mm]	Peak reach time [h]		
	168	336	720		168	336	720
0.005	60%	47%	0%	0.008	80%	80%	80%
0.008	100%	100%	87%	0.01	100%	100%	80%
0.01	100%	100%	87%	0.04	100%	100%	100%

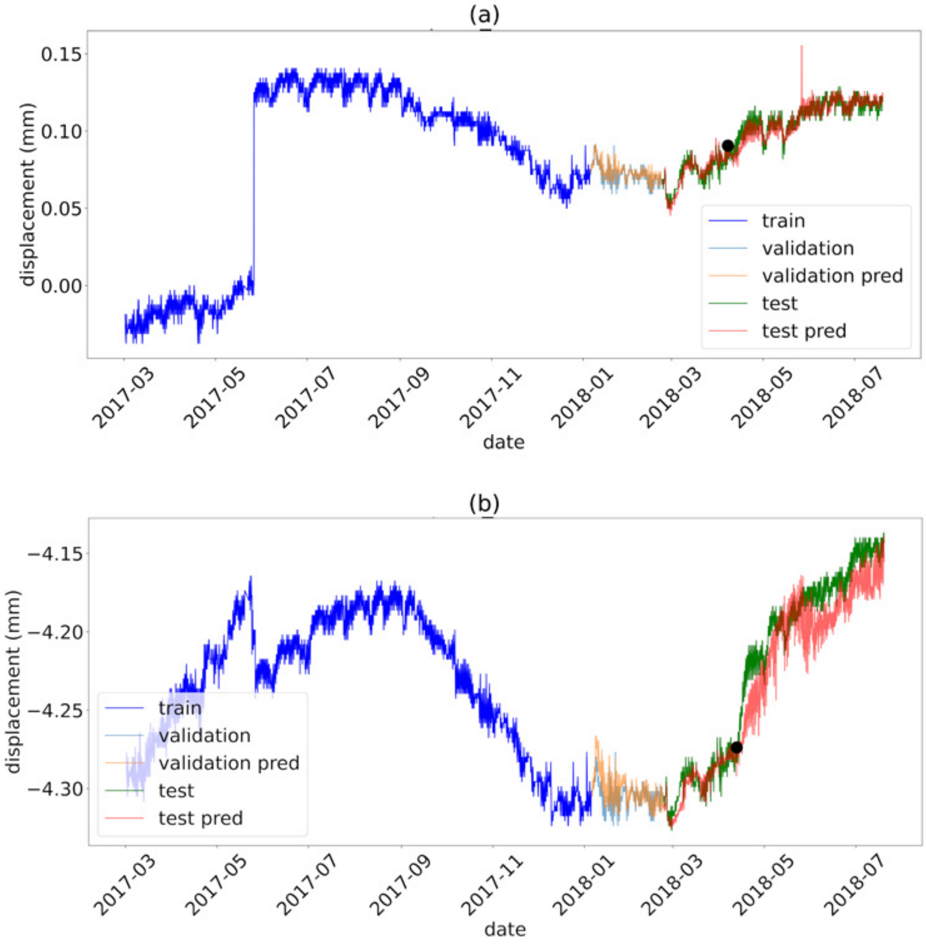

Fig. 3.14 Displacements. Subdivision into train, validation error and test anomaly set a Signal MGB1T; b Signal MGB1L

The results, for both MGB1T and MGB1L, have been good. MGB1T produces successful findings from an anomaly with an amplitude of 0.008 mm, which is around 10% of the mean value of the signal. The damage detection ability for the MGB1L sensor is substantially higher, as the findings are already acceptable for a 0.008 mm amplitude anomaly, which is around 2‰ of the average signal. Even if we just assumed the damage detection ability to be reliable for anomalies with an amplitude of 0.04 mm or higher for MGB1L and 0.01 mm for MGB1T, it would turn out to be much higher than the one depending on the design threshold (DT). In fact, the alert and alarm levels for MGB1L and MGB1T are respectively ± 170.9 and ± 205 millimetres and ± 60 and ± 72 millimetres. In this case the alert values for the design thresholds are the joint excursion values calculated in the two directions in the presence of an earthquake. The alarm thresholds are 120 percent of these values, as in the preceding scenario.

3.3 Genetic algorithm supported by influence lines and a neural network for bridge static periodic assessment

The methodology presented in this Section investigates the use of fewer sensors/measuring points to achieve satisfactory results in damage identification. Structural evaluation is the result of periodic monitoring in which few static parameters are measured when an external load is in various positions over the structure. Analyzing measurements taken at different times under the same conditions can reveal information about potential structural changes. The study presents a hybrid technique using a genetic algorithm, influence lines, and a neural network to tackle the inverse problem of localization and severity estimation of the damage. In the first phase, influence lines are used to obtain information about the damage position [200]. Then, a genetic algorithm (*GA*), which is at the base of the technique, estimates bending stiffness along a discretized structure by means of static characteristics recorded at a few points (i.e. midspan deflections and end rotations). The choice to use of a limited number of parameters, distributed to capture potential changes both in the middle of the beam and near the supports, is due to the optimization perspective in which the methodology has been designed. An increase in parameters would mean greater methodology redundancy and reliability but also higher costs and calculation time. The information obtained in the first phase has main benefits. First, it decreases the number of design variables of the algorithm and, as a result, the computational time. Second, it increases the accuracy of the GA's solution by allowing a properly trained neural network to determine the optimal values for the GA's cost function coefficients. The adoption of a cost function made up of components with variable sensitivity to damage locations allows power coefficients to be used to weight the various contributions. The method has been applied to a simply supported beam with damage scenarios characterized by localized reductions in bending stiffness (approximately from 5 to 40%) to first validate the overall strategy (influence lines, genetic algorithm, and neural network) to an elementary test problem. The bending stiffness reduction can be associated with more or less severe damage caused by corrosion (especially in the sections near the joints where water infiltration is more present), cracks (most likely in the mid-span section), defects in the concrete along the development of the cable, defects in the pre-tensioning cables, and loss of material. The effectiveness of the suggested approach with the use of real values has been verified by using data from the structure under consideration as model data. Numerical experiments have been also carried out to test the technique when the beam length and geometric parameters are altered.

In this preliminary study, only longitudinal flexural behavior has been investigated. The single longitudinal beam-slab system (interior beam in Figure 3.15) has been considered for the analyses. Its undamaged bending stiffness is $EI =$ 9.407 $10^{10} Nm^2$ (Young's modulus $E = 36.280^9 Nm^2$, area moment of inertia $I =$ 2.593^4);the length is L= 27.8 m.

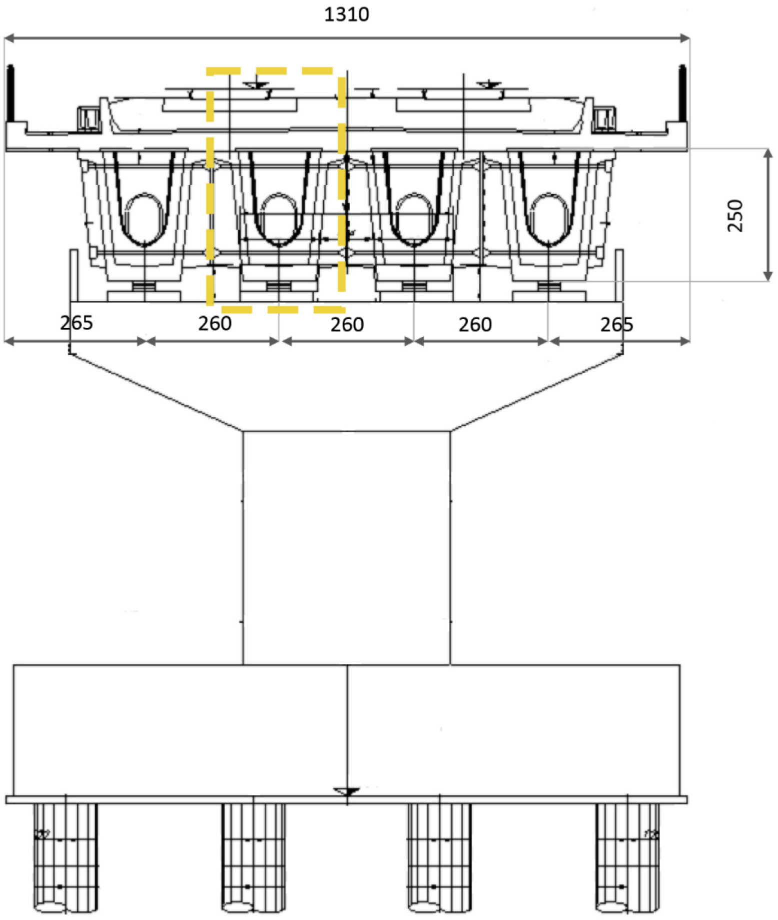

Fig. 3.15 Pile elevation and a cross-section of a bridge displaying the chosen beam (cm)

In the computations, a vertical traveling force of 294.2 kN has been used. It corresponds to the weight of a high-speed train bogie, giving the test a realistic force value. A succession of traveling forces can be readily added to the method (train carriage).

3.3.1 Methodology

A finite-element model (FEM), with the beam discretized using NE=27 beam elements (see 3.16), has been utilized to examine the damage scenarios. The structural problem has been addressed using a displacement approach based on an exact two-node beam stiffness matrix that matches the two-node Euler-Bernoulli beam finite element. As nodal forces are taken into account, the solution in terms of nodal displacements is correct; the deflection curve is well defined because element length is 1/27th of total beam length. Twenty-seven elements have been chosen to consider damage extending over a distance of approximately 1 m. Such extension turns out to be realistic, as shown in Figure 3.1. The chosen reference quantities have been the midspan deflection and rotations at both supports. To assess structural conditions, values of bending stiffness of damaged elements considered unknowns have been determined using measured and model-computed quantities.

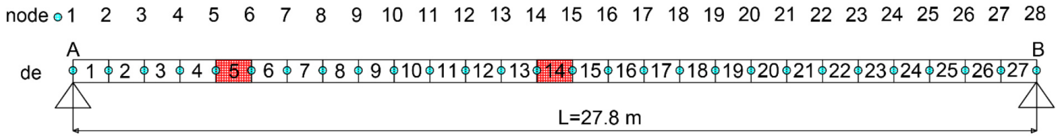

Fig. 3.16 Simply supported beam discretized by 27 elements. Red = generic couple of damaged elements

The "measured" parameters (mid-span deflection and end rotation), which should be derived from in-situ measurements in reality, have been generated from the FEM model associated with the imposed damage scenario; they are input data. The FEM model, which utilizes the trial bending-stiffness values from the genetic algorithm, have provided the model-computed quantities (midspan deflection and end rotation). Therefore, the unknown quantities can be found by seeking for values that minimize the difference between the measured and computed quantities. Figure 5.3 shows a flowchart that highlights the structural assumptions and the essential steps of the suggested methodology.

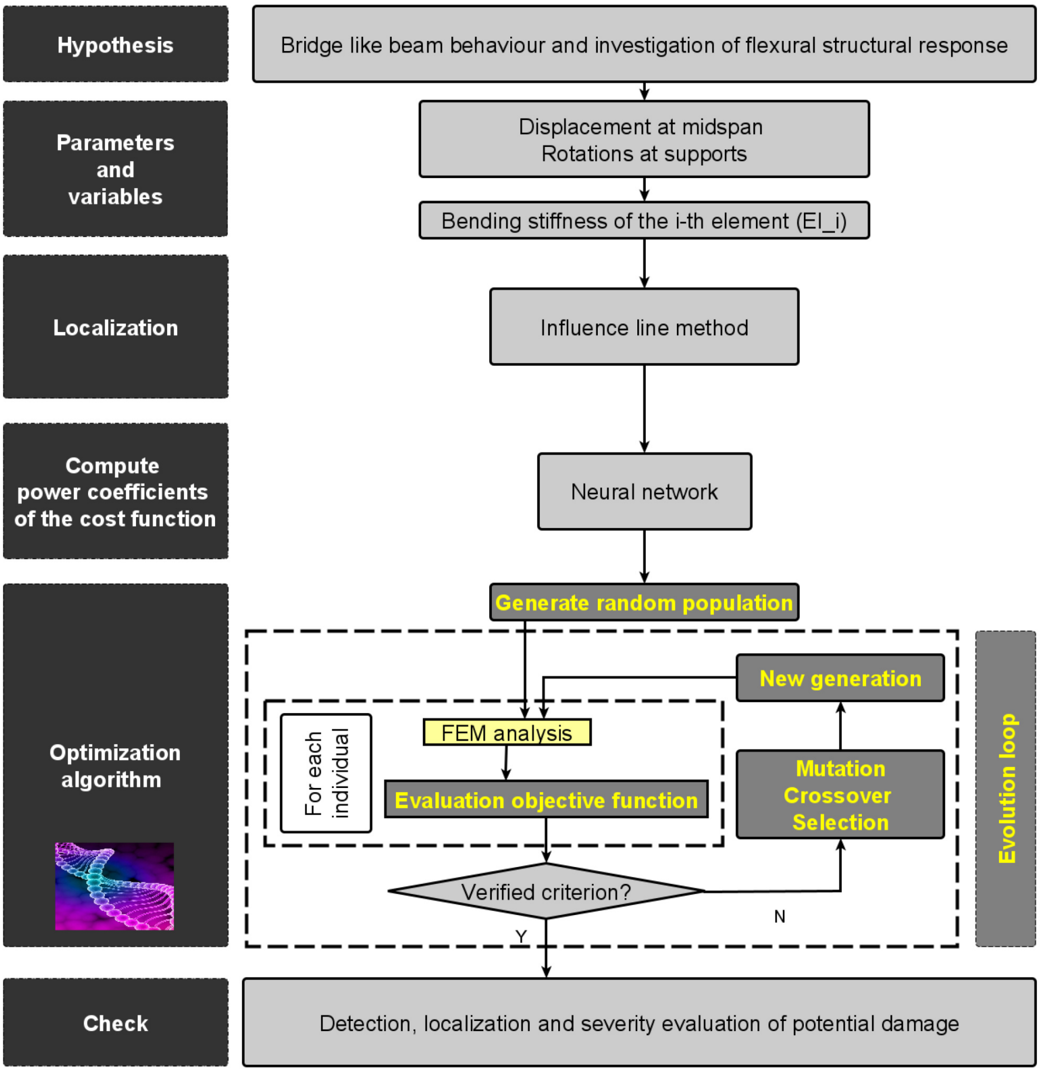

Fig. 3.17 Damage assessment process flowchart

Damage localization: influence line method

Influence lines provide the value of entities (e.g., shear force, bending moment, support reaction, displacement, and rotation) for all positions of a traveling unit load at a certain position in a structure. Damage in beams can be monitored and localized by means of them [201–203]. For instance, one considers the displacement influence lines at the midspan of the damaged ($\eta_m(x)$) and undamaged ($\overline{\eta}_m(x)$) structures, i.e. the midpoint displacement in the two structures when a traveling unit transverse force acts at section x. As a result, at section ($x = xd$) where damage is present

, the difference $\delta_m^{\eta}(x) = abs(\eta_m(x) - \overline{\eta}_m(x))$ will be greater. Likewise, rotation or curvature influence lines can be exploited [202]. One considers a 10 m long, simply supported beam with intact bending rigidity $EI = 1Nm^2$, as an illustration. One assume the beam divided into 20 elements, each of which is 0.5 m long, and that damage is occurring in the fifth element from the left, resulting in a 10% drop in bending rigidity, $EI_d = 0.9Nm^2$. For both undamaged and damaged conditions, influence lines can be estimated using a traveling unit transverse force.

Figures 3.18 a and b depict, from left to right, the influence line for the damaged structure, for the integer one, and the difference between them as functions of the abscissa (load position), for the midspan displacement and left support rotation, respectively. The figure shows the highest values of the $\delta_m^{\eta}(x)$ and $\delta_A^{\varphi}(x)$ (highlighted with red diamond) in the area of the damaged element.

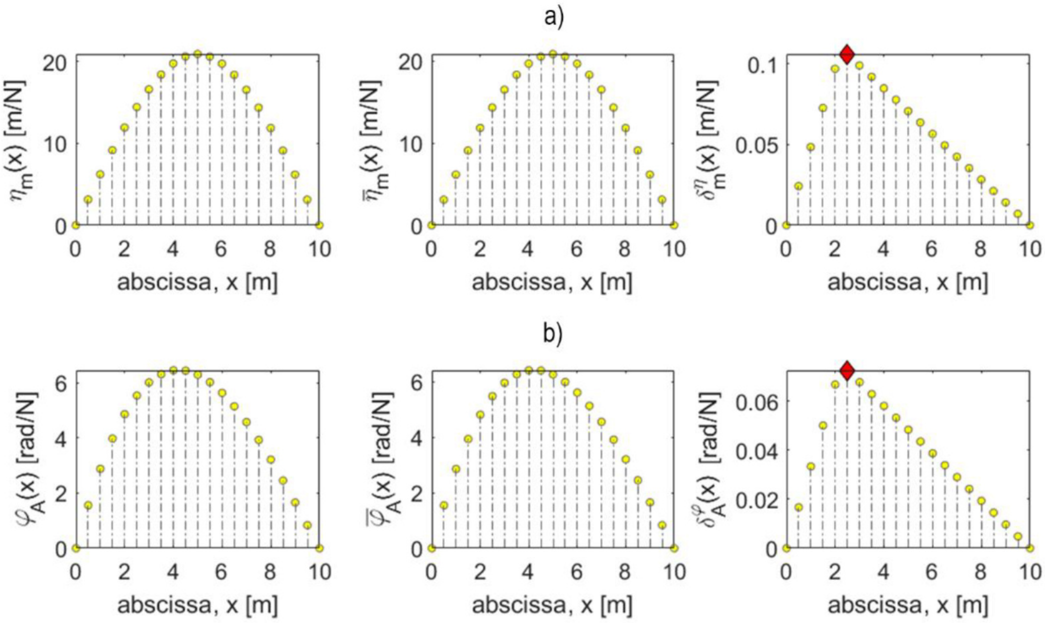

Fig. 3.18 Example of the influence line approach for identifying damage: (a) midspan deflection; and (b) left support rotation

Estimation of damage severity with genetic algorithm supported by a neural network

The genetic algorithm (*GA*), a Darwinian-based optimization method introduced in the Section 1.4.1, has been exploited for the damage severity estimation.

In this research, individuals have been defined by the bending stiffness of the elements identified as being damaged by the influence lines. Once the position and number of damaged elements are determined, the genetic algorithm computes the bending stiffness of the damaged elements by means of the static measurements. Roulette wheel selection and uniform crossover have been the chosen operators (qualitative parameters) in this investigation. The qualitative parameters have been established in the manner outlined subsequently.

The cost function of the *GA* is driven by static parameters (midspan displacement and support rotations). The use of only three measured static parameters in the cost function formulation reduces the need to acquire huge amounts of data. This is one of the particular characteristics of the proposed methodology. Five components make up the cost function:

$$Cost = Cost_{Disp_{pol}}^{\rho} + Cost_{f}^{\varphi} + Cost_{RotA}^{\alpha 1} + Cost_{RotB}^{\alpha 2} + Cost_{RatioRot}^{\delta} \tag{3.11}$$

The power coefficients ρ, φ, $\alpha 1$, $\alpha 2$, and δ have been used to weight the individual contributions, which can be more or less sensitive to the position of the damage. Their impact will be evaluated afterwards. They have been fixed for preliminary analysis and then calculated at a later stage to increase the quality of the results.The formulas for each of the five addends of the Equation 3.11 are given following.

$$Cost_{Disp_{pol}}^{\rho} = \left((NE-2) \frac{\sum abs(Disp_a - Disp_m)}{\sum absDisp_m} \right)^{\rho} \tag{3.12}$$

$$Cost_{f}^{\varphi} = \left(abs \left(\frac{f_m - f_a}{f_m} \right) \right)^{\varphi} \tag{3.13}$$

$$Cost_{RotA}^{\alpha 1} = \left(abs \left(\frac{RotA_m - RotA_a}{RotA_m} \right) \right)^{\alpha 1} \tag{3.14}$$

$$Cost_{RotB}^{\alpha 2} = \left(abs \left(\frac{RotB_m - RotB_a}{RotB_m} \right) \right)^{\alpha 2} \tag{3.15}$$

$$Cost_{RatioRot}^{\delta} = \left(abs \left(Ratio_{m - Ratio_a} \right) \right)^{\delta} \tag{3.16}$$

The formulas used for $Ratio_m$ and $Ratio_a$ are shown in Equation 3.17 and 3.18, respectively:

$$Ratio_m = \left(abs \left(\frac{RatioA_m}{RatioB_m} \right) \right) \tag{3.17}$$

$$Ratio_m = \left(abs \left(\frac{RatioA_a}{RatioB_a} \right) \right) \tag{3.18}$$

The terms $Cost_f^{\varphi}$, $Cost_{RotA}^{\alpha 1}$,and $Cost_{RotB}^{\alpha 2}$ refer to the measured parameters (displacement at midspan and the rotations at Supports A and B). The first term, $Cost_{Disp_{pol}}^{\rho}$, is derived from the displacements of the other structural nodes, which are calculated using the Vurpillot method using the measured quantities; the differences between computed and measured quantities are normalized to the average measured displacement. The final term, $Cost_{RatioRot}^{\delta}$, is dependent on the rotation ratio measured at the supports. Measured and analytical (computed) quantities are indicated by the subscripts m and a, respectively. As suggested previously, the measured values have been numerically generated by means of a FEM analysis, with the damaged elements having reduced bending stiffness; in real-world scenarios, they should derive from on-site measurements. The analytical quantities, on the other hand, have been calculated with a FEM analysis in which the values of bending stiffness of the damaged elements have been extracted from the GA individuals. At the start, the power coefficients for each part of the cost function were fixed to 1. The use of few sensors/measure points (due to the cost function's shape and information given by influence lines), the use of parameters such as end rotations, which is frequently overlooked, the lack of the need to save large amounts of data, and the reducing of computational time are all positive aspects of the proposed cost function.

As [204] highlighted, each quantitative hyperparameter employed in the genetic algorithm has a distinct influence and a significant effect on the success of the algorithm. As a result, it is not advisable to chose them unwisely. Along with the aforementioned parameters (*npop*, *CR*, *MR*), there are three more (β, γ, σ) that are dependent on the selected operators and require attention. The first, β, permits the roulette wheel approach to pick the parents by assigning probabilities (*probs*) to individuals in the population (see Equation 3.19). This method is implemented by creating a probability distribution over the population so that the population's better individuals have a larger chance of being chosen as parents. In the aforementioned equation, c is the cost of the individual normalized with respect to the average cost of the population. The second hyperparameter, γ, is related to the uniform crossover operator. It increases the exploration capabilities of the *GA*.

$$probs = e^{-\beta c} \tag{3.19}$$

Two offspring, $y_j(j = 1,2)$ with n genes (see Equation 3.21) are built starting from two parents $x_j(j = 1,2)$ with n genes (see Equation 3.20). The *i*th gene of the *j*th offspring (see Equation 3.22) is linked to the ith gene of the corresponding parent (x_{ji}) and to the *i*th gene of the other ($x_{\bar{j}i}$) by means of the parameter α_i. The γ parameter is used to extend the classical dispersion range of α_i from [0, 1] to [$-\gamma$, 1+γ]. In this way, it is possible to create offspring somehow different from parents

$$x_j = (x_{j1}, x_{j2}, ..., x_{jn}) \tag{3.20}$$

$$y_j = (y_{j1}, y_{j2}, ..., y_{jn}) \tag{3.21}$$

$$y_{ji} = \alpha_i x_{ji} + (1 - \alpha_i) x_{\bar{j}i} \tag{3.22}$$

The third hyperparameter, σ, is related to the mutation operator, which adds a random number with zero mean and variance σ^2. A search has been carried out on a subset of the space of hyperparameters given in Table 3.12, which specifies the range values and step used for each of them in the context of a grid search method ([205–207].

Table 3.12 Grid search for hyperparameter optimization

Parameter	**Range**	**Step**
npop	[10–50]	20
CR	[0.5–1]	0.15
MR	[0.01–0.1]	0.02
β	[0.8–2]	0.2
γ	[0.1–0.5]	0.1
σ	[0.1–40]	10

Neural Network: Supervised Learning for Selection of Cost Function Power Coefficients

A neural network, a supervised learning model that is currently successfully employed in several scientific fields [208], has been used to enhance the accuracy of the genetic algorithm results of the genetic algorithm. Once the damaged elements have been identified, it has been trained to find optimal power coefficients for the cost function. The damage scenarios, which have been characterized by some damaged elements, have been linked to the power coefficients using numerical simulations. Several damage cases have been explored, and numerical evaluations including 10,000 combinations of power coefficients have been run for each of them. For each power coefficient, the minimum and maximum values of the explored variability range have been set to 0.1 and 1, respectively, with the step set to 0.1. An exception has been made in the case of ρ. This coefficient has been fixed because the associated term in the cost function is related to computed parameters rather than measured ones. Among the 10,000 combinations of power coefficients, the one corresponding to the least error has been picked for each damage scenario. The error has been calculated as the absolute value of the difference between the genetic algorithm's solution and the variables' proper values. Additional linkages between other cases of damage and power coefficients have been created by means of a simplified method due to the considerable computational and time effort needed [209–211, 207, 212]. For damage cases similar to to the ones already studied, where "similar" denotes that the damage locations are close to those just analyzed, the power coefficients previously computed with the addition of noise have been utilized. The noise varies between 0.5 and 1.5 percent depending on the proximity to the previously examined case. The 171 connections have been used to train and test a neural network. Figure 3.19 shows the neural network architecture. For each example provided to the neural network, there are seven inputs. The first five are set aside for reporting damaged elements, labelled 1 to 27. If *nd* (namely the number of damaged elements) is less than 5, the remaining 5–*nd* inputs are set to zero. The positions of the most affected elements are included in the last two inputs. The four power coefficients, on the other hand, constitute the targets.

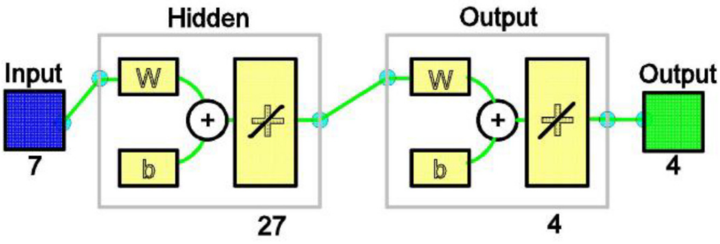

Fig. 3.19 Architecture of neural networks

The samples have been divided into three groups: training (70%), validation (15%), and testing (15%). A two-layer feedforward network, with a sigmoid transfer function in the hidden layer and a linear transfer function in the output layer, has been employed. The training algorithm employed Bayesian regularization and the number of hidden neurons has been tuned to 27. Performance has been measured using regression (R) and mean squared error (MSE). The correlation between outputs and targets is evaluated using regression. The correlation between outputs and targets is evaluated using regression. R values near 1 imply a strong relationship, whereas R values near 0 indicate a random one. The MSE is the average squared difference between the outputs and the target. Low values of this index mean good results.

3.3.2 Results

Under the above-mentioned traveling force, the influence lines of midspan deflection and support rotations have been numerically calculated for the undamaged and damaged structures for the analyzed problem. This have allowed the damaged elements in the discretized structure to be localized, giving information for the genetic algorithm. Three structural damage scenarios with two damaged elements are depicted in Figure 3.20. The structural schemes are shown in the upper section of the figure. The most significantly damaged element is shown in red, along with the corresponding flexural stiffness. The color blue is used to represent the element with less severe damage. The case on the right, for example, includes two damaged elements, one with a 0.9EI for element n. 7 (*de = 7*) and the other with a 0.75EI for element n. 16 (*de = 16*). The peaks (diamonds) corresponding to the damaged elements may be observed in the squares of relative differences $\delta_m^{\eta,rel}$, $\delta_A^{\varphi,rel}$, $\delta_B^{\varphi,rel}$for the midspan displacement and for the left (A) and right (B) support rotations (e.g., $\delta_m^{\eta,rel} = abs\left(\frac{(\eta_m(x)-\overline{\eta}_m(x)}{\overline{\eta}_m(x)}\right)$. The use of these three indices also allows for the localisation of damage in areas where it is typically difficult to do so, such as those near the supports (see the second case in Figure 3.20).

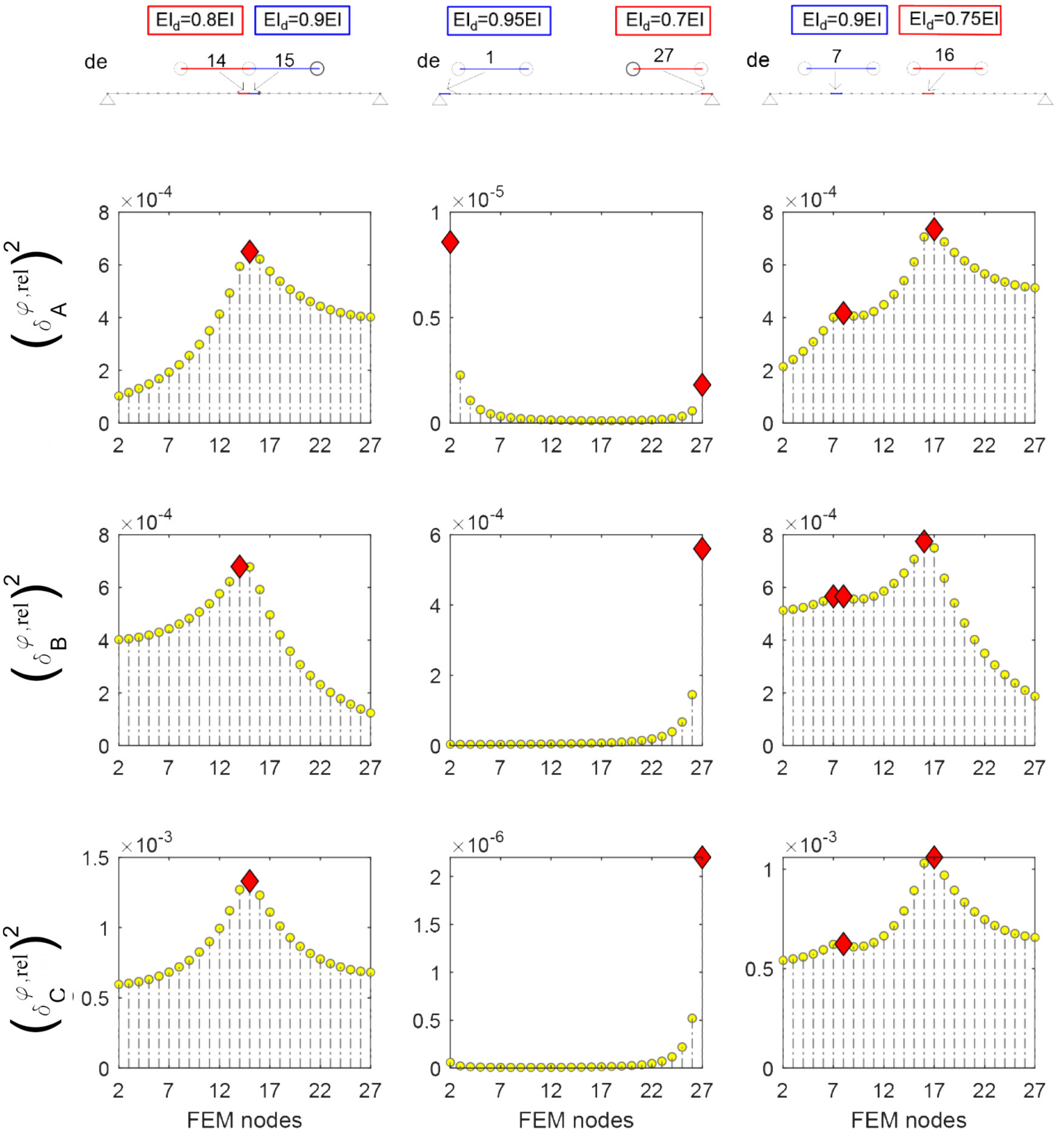

Fig. 3.20 Three damage scenarios identified by influence line methodology

It is worth mentioning that the bridge under study has a high bending stiffness. This leads in relatively small differences in the values of displacement and rotation between the undamaged and damaged states when the traveling force is applied. For micrometer measurements, nevertheless, high-sensitivity displacement transducers such as LVDT sensors, as well as current approaches such as digital image correlation (DIC) [213], are possible. Other damage-sensitive mechanical parameters, such as strains, can also be employed; such technique is still accurate, and the procedure provided above is still applicable in theory. The findings of damage localization using influence lines are useful for estimating damage severity later on. Implementing these two procedures at the same time would be quite computationally expensive, particularly for complex problems. In these scenarios, the number of design variables is high, and the accuracy of the solution worsens. Influence lines can not only eliminate elements with a low likelihood of damage from further study, as is the case of gray relation analysis [81], but they can also significantly reduce the number of design variables by detecting damaged elements. The use of influence lines on a non-complex beam structure is a streamlining that has allowed the process to be tested for the first time. Influence surfaces should be utilized on a two-dimensional (2D) structural model to better characterize the bridge structural response [202]. A preliminary study has been carried out to tune the GA's numerical parameters, as previously mentioned. The aim has been to determine the combination of hyperparameters that delivers adequate results for future investigations, rather than the optimum combination of hyperparameters. As a result, performance in terms of cost has been compared for each structural problem (case of damage considered for the parameters tuning operation) and each combination of parameters, neglecting the stochastic aspect of the problem. Using the range values and steps in table 3.12, a total of 8,400 parameter combinations have been created. For each of the four studied damage cases (DCs), the behavior of the cost function with regard to parameter combinations has been examined. For the sake of simplicity, only one damaged element is present in each of these cases. As a result, the GA's number of variables has been fixed to one. Table 3.13 shows the number *de* (between 1 and 27 starting from the Left support A) that identifies the damaged element, as well as the related bending stiffness, EI_d, given as a proportion of the undamaged bending stiffness EI, for each of the four damage scenarios studied.

Table 3.13 Damage scenarios for tuning GA numerical parameters

DC parameters	**DC_1**	**DC_2**	**DC_3**	**DC_4**
de	14	14	2	2
Ei_d	0.5 EI	0.8 EI	0.5 EI	0.8 EI

The cost, as a function of parameter combinations and damage scenarios DC1 to DC4, is depicted in Figure 3.21. It is extremely dependent on the parameters, particularly for DC1. As a result, with DC1 as the worst scenario, Combination 558 has been chosen as the parameter combination with the lowest cost; view Table 3.14.

Table 3.14 Combination 558

npop	***CR***	***MR***	β	γ	σ
50	0.8	0.003	1.4	0.2	0.1

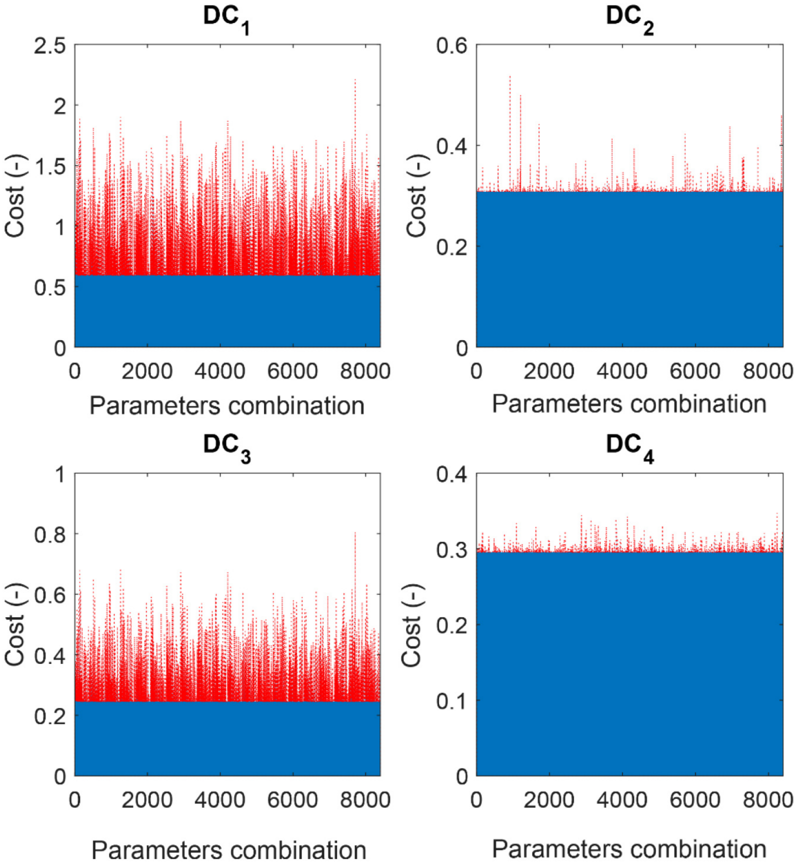

Fig. 3.21 Cost based on parameter combinations and damage scenarios

For the examined damage scenarios, the outcomes in terms of cost, accuracy, and error are shown in Table 3.15. The ratio between the estimated solution and the correct one has been used to calculate accuracy. The error has been computed using the equation 3.23:

$$Error = \frac{GA_{value} - Correct_{value}}{Correct_{value}} \tag{3.23}$$

Table 3.15 Combination 558 cost and accuracy

Results	**DC$_1$**	**DC$_2$**	**DC$_3$**	**DC$_4$**
Cost	0.6	0.30	0.24	0.29
Accuracy	1	0.9	1	1
Error	0	-0.1	0	0

Although the findings are acceptable, they are still subject of improvement. Starting from information of the damage location, the effects of the power coefficients (φ, $\alpha 1$, $\alpha 2$, δ) of the cost function, which had previously been considered unitary, have been examined. After finding the benefits of varying these coefficients in the simplest damage situation (one element), it has been decided to fully leverage the damage location information to improve results in even the most complicated damage scenarios. A regression R of about 0.92 for the training set and about 0.88 for the test set has been produced by utilizing the neural network, as previously mentioned. They may be deemed satisfactory, though an increase of the number of sample cases used to train the network will undoubtedly enhance them. Figure 3.22 depicts the MSE value for the training and test sets versus epoch variation. The training set at Epoch 1,000 achieves the best MSE value, which is rather minimal. In addition, the test set's MSE index is trending downward, indicating that the training data is not overfit. Without overfitting, an increase in the number of epochs can improve the network's performance even further [214]. The error histogram is another approach for determining the network's quality, as shown in Figure 3.22. The error has a Gaussian distribution with a mean close to zero and a small dispersion, as can be observed.

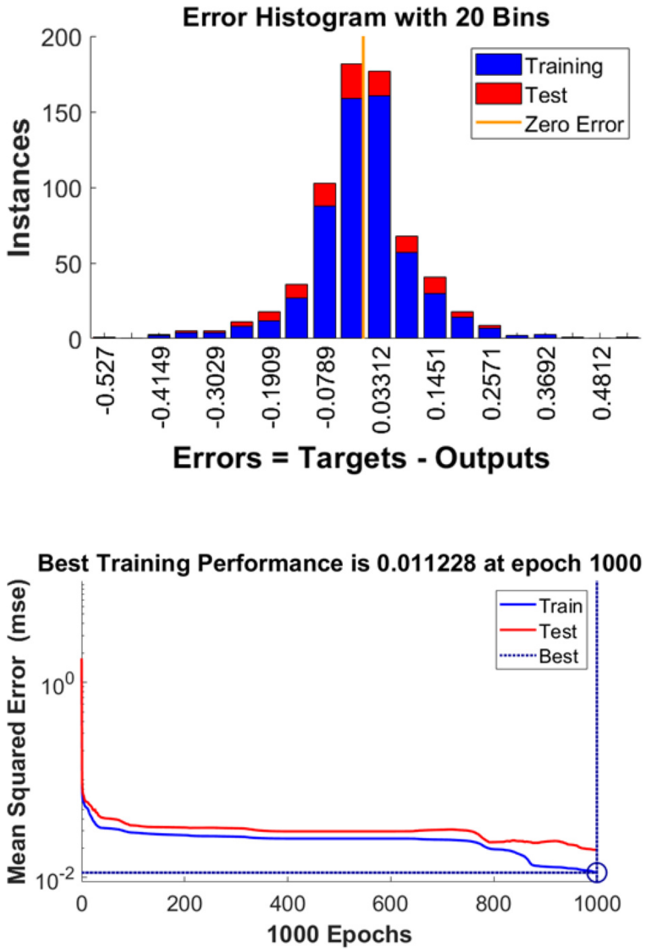

Fig. 3.22 Error histogram and performance of neural network

Validation tests have been carried out to ensure that the neural network has been capable of generating power coefficients that could be used to determine damage severity reliably. Starting with new damage scenarios and assuming that the damage location is known via the influence line approach, the neural network (*NN*) has been utilized to generate the power coefficients that would be employed in the genetic algorithm to estimate the bending stiffness of the damaged elements. Table 3.16 shows the results of one of the new damage cases that has been tested. The error in estimating the bending stiffness is computes by Equation 3.23.

Table 3.16 Example of new case with two damaged elements

de	**EI**$_d$	φ	$\alpha 1$	$\alpha 2$	$\delta 2$	**Error**
10,27	0.8 EI 0.95 EI	0.75	1.07	0.36	0.52	1.3 10^{-3} 1.8 10^{-2}

Figure 3.23 shows the error distribution. With a mean of -0.011 and a standard deviation of 0.06, the normal distribution demonstrates that almost 70% of the damage cases has an error less than 6%. The logistic distribution can also be used to fit the data. It seems to fit the data even better with a mean of -0.0026 and a standard deviation of 0.025. The damage examples sketched in Figure 3.23 are the ones with the most significant errors. In overall, the results are satisfactory, but they can still be improved by training the *NN* with more cases to eliminate the probability distribution's tails. The same damage cases have been utilized to demonstrate the actual improvement in outcomes that may be gained by applying power coefficients extracted from the neural network, as stated so far. A normal error distribution with a mean of -0.015 and a standard deviation of 0.48 has been produced using unitary coefficients, which is a less accurate solution than the one above. As a result, the strategy is worthwhile.

As the geometric properties of the beam have been altered, the same damage scenarios have been employed to test the methodology's effectiveness. The error distribution is essentially identical when a beam length of 50 m is considered. Furthermore, the distributions shift very slightly when the value of the moment of inertia I is changed. The results have been explored for moment of inertia values of 2 and 1.5 m^4. In these circumstances, the normal distribution's mean is around -0.01 and the standard deviation is around 0.08. These findings are encouraging in terms of the applicability of the methodology as the geometric parameters of the beam change. Finally, it is also worth noting that the methodology is computationally sustainable. For each analysis involving the genetic algorithm, the needed computational time is around 2.5 seconds.

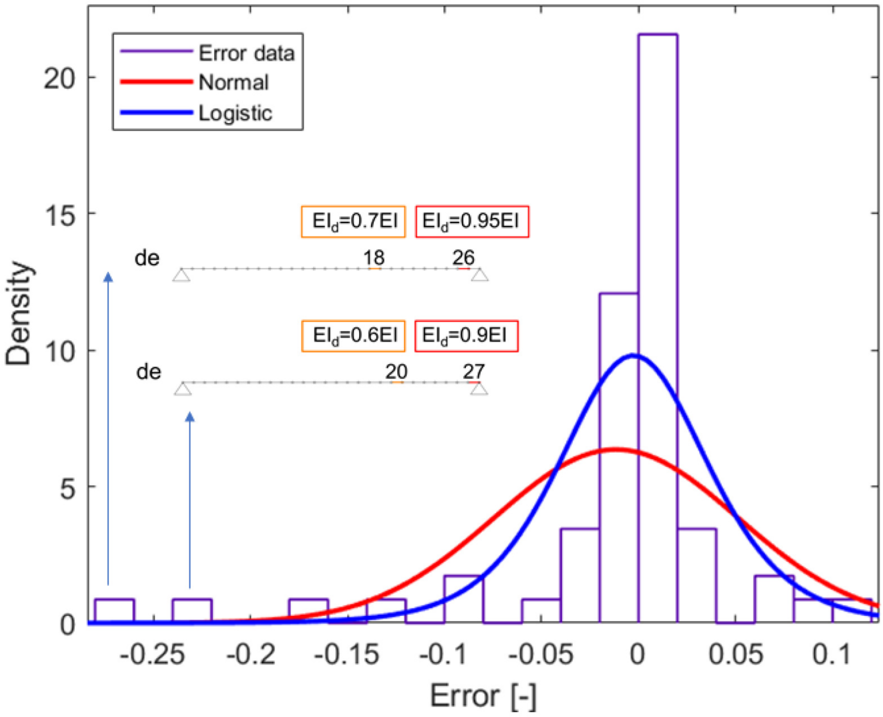

Fig. 3.23 Distribution of errors

3.4 In Closing

The first methodology discussed in this chapter (Section 3.2) investigates the static and environmental data collected on a prestressed railway bridge during its first few years of service. Correlation models have been developed following evaluations of cause-effect relationships between the measured quantities in the healthy condition. The modelling assumptions underlying such correlations are founded on physical phenomena. These are represented by relationships that relate input parameters (causes) to output parameters (effects), which can be described by complex models due to the structural complexity and the multiplicity of phenomena to which it is exposed. Two aspects have been explored and controlled in depth. The first one, the assessment of the midspan strain of the unloaded deck, has been faced taking into account the influence of several factors. Among these are temperature, its difference (gradient) measured over many distances, and other environmental elements (for example, solar radiation). The second task, the assessment of pier rotations and joint expansion, has been performed by considering the impact of environmental variables on these phenomena. The correlations defining the undamaged structural condition has been effectively modelled, resulting in extremely precise predictions of the signal chosen as output of the model. The addition of a pre-processing operation involving z-score normalization on a sliding window has been demonstrated to be a tool capable of mitigating the effects of both structural and non-structural delayed phenomena. This is necessary in order to get data that are repetitive. The absence of such operation would have implied an ineffective training of the model with a consequent inaccuracy. In fact, a model that learns different relationships between input and output cannot be an accurate or robust model. Furthermore, this has allowed for the development of successful correlation models and the determination of the healthy structural condition. The use of additional temporal parameters, on the other hand, has proved very effective in overcoming the lack of some environmental parameters, such as solar radiation. The findings of the signal analysis and reconstruction approach have resulted in the establishment of undamaged-condition alarm thresholds (UCT) and successful fault detection, which has outperformed the results of traditional thresholds (DT) based on design values. The minimization of false alerts has been given particular consideration. The moving median of the residual between the predicted and measured signals has been used as a damage index to reduce their number. In detail, the moving median of the residuals with respect to the seven preceding days has implied that an anomaly is reported only if at least more than 50% of the signals in the previous week have an error falling outside the threshold. The selection of features composing the correlation models, the use of pre-processing operations to give data repetitiveness over time, the exploitation of some temporal parameters to compensate for the lack of some environmental ones, the selection and the training of specific regression model, and the proposed damage index have all been found to be very successful in the framework of long-term monitoring.

The second methodology presented in this Chapter considered the idea of a hybrid technique based on static measurements that could aid a genetic algorithm in identifying and quantifying structural damage with a reduced number of variables. The proposed hybrid technique for inverse damage identification (detection, localization, and estimation) has been successful and encouraging. The main new features and highlights can be briefly listed as follows:

- The use of influence lines with the three associated indices – namely, the square of relative differences between undamaged and damaged stages for the mid-span displacement, $\left(\delta_m^{\eta,rel}\right)^2$, for the left (A) and right (B) support rotations, $\left(\delta_A^{\varphi,rel}\right)^2$ $\left(\delta_B^{\varphi,rel}\right)^2$, makes it possible to identify damaged regions (beam elements), either along the span or near the supports. Using the rotations at the supports as control parameters certainly helps in this regard;

- By overcoming the exclusion of unlikely damage locations (e.g., gray relation analysis), the application of influence lines drastically decreases the design variables of the genetic algorithm. As a result, the computation time is reduced. This is a conceptual prerequisite for the development of this methodology for use in practical applications;

- The use of a cost function defined as the sum of five addends, each of which is more or less influenced by the damage depending on its location, allows a specific weight to be connected with each addend using power coefficients, hence improving the solution accuracy . The findings reveal that the three measure points/sensors produce extremely accurate predictions in the investigated case. The mid span displacement and the two end rotations are the only values needed to calculate displacements at each node in the cost function;

- The power coefficient of the cost function can be successfully set using the trained neural network. Its architecture is also capable of dealing with scenarios involving more than two damaged elements;

- Damage scenarios characterized by localized bending stiffness reductions have been successfully evaluated on a simply supported beam. Using different beam lengths and geometric features, the same damage scenarios have been applied to test the validity of the methodology. Without modifying the coefficients in the algorithm, good outcomes have been achieved;

In summary, the achieved gains are in terms of computational speed, critical element location utilizing few measure points, and adaptability. The findings for the studied case make this technique appealing and deserving of future investigation. Even though more study is needed before moving further with real-world applications, the proposed technique is generalizable. Areas of improvement involve the use of more refined structural models (grillage), the use of influence surfaces for damage localization, other damage indicators, and damage scenario investigations.

The two presented techniques have been designed to complement each other for the development of a holistic control plan for simply supported concrete railway bridges.

Chapter 4

Transfer learning for structural health monitoring of urban pedestrian bridges

4.1 Problem definition

Pedestrian bridges in high-densities city are bridge structures that are structural similiar and replicated extensively. In Lisbon, for example, there are 60 of these bridges strewn across the city. The problem of managing a large number of bridges of the same type is similar to that shown in the previous Chapter of this thesis. However, in the current Chapter, the aim of optimising resources for the development of control plans to ensure the infrastructure safety has been achieved by a different method. This is Transfer Learning, a method that has recently gained relevance in *SHM*. The application of transfer learning and domain adaptation methods to monitor pedestrian bridges has not yet been applied. In this Chapter, to further understand the potential and limitations of domain adaptation, the performance of the transfer learning approach has been demonstrated first in a numerical simple supported beam model. Then, an extension has been made to two real pedestrian bridges located close the campus of the Lusòfona University. As will be shown in the following sections, a further methodology defined as "direct standardization" has been used to assess classification performance and a comparison with the results extracted from the application of TCA has performed.

4.2 Methodology

4.2.1 Transfer Component Analysis

The domain adaption strategy used in this investigation was the one proposed by [215]. TCA is a transformation and dimension reduction space of features into a reproducing kernel Hilbert space (RKHS), which is analogous to principal component analysis [216]. This mapping is driven by the distance between probability density distributions (PDF) of these features or other metrics, as well as an unknown nonlinear function $\phi(\cdot)$ that must be discovered. The basic idea is to use a domain transformation technique to minimize the distance between these features while keeping the main properties [217]. Kernel Mean Matching [218], Kullback-Leibler Divergence [219], and the Maximum Mean Discrepancy ($\mathscr{M}$) are three well-known methods for computing distances between feature distributions. This last method has been chosen in this study since it is the simplest and most basic one to execute this minimization. The squared average element of source and target domains into the RKHS computed by [220]is the distance metric ($\mathscr{M}$) used here.

$$\mathscr{M}\left(\mathscr{X}_s, \mathscr{X}_t\right) = \left\| \frac{1}{n_s} \sum_{i=1}^{n_s} \phi(x_{s_i}) - \frac{1}{n_t} \sum_{j=1}^{n_t} \phi(x_{t_j}) \right\|_{\mathscr{H}}^2 \tag{4.1}$$

where the subscripts s and t is the source and target domains, respectively, $\mathscr{X} = [x_1 \cdots x_n]^T$ is the feature matrix, where n is the number of vectors in the source $\mathscr{D}_{\mathscr{S}}$ and target $\mathscr{T}_{\mathscr{S}}$ domains in the Hilbert space $\mathscr{H}$, and $\phi(.)$ is the nonlinear mapping function to be determined. However, because it necessitates complex mapping functions, minimizing equation (4.1) directly utilizing unlabeled features in the target domain is difficult. A correlation matrix (or Gram matrix) can be used to perform this technique as a simple measure of similarity between feature observations in the source and destination domains, i.e., how comparable such features are based on their distance. In a practical sense, the Gram matrix can be calculated using the kernel approach, which reduces dimensionality by adopting an inner product structure [221]. In this study, a linear kernel $\mathscr{K}$ was used.

Equation (4.1) can be rewritten as:

$$\mathscr{M}\left(\mathscr{X}_s, \mathscr{X}_t\right) = \operatorname{tr}(\mathscr{K}L) \tag{4.2}$$

where $\operatorname{tr}(\cdot)$ is the trace operator, and $L \in \mathbb{R}^{(n_s+n_t)\times(n_s+n_t)}$ is described as:

$$L_{ij} = \begin{cases} \frac{1}{n_s^2}, & x_i, x_j \in \mathscr{X}_s \\ \frac{1}{n_t^2}, & x_i, x_j \in \mathscr{X}_t \\ -\frac{1}{n_s n_t}, & \text{otherwise.} \end{cases} \tag{4.3}$$

To easily achieve the minimization of equation (4.2), the Gram matrix can be decomposed in this form:

$$\mathscr{K} = \left(\mathscr{K}\mathscr{K}^{\frac{1}{2}}\right)\left(\mathscr{K}\mathscr{K}^{\frac{1}{2}}\right)$$

and replaced by an empirical kernel $\tilde{\mathscr{K}}$

$$\tilde{\mathscr{K}} = \mathscr{K}\mathscr{W}\mathscr{W}^T\mathscr{K} \tag{4.4}$$

where $\mathscr{W} \in \mathbb{R}^{(n_s+n_t)\times m}$ is a transformation matrix such that reduces the dimensions m, i.e. $m << n_s + n_t$, and also maps the features into the RKHS.

As a result, using this empirical kernel, the MMD can be rewritten as follows:

$$\mathscr{M}(\mathscr{X}_s, \mathscr{X}_t) = \operatorname{tr}\left(\tilde{\mathscr{K}}L\right) \equiv \operatorname{tr}\left(\mathscr{W}^T\mathscr{K}L\mathscr{K}\mathscr{W}\right) \tag{4.5}$$

In order to retain the properties of the features after transferring, it is also necessary to ensure that the data variance is conserved. The following is the data variance:

$$\mathscr{W}^T\mathscr{K}\mathscr{H}\mathscr{K}\mathscr{W}, \quad \text{where} \quad \mathscr{H} = \mathbb{I} - \left(\frac{1}{n_s + n_t}\right)\mathscr{I} \tag{4.6}$$

where $\mathscr{H}$ is a centering matrix, $\mathbb{I} \in \mathbb{R}^{(n_s+n_t)\times(n_s+n_t)}$ is the identity matrix and $\mathscr{I} \in \mathbb{R}^{(n_s+n_t)\times(n_s+n_t)}$ is the matrix of one. Consequently, an optimization problem with a constraint can be defined to find the optimal or sub optimal value of

$$\begin{aligned} \min_{\mathscr{W}} \quad & \operatorname{tr}\left(\mathscr{W}^T \mathscr{K} \mathrm{L} \mathscr{K} \mathscr{W}\right) + \mu \operatorname{tr}\left(\mathscr{W}^T \mathscr{W}\right) \\ & \text{subject to} \quad \mathscr{W}^T \mathscr{K} \mathscr{H} \mathscr{K} \mathscr{W} = \mathbb{I}_m \end{aligned} \tag{4.7}$$

where $\mu > 0$ is the trade-off parameter related to the regularization term, and $\mathscr{I}_m \in \mathbb{R}^{m \times m}$ is the identity matrix. The constraint's restriction are intended to maintain the data variance and keep the attributes of the source and target unchanged.

Equation (4.7) can be resolved by various different optimization procedures. Among these approaches, Lagrange multipliers are beneficial to describe this optimization as an equivalent maximization problem given by [222].

$$\max_{\mathscr{W}} \quad \operatorname{tr}\left[\left(\mathscr{W}^T (\mathscr{K} \mathscr{L} \mathscr{K} + \mu \mathbb{I}_m) \mathscr{W}\right)^{-1} \mathscr{W}^T \mathscr{K} \mathscr{H} \mathscr{K} \mathscr{W}\right] \tag{4.8}$$

where the m eigenvectors of $(\mathscr{K} \mathscr{L} \mathscr{K} + \mu \mathbb{I}_m)^{-1} \mathscr{K} \mathscr{H} \mathscr{K}$ are the transformation matrix $\mathscr{W}$ that shifts all attribute data into RKHS by diminishing the distance between distinct domains and preserving the properties.

4.2.2 Statistical modeling for feature classification

In this study, a Gaussian model and a subsequent outlier identification approach have been used to perform the classification. In detail, one of the most frequently applied procedures has been utilized, namely the MSD. It is a distance measure used to find outliers in multivariate statistics [223]. When one considers the training matrix, $\mathscr{X}_s$, with multivariate mean vector, μ, and covariance matrix, Σ, the MSD (or DI in the context of SHM) between feature vectors from $\mathscr{X}_s$ and any new feature vector (or observation) from the test matrix, $\mathscr{X}_t$, is calculated as:

$$\mathrm{DI}(x_t) = (x_t - \mu) \Sigma^{-1} (x_t - \mu)^{\top} \tag{4.9}$$

As a result, multivariate outliers are defined as observations with DIs greater than a given threshold. It is worth remembering that outlier identification requires the assumption of a Chi-square distribution since it allows for the definition of a cut-off value or threshold, c, for a level of significance, α, in the form of $c = invF_{\chi^2_n}(1-\alpha)$, where $F_{\chi^2_d}$ is the cumulative distribution function of the central Chi-square distribution. When the DI of a feature vector is equal to or greater than c, it is deemed a multivariate outlier. The choice of α involved a trade-off between the Type I error (a false-positive) and the Type II error (a false-negative). Typically, a level of significance of 5% is considered adequate.

4.3 Transfer learning between numerical models

Two beams with same static scheme, same section, but differing lengths have been used in a numerical research for the source and target domain. Their cross-section is rectangular, with a height of 0.4 meters and a width of 0.2 meters. The length of the target beam, L_t, is fixed and equal to 5 meters. The length of the source beam L_s is variable and connected to the one of the target beam by means of Equation 4.10.

$$L_t = L_s + (L_s \Delta) \tag{4.10}$$

The parameter Δ, which ranges from 0.2 to -0.2 (in steps of 0.1) in this study, indicates the percentage of length variation between the two beams. For the source and target domains, two populations of frequencies reflecting the healthy structural state have bene produced, each with 1000 and 300 samples. To achieve this, first, Gaussian distributions of 20000 samples for Young's modulus (E), cross-section height (h), and cross-section width (w) have been created. Table 4.1 displays the mean values for such populations. The dispersion (in terms of standard deviation) of these populations has been object of study. Indeed, to account for the effect of parameter dispersion on the results provided by the methodologies listed below, three combinations of standard deviation have been investigated. For each combination, the standard deviation of the parameters (Std_*) has been expressed as the product of a dispersion factor (F_*), defined in Table 4.2, by the mean value (see equations 4.11, 4.12, and 4.13).

Table 4.1 Mean values of Gaussian distributions of the key structural parameters

E [Pa]	**h [m]**	**w [m]**
$35E+9$	0.4	0.2

$$Std_E = F_E \, mean(E) \tag{4.11}$$

$$Std_h = F_h \, mean(h) \tag{4.12}$$

$$Std_w = F_w \, mean(w) \tag{4.13}$$

Table 4.2 Definition of the dispersion factors for comb*i* parameter (i=1, 2, or 3)

Parameter	comb1	comb2	comb3
F_E	0.008	0.02	0.03
F_h	0.005	0.013	0.02
F_w	0.005	0.013	0.02

Second, random choices for E, h, and w were made 1000 times for the source and 300 times for the target, starting from the respective distributions consisted of 20000 values. In this manner, using analytical formulations, a population of frequencies has been created, consisting of 1000 and 300 samples for the source and target domain, respectively.

The first four longitudinal bending frequencies, the first four transverse bending frequencies, and first torsional frequency have been computed analytically for the two domains, with the aim of evaluating the results of the analysis even when the number of frequencies constituting the individual sample/data varies. Nevertheless, as explained in the following section, the results displayed pertain to data with only one frequency of each type. The target domain has been then supplemented with 20 samples related to the damage condition (beam with crack). Three damage scenarios, labelled based on the average crack depth (DS15, DS12, and DS10), have been systematically studied in detail. They entail the creation of a crack (eg., average depth 0.15, 0.12, and 0.10 m, respectively for DS15, DS12, and DS10) in 20 sections between 1 and 1.20 meters from the left support. To get a dispersion of the data for the three damage scenarios, a constant standard deviation of 0.6 cm was employed in conjunction with each of the three mean crack depths.

Considering different values of the Δ parameter, the comb parameter, and the damage severity, Figure 4.1 displays five examples (from *a* to *e*) illustrating target and source domain in the original space. Indeed, for each of the 45 cases listed above, transfer learning between source and target structures has been carried out utilizing direct standardization and TCA (five length differentials, three dispersion scenarios, and three damage scenarios). Although the categorization performance results for all cases will be shown, five of them have been chosen for a more thorough explanation of the outcomes. The choice is intended to address as many diverse scenarios as feasible. The frequency distributions of the source and target structure are shown in a frequency space that includes the first bending modes in the longitudinal and transverse axes as well as the first torsional mode.

This allows for a better understanding of what happens as the parameter Δ, the parameter comb, and the damage severity change. Table 4.3 shows the parameters related to the five cases depicted in the Figure 4.1.

Table 4.3 Parameter definition (Δ, comb, and DS) for meaningful cases

Case	**Δ**	**comb**	**DS**
a	-0.2	1	15
b	0.1	2	12
c	-0.1	3	12
d	0.2	3	10
e	0	2	10

All length differences between the source and target structures are represented by the scenarios chosen. The largest damage will occur in the first scenario, followed by medium damage in the second and third, and smallest damage in the final two. As regards the dispersion, case a small shows a small dispersion, case b and e a medium one, and cases c and d a large one. For the extremely favorable case, no problem in damage recognition is foreseen (small dispersion, large crack scenario a). The damaged data points are still plainly visible when the medium dispersion and a medium crack are present (scenario b), but they are substantially closer to the normal (undamaged) target data. When the undamaged and damaged target data partially overlap, as in scenario c, some false negatives can be observed. The damaged data points are substantially closer to the normal (undamaged) target data and substantially overlap when the medium dispersion is coupled with a small crack (scenario e). Due to the overlap of damaged and undamaged target data, as in scenario e, there are several false negatives occurring.

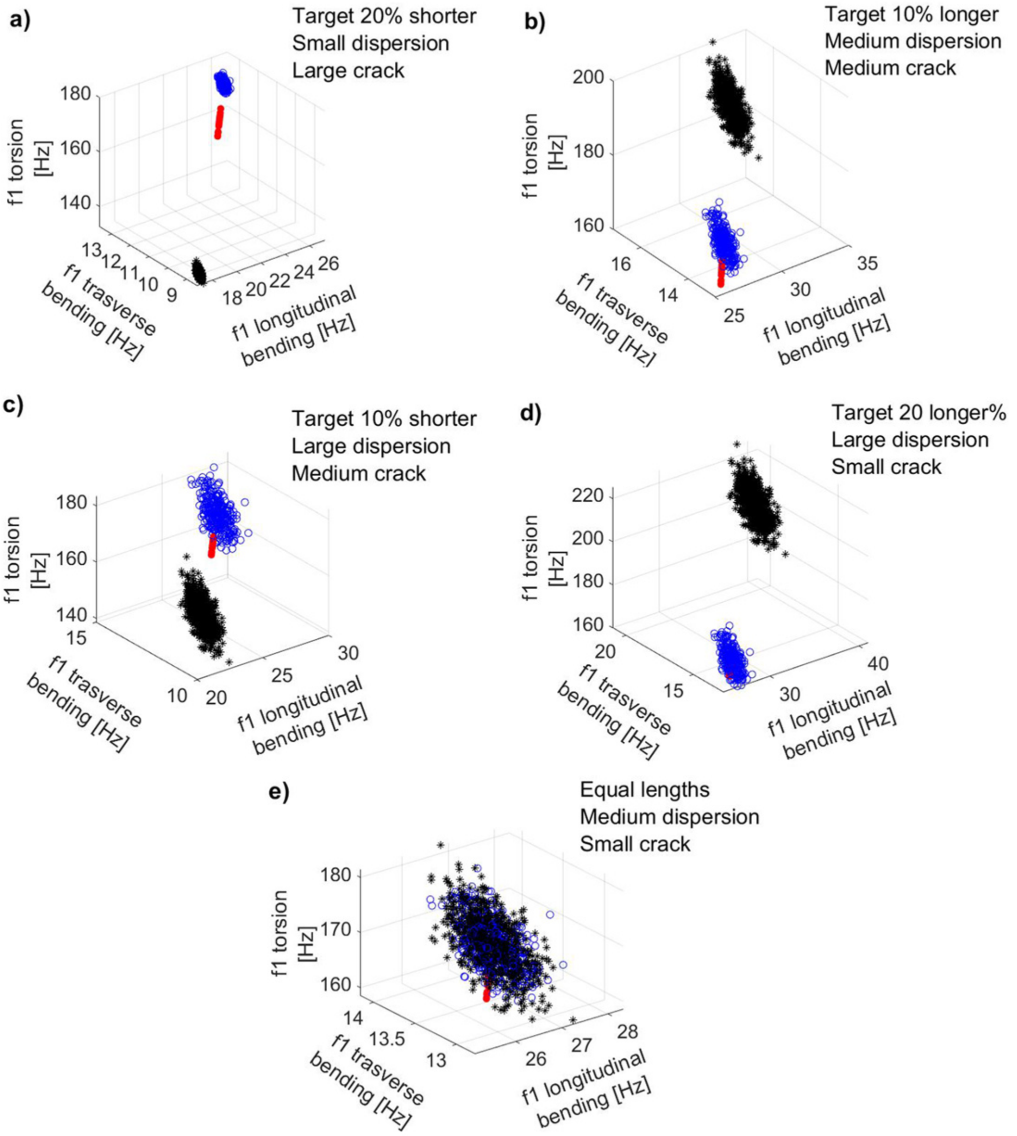

Fig. 4.1 Original space. Black (Healthy source data), Blue (Healthy target data), Red (Damaged target data)

Other observations can also be made from these five examples. As is well known, the length of the beam has an effect on its frequencies. As the length increases, the frequency decreases. In Figure 4.1, due to the increase in length, the target domain shifts away from the source domain in the second and fourth cases, resulting in progressively smaller values of the three frequencies. From the other hand, it's worth noting that increasing dispersion in the undamaged state leads to include the damaged samples, particularly if the damage is small.

4.3.1 Analitycal and numerical solution

Undamaged condition

To calculate the frequencies in the undamaged condition, the following formulations have been adopted.

Equation 4.14 [224] calculates the angular frequency (p) for each bending mode (longitudinal and transverse).

$$p = \sqrt{\frac{b^2 EI}{\rho AL^4}} \tag{4.14}$$

In this equation E is the elasticity modulus, I is the cross-sectional area moment, ρ is the density, A is the cross-sectional area, and L is the beam length. The value b is determined for each mode, after defined the quantities r^2 (Equation 4.15) and s^2 (Equation 4.16), and the value of β (Equation 4.17) is replaced in Equation 4.18.

$$r^2 = \frac{I}{AL^2} \tag{4.15}$$

$$s^2 = \frac{EI}{kAGL^2} \tag{4.16}$$

$$\beta = \frac{((r^2+s^2)+((r^2-s^2)^2+\frac{4}{b^2})^{0.5})^{0.5}}{\sqrt{2}} \tag{4.17}$$

$$\sin b\beta = 0 \tag{4.18}$$

There are two more parameters in Equation 4.16 that have still to be stated. The numerical shape factor for the cross section k is the first. Because a rectangular shape is being evaluated, this value is set to 5/6 in this example. The modulus of rigidity G is the second parameter.

The angular frequency expressed by Equation 4.19 has been employed for the torsional mode.

$$\omega_{nt} = \left(\frac{n\pi}{L}\right)\sqrt{\frac{GJ_s}{J_o\rho}} \tag{4.19}$$

In this Equation J_s is the cross section equivalent moment of inertia owing to torsion, J_o is the polar moment of inertia, n is the mode number, and ρ is the density. Equation 4.20 provides the equivalent moment of inertia of a cross section due to torsion.

$$J_s = 0.2287\,h\,w^3 \tag{4.20}$$

The natural frequencies [Hz] for both flexural and torsional modes have been calculated by dividing the angular frequencies by the value ($2\,\pi$).

Damaged condition

A crack has been inserted in the beam to represent damaged cases for the target domain.

The longitudinal bending mode has been studied using an analytical formulation based on a perturbative solution [225]. A beam with a crack of length (a) positioned at a distance L^* ($e = \frac{L^*}{L}$) from the left support is considered in this method (see Figure 4.2 for crack and beam geometry). Such approach define $q(\alpha)$ and $\Theta(\alpha)$ as functions based on the crack ratio $\alpha = \frac{a}{h}$ and on the beam cross-section geometry.

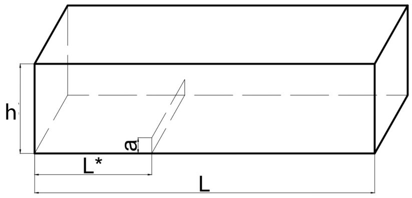

Fig. 4.2 Beam with a crack

For rectangular section:

$$q(\alpha) = \left(\frac{\alpha}{1-\alpha}\right)^2 (-0.22 + 3.82\,\alpha + 1.54\,\alpha^2 - 14.64\alpha^3 + 9.60\,\alpha^4) \tag{4.21}$$

$$\Theta(\alpha) = 2\left(\frac{\alpha}{1-\alpha}\right)^2 (5.93 - 19.69\,\alpha + 37.14\,\alpha^2 - 35.84\alpha^3 + 13.12\,\alpha^4) \tag{4.22}$$

Equation 4.23 yields a natural angular frequency ω_c as a function of Λ^2, a crack beam frequency parameter (Equation 4.24) that depends on a frequency parameter λ^2 (Equation 4.25), and a constant c (Equation 4.26).

$$\Lambda^2 = \left(\frac{\rho A}{E I}\right) L^4\, \omega_c^2 \tag{4.23}$$

In the following formulations *n* represents the mode number.

$$\Lambda^2 = \lambda^2 - 2n^2\pi^2 \left(\frac{h}{L}\right) \frac{(\frac{r^2}{s^2})\, q(\alpha)\, (1 - \frac{c}{n\pi})^2 \cos(n\pi e)^2 c^2\, \Theta(\alpha)\, s^2 \sin(n\pi e)^2}{s^2\,(1 + c^2 r^2)} \tag{4.24}$$

$$\lambda^2 = \frac{1 + (n\pi)^2 (r^2 + s^2) - \sqrt{(1 + (n\pi)^2 (r^2 + s^2))^2 - 4\,(n\pi)^4 r^2 s^2}}{2\, r^2 s^2} \tag{4.25}$$

$$c = n\pi - \frac{s^2 \lambda^2}{n\pi} \tag{4.26}$$

The natural frequencies [Hz] for each flexural mode have been calculated by dividing the angular frequencies by the factor 2π. The method has been found to be appropriate because, for small dimensionless crack lengths, such as those employed in this work, the findings are comparable to those obtained using the analytical method, and a reduced computing effort can be used.

Because there are no analytical formulations for flexural transverse and torsional modes, a FEM model has been created to estimate the variations to be applied to the frequencies of the undamaged beam to account for the influence of crack presence.

A beam made of 500 elements, bound at the ends by constraints that do not allow displacement in three directions and rotation with respect to the beam's development axis, is one such model produced using the Robot Structural Analysis software. Figure 4.3 depicts the model with the cracked element marked in blue.

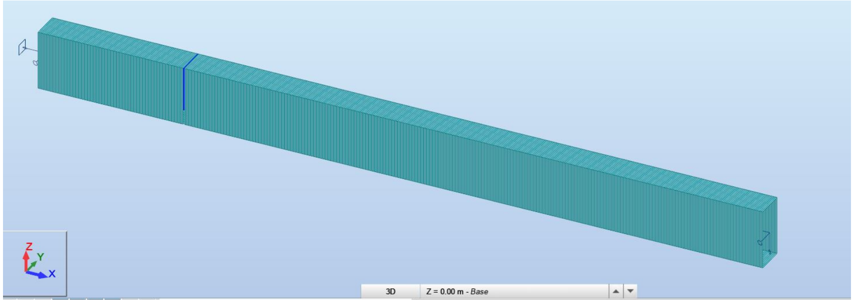

Fig. 4.3 Simply supported cracked beam

The ratio between the damaged and undamaged transversal/torsional frequencies in the FEM model is assumed to be the same as in the analytical model (MATLAB) in order to compute the flexural transverse and torsional modes in the damaged condition

4.3.2 Methods and results

The performance of classification has been evaluated using two methodologies: direct standardization in the original space and TCA with SD normalization pre-processing operation. For the three damage scenarios, the dispersion of the source and target datasets in the original space (parameter comb) and the length variation between the source and the target domain (parameter Δ) have been investigated.

Direct standardization

The percentages of false positives (error type I) and false negatives (error type II) relative to the total amount of undamaged and damaged data in the target structure, respectively, are used to quantify damage detection errors. In Tables 4.4, for the highest level of damage, 4.5, for the middle level of damage, and 4.6, for the lowest degree of damage, they are presented for all 45 examined cases. Figure 4.4 shows what happens in the five cases chosen as representative. In Tables 4.4 to 4.6, the values that relate to the chosen scenarios are also marked.

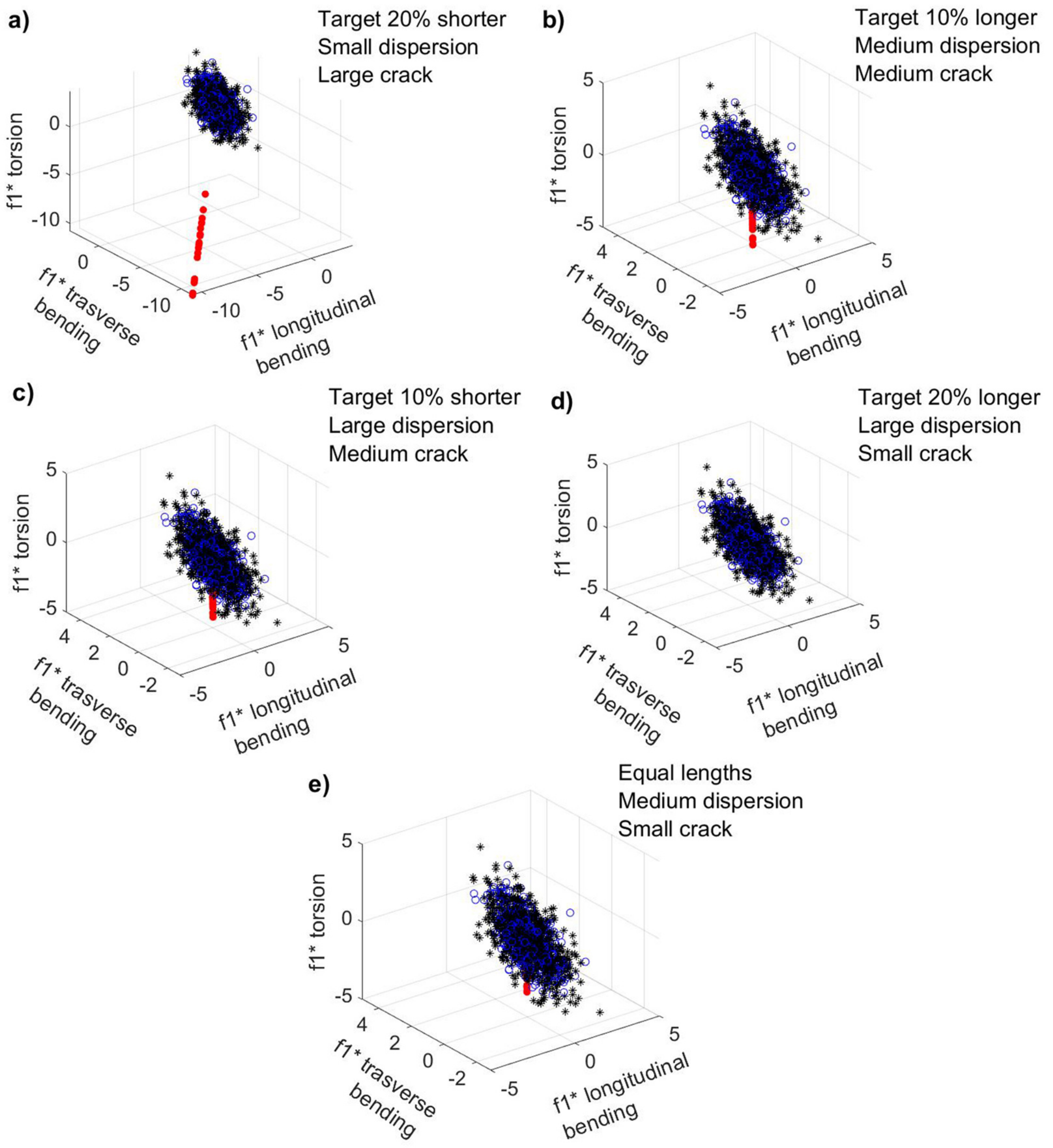

Fig. 4.4 Standardized space. Black (Healthy source data), Blue (Healthy target data), Red (Damaged target data.

The direct standardization with respect to the undamaged data shows Type I error (false positive error) about constant and equivalent to 4%. The Error Type II (false negative error) is stable with respect to the Δ parameter (except for Δ equal to

-0.1). The limited impact of the length difference between the source and the target structure means that the methodology is effective between geometrically different structures.

The error Type II is a function of the healthy source and target set dispersion (i.e., the parameter comb) as well as the severity of the damage. As the dispersion widens, so does the error. When the damage is of medium/low severity, such as in the DS12 and DS10 damage scenarios, this behavior emerges more clearly.

Large damage is always evident (see Table 4.4). Except for the significant dispersion, medium damage is also easily identifiable. The biggest false negative rate is associated with the largest dispersion (see Figure 4.4(c)), where considerable overlap between the damaged and undamaged target data results in the incorrect classification of 9 out of 20 damaged points. Only in the situation of a small dispersion of undamaged data is a small level of damage clearly identifiable (see Table 4.6).

Particularly for the lowest and middle levels of damage, the classification performance is heavily reliant on the dispersion of the target data that has not been damaged (see Tables 4.5 and 4.6). The smallest dispersion for such damage levels involves damaged data points being evenly spaced from the undamaged ones. As can be observed in Figure 4.4(b), the damage data points for the medium dispersion are quite distanced from the undamaged ones for the medium level of damage, and the false negatives range from 15% to 25%. On the flip side, as shown in Figure 4.4(e), the majority of damaged readings are incorrectly classified for the small damage case. For the medium and smallest damage levels, respectively, the majority or all damaged readings are not correctly classified due to the biggest dispersion. In fact, the damage measurements partially or entirely overlap the undamaged data (Figure 4.4 (c) and (e)).

Table 4.4 Errors in damage identification for different length differentials and levels of dispersion for a 15 mm crack depth

					DS15					
Δ	**0.2**		**0.1**		**0**		**-0.1**		**-0.2**	
Type of error [%]	**I**	**II**	**I**	**II**	**I**	**II**	**I**	**II**	**I**	**II**
Comb1	4.3	0	4.3	0	4.3	0	4.3	0	**4.3**	**0**
Comb2	4.3	0	4.3	0	4.3	0	4.3	0	4.3	0
Comb3	4.3	5	4.3	5	4.3	10	4.3	0	4.3	10

Table 4.5 Errors in damage identification for different length differentials and levels of dispersion for a 12 mm crack depth

					DS12					
Δ	**0.2**		**0.1**		**0**		**-0.1**		**-0.2**	
Type of error [%]	**I**	**II**	**I**	**II**	**I**	**II**	**I**	**II**	**I**	**II**
Comb1	4.3	0	4.3	0	4.3	0	4.3	0	4.3	0
Comb2	4.3	15	**4.3**	**15**	4.3	25	4.3	0	4.3	25
Comb3	4.3	80	4.3	80	4.3	90	**4.3**	**45**	4.3	90

Table 4.6 Errors in damage identification for different length differentials and levels of dispersion for a 10 mm crack depth

					DS10					
Δ	**0.2**		**0.1**		**0**		**-0.1**		**-0.2**	
Type of error [%]	**I**	**II**	**I**	**II**	**I**	**II**	**I**	**II**	**I**	**II**
Comb1	4.3	0	4.3	0	4.3	0	**4.3**	**0**	4.3	0
Comb2	4.3	70	4.3	70	**4.3**	**80**	4.3	10	4.3	75
Comb3	**4.3**	**100**	4.3	100	4.3	100	4.3	100	4.3	100

TCA with an SD normalization preprocessing

Similar to Direct standardization, the percentages of false positives (error type I) and false negatives (error type II) in relation to the total number of undamaged and damaged data in the target structure, respectively, are used to describe damage detection errors. Tables 4.7, 4.8, and 4.9 for the highest level of damage, the middle level of damage, and the lowest level of damage, respectively, show them for each of the 45 testing scenarios. They are referred to analyses carried out with the regularization parameter μ set at 0.1. Figure 4.5 displays the plots of the data distribution in the latent space for the five chosen scenarios. Tables 4.7 to 4.9 further emphasize the values corresponding to the chosen cases.

Since TCA is not normalizing the SD, we are always doing it in the original space, and then run TCA and go to the latent. For both the source and target domains, this type of standardization has been done with regard to the undamaged samples.

Table 4.7 Errors in damage identification for different length differentials and levels of dispersion for a 15 mm crack depth

DS15										
Δ	**0.2**		**0.1**		**0**		**-0.1**		**-0.2**	
Type of error [%]	**I**	**II**	**I**	**II**	**I**	**II**	**I**	**II**	**I**	**II**
Comb1	12.6	0	12.6	0	12.3	0	14.6	0	**12**	**0**
Comb2	5	0	5.3	0	5.3	0	5	0	5	0
Comb3	4	10	3.6	10	3.6	10	4.3	0	4.3	10

Table 4.8 Errors in damage identification for different length differentials and levels of dispersion for a 12 mm crack depth

DS12										
Δ	**0.2**		**0.1**		**0**		**-0.1**		**-0.2**	
Type of error [%]	**I**	**II**	**I**	**II**	**I**	**II**	**I**	**II**	**I**	**II**
Comb1	6.6	0	6.3	0	6.3	0	8.3	0	6.3	0
Comb2	3.6	15	**3.3**	**15**	3.6	20	4	0	3.6	15
Comb3	3.6	70	3.3	70	3.6	70	**4**	**40**	4	70

Table 4.9 Errors in damage identification for different length differentials and levels of dispersion for a 10 mm crack depth

	DS10									
Δ	**0.2**		**0.1**		**0**		**-0.1**		**-0.2**	
Type of error [%]	**I**	**II**	**I**	**II**	**I**	**II**	**I**	**II**	**I**	**II**
Comb1	5	0	5	0	4	0	5.3	**0**	4	0
Comb2	3.3	70	3.3	70	**4**	**70**	4.3	10	4	70
Comb3	**3.6**	**100**	3.6	100	3.6	100	4	90	4	100

In all 45 of the examined examples, TCA with an SD normalization pretreatment of the frequency data appears to be able to identify the target structure's normal behavior. False positive errors, in contrast to the direct standardization method, are not constant and appear to be impacted by the degree of dispersion of the undamaged data. The impact of the dispersion of the undamaged data becomes increasingly apparent as the damage levels rise.

As can be seen from Table 4.7, large damages are always straightforward to recognize although the classification performance is slightly subpar compared to the direct standardization technique. Except for a significant dispersion, medium damage is also easily identifiable. The biggest false negative rate is associated with the largest dispersion condition (see Figure 4.5(c), where some overlap between the undamaged and damaged target data results in the misclassification of 8 out of 20 damaged points. The false negatives for the medium damage level are a little bit lower than those from the direct standardization method. As concern the small level of damage, it is clearly identifiable only in the case of small dispersion of undamaged data (see Table 4.9).

Particularly for the lowest and middle levels of damage, the classification performance is heavily reliant on the dispersion of the target data that has not been damaged (Tables 4.8, 4.9). The damaged data points are sufficiently spaced from the undamaged ones for both damage scenarios for the smallest dispersion condition. The damage data points are adequately separated from the undamaged ones for the medium level of damage in the medium dispersion example, and the false negatives range from 15% to 20%, as can be observed in Figure 4.5(b). On the other hand, the majority of damaged readings are incorrectly classified when the small level of damage is present (Figure 4.5 (e)). For the medium and lowest damage levels, respectively, the majority or all damaged readings are not correctly classified in the largest dispersion case. In fact, the damage measurements partially or entirely overlap the undamaged data (Figure 4.5 (c) and (e)). TCA displays a type two error for medium and low damage levels that is a little bit lower than what the direct standardization technique provides.

The length difference between the source and target structures appears to have a very small impact on the classification performance. For this reason, TCA between structures that are geometrically significantly dissimilar from one other turns out to be possible, similar to the direct standardization technique.

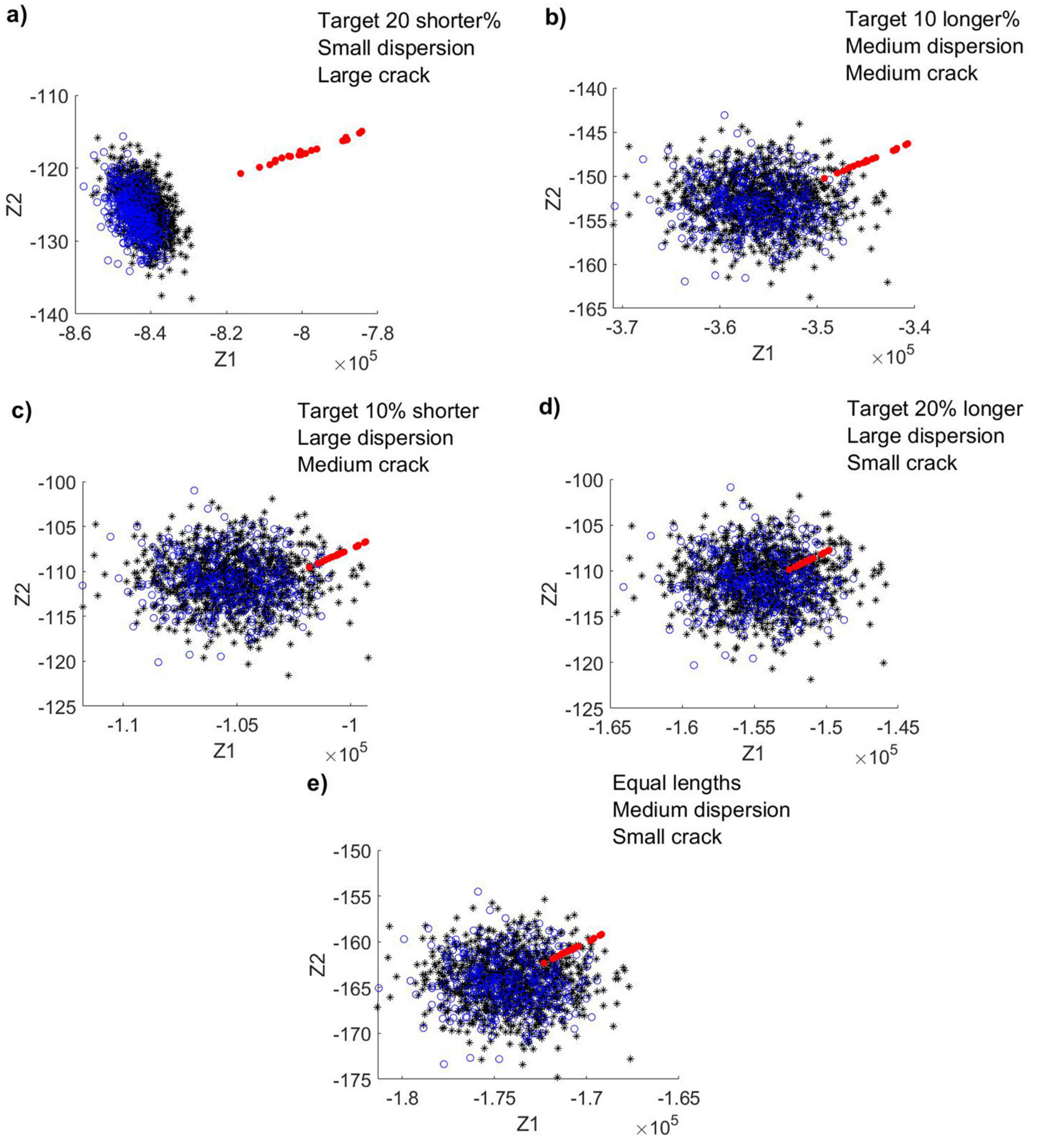

Fig. 4.5 Latent space. Black (Healthy source data), Blue (Healthy target data), Red (Damaged target data)

4.4 Transfer learning between two pedestrian bridges

4.4.1 Structures and data set description

In Campo Grande, district of Lisbon, there are two similar pedestrian bridges distanced by 225 m. Herein we designated them as Bridge Target (Figure 4.6) and Bridge Source (Figure 4.7).

Fig. 4.6 Bridge Target.

Both bridges are in front of Lusofona University's Campus and are characterized by a superstructure consisting of two prefabricated beams in reinforced and prestressed concrete, with two I-shaped cross section beams linked by simply supported slabs at the bottom flanges, as shown in Figure 4.8.

Fig. 4.7 Bridge Source.

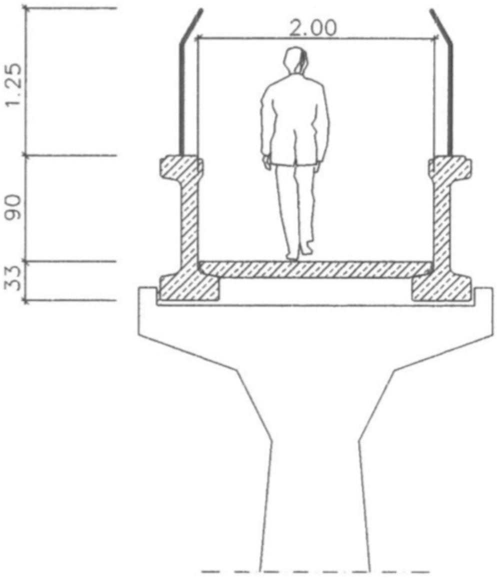

Fig. 4.8 Typical cross section of both bridges.

On March 2, 2022, 45-min ambient field test was performed on the Bridge Target's deck (Figure 4.9) in order to study the influence of mass variability on its modal properties. Assuming an average of 65 kg per person, the total additional mass caused by 56 people on the deck over 10 min may be approximated by 3640 kg.

Fig. 4.9 Ambient vibration test on Bridge A with additional mass caused by pedestrians.

The total data set is made up of: 90 samples related with the healthy condition for the Source Bridge, 109 samples related with the healthy condition for the Target

Bridge, and 10 samples related with the damaged condition for the Target Bridge (simulated with the additional mass).

4.4.2 Methods and results

Figure 4.10 shows the first three natural frequencies for both pedestrian bridges in the original space.

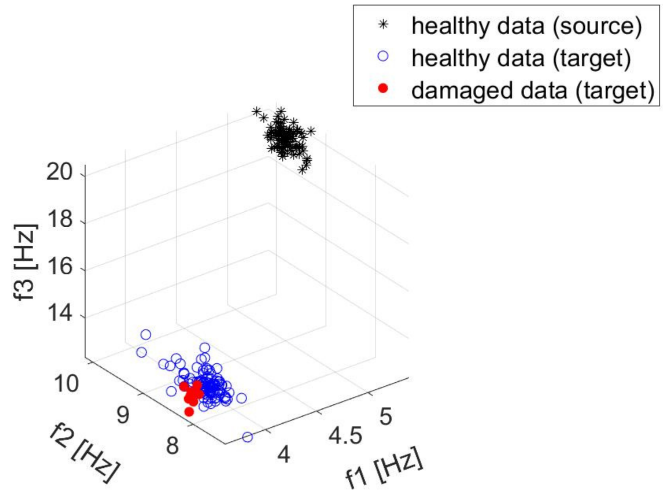

Fig. 4.10 Original space

Direct standardization

Table 4.10 displays the results obtained with the Direct standardization strategy and Figure 4.11 shows a 3D plot of the first three frequencies after such operation. This strategy shows optimal damage detection capability.

Type I error [%]	**Type II error[%]**	**Total [%]**
8.25	0	7.56

Table 4.10 Error with Direct standardization strategy

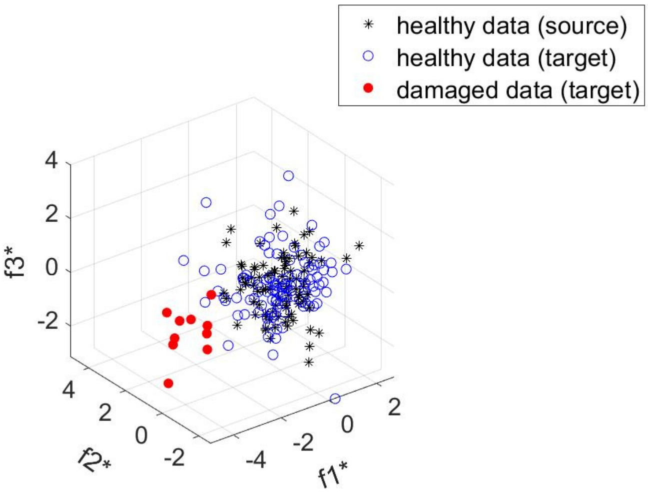

Fig. 4.11 Standardized original space

TCA with SD normalization preprocessing

Table 4.11 shows the results obtained with the TCA with SD normalisation preprocessing strategy. Figure 4.12 displays the two components Z1 and Z2 in the latent space. This strategy shows the same Type I error as the previous one. The Type II error is higher but the damage detection capability remains good.

Type I error [%]	**Type II error[%]**	**Total [%]**
8.25	30	10.08

Table 4.11 Error with strategy "TCA with SD normalization preprocessing"

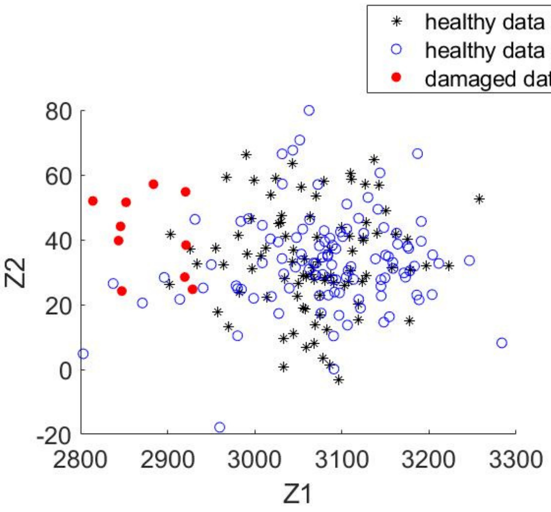

Fig. 4.12 Latent space

4.5 In Closing

In this Chapter, numerical analyses have been firstly carried out to understand the potential and limitations of domain adaptation (transfer learning) and standardization techniques for pedestrian bridges. They demonstrate that the effect of length variation (Δ parameter) between beams in the source and target domains is negligible on the results. This is a strength for the application of such techniques for similar structures but which may have differences in their size. As can be seen from a comparison of Tables (4.4, 4.5, 4.6) and (4.7, 4.8, 4.9), the two techniques are both dependent on the dispersion of the data in the undamaged condition. The Direct Standardisation technique shows a constant Type I error (around 4%) and slightly lower damage detection capability for medium and low severity damage (DS12-D10) than TCA. On the other hand, the TCA technique shows a non-constant but still adequate Type I error in most cases (less than 15%) and a consistent damage detection capability. The application of these two techniques to a real case has showed encouraging results for both techniques, making them worthy of further investigation.

Chapter 5

Deep convolutional neural network support in a multi-level non-invasive tunnel assessment[1]

5.1 Problem definition

After bridges, tunnels are the second most common engineering element in Italy's infrastructural assets. The latter is made up of approximately 33,500 bridges and 2,500 tunnels. Due to the size of the asset, new automatic control plans are clearly required. The current state of infrastructure aging, further, adds the necessity of their creation and execution. Indeed, most of infrastructures date from the 1960s and are, thus, very vulnerable to age-related deterioration. Structural conditions may differ from the original design due to several factors such as structural deformations and damages, voids, material deterioration [226], water leakages [227–232], frost damage mechanisms [233], earthquake cracks [234], and construction defects.

---

[1] Part of the work described has been previously published in:
B. Chiaia, G. Marasco, S. Aiello. Deep convolutional neural network for multi-level non-invasive tunnel lining assessment. Frontiers of Structural and Civil Engineering 16 (2), 214-223 (2022).
G. Marasco, M.M. Rosso, S. Aiello, A. Aloisio, G. Cirrincione, B. Chiaia, G. C. Marano. Ground Penetrating Radar Fourier Pre-processing for Deep Learning Tunnel Defects' Automated Classification. In: Iliadis, L., Jayne, C., Tefas, A., Pimenidis, E. (eds) Engineering Applications of Neural Networks. EANN 2022. Communications in Computer and Information Science, vol 1600. Engineering Applications of Neural Networks, 165-176 (2022).

5.2 Methodology

This section will illustrate the proposed methodology for developing a tunnel control plan. It lays the foundations in the use of a specific technology/instrumentation (*GPR*), the outputs of which will be processed through deep learning algorithms inserted within an analysis flow.

5.2.1 Ground Penetrating Radar

A *GPR* campaign produced the images utilized in the damage classification. This technology is a non-destructive screening approach [235] that is commonly utilized in civil engineering applications [236], specifically for analyzing the structural conditions of tunnels [237]. Concrete void identification [238], subsurface utility tracking [239] , railway ballast optimization and evaluation [240], and landmine detection [241] are just a few of the uses. Such instrument is well-known for its high penetration capability as well as its ease of use and transportation [242]. As a result of these capabilities, it is a useful tool for detecting and locating damage.

GPR is a geophysical [243] survey method that involves sending high-frequency electromagnetic wave impulses into a material using an antenna with a frequency ranging from 10 to 2600 MHz. The dielectric characteristics of the material influence the propagation of such an impulse. As a result, certain factors, such as water, have a large impact on the quality of the representation. Indeed, due to its presence a portion of the signal is reflected and attenuated, resulting in a rendering that is less clear and intelligible. The images used in this investigation have been obtained through the use of two *GPR* by the RINA company. The first used a dual-frequency antenna, whereas the second used a high-frequency antenna. The technical elements of each are reported in Tables 5.1 and 5.2.

Table 5.1 Technical characteristics of GPR with dual frequency antenna.

Characteristics	**Value**
Minimum number of channels	4
Pulse repetition frequency (kHz)	400
Range (ns)	0-9999
Min. number of scans (scans/second)	400
Voltage (V)	12
Primary dual-frequency antenna (MHz)	400-900
Secondary dual-frequency antenna (MHz)	200-600

Table 5.2 Technical characteristics of GPR with high-frequency antenna.

Characteristics	**Value**
Minimum number of channels	4
Pulse repetition frequency (kHz)	400
Range (ns)	0-9999
Min. number of scans (scans/second)	400
Voltage (V)	12
High-frequency antenna (GHz)	≥ 2

The dual-frequency antenna has been used to acquire longitudinal profiles, the number and layout of which have been determined by the number of lanes and tunnel dimensions (Figure 5.1). *GPR* scans using a high-frequency antenna, on the other hand, can be longitudinal or transverse. This is dependent on the level of detail necessary.

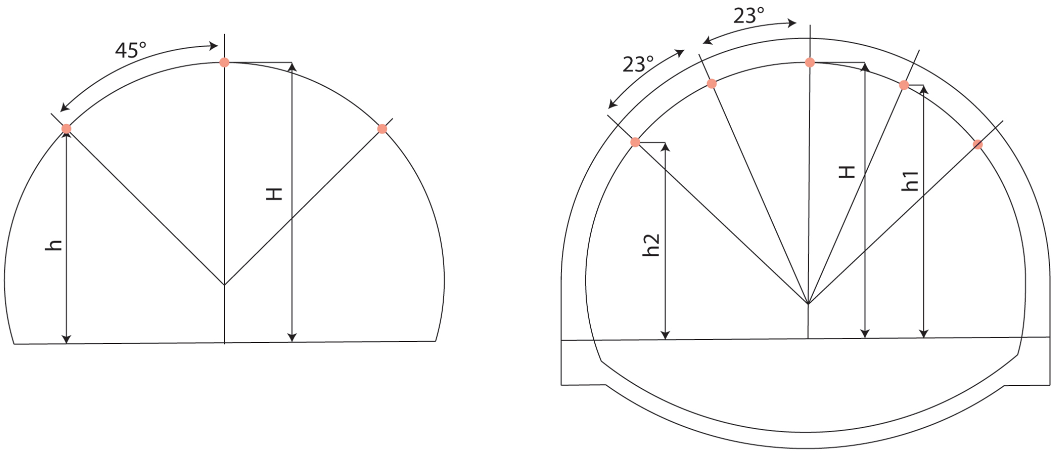

Fig. 5.1 2-lane tunnel (3 profiles) and 3-lane tunnel (5 profiles).

Database creation: image pre-processing and engineering judgement

The database used to develop and evaluate the proposed methodology is made up of images (input), namely *GPR* profile, that are linked to a specific structural state (output). Image-based analysis (*IBA)*, i.e., visual recognition methods of certain patterns with qualified inspectors, as well as a range of additional tests, such as transverse *GPR*, jack, pull-out, core drilling, and videoendoscopy, have been used to support the profile interpretation and, consequently, the categorization process. It is worth noting that the longitudinal *GPR* profiles have been acquired through a B-scan visualization and pre-processing images have been taken prior to their use.

First of all it is essential to dwell on the *GPR* profile characteristics. Such profiles have a vertical axis that represents the depth of the investigated thickness and a horizontal one that represents the progressive distance from the structure's beginning. Figure 5.2 shows an example of a *GPR* profile with interpretations.

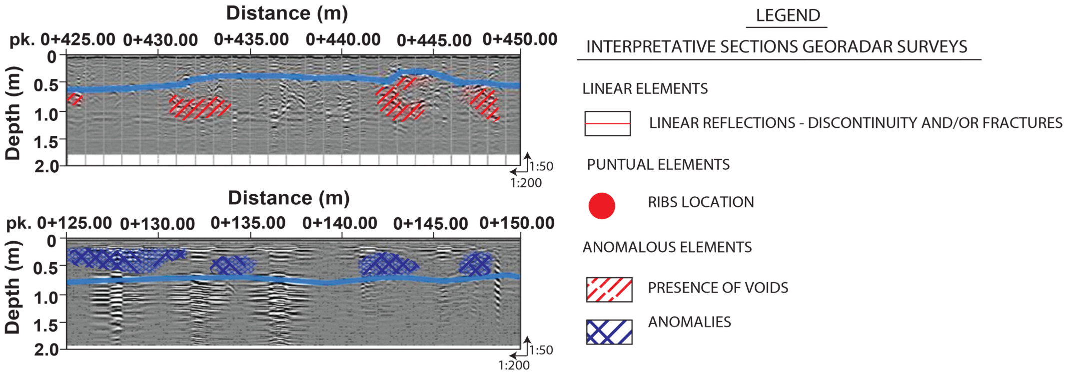

Fig. 5.2 GPR interpretation

Noise, sound tails, and interferences can impact *GPR* profiles. Their interpretation, whether done by experts or by an algorithm, might be hindered by external noise. Therefore, the RINA company has implemented four types of filters. To properly interpret the studied depth, the first filter ("Move start time") has been utilized to remove the part of the signal between air and examined medium. The second (“Background removal”), the third (“Bandpass filter”), and the fourth (“Smoothed gain”) one have filtered the noise, the high frequencies, and equalized the power, respectively. The first executed pre-processing procedure has been the profile cutting, which started with filtered *GPR* profiles. Each profile has been split down into components with sizes ranging from 112 to 600 horizontal pixels and 110 to 564 vertical pixels. This operation has been performed with the aid of PineTools’ free web tools. The second operation to effectively use such profiles in the proposed methodology, is the axes removal. Then, a data augmentation strategy has been utilized to increase the classification performance. This strategy proved to be quite beneficial, as many studies in the literature [244] have shown. The horizontal flip augmentation [245, 246], which involves rotating images around the vertical axis, has been exploited. Microsoft Office Picture Manager has been used to perform this task. Except for the images relating to healthy conditions, such method has been carried out for all of the classes. The presence of a large number of images in this class led to this decision. After performing the operations outlined thus so far, the database has been created by associating the ith image to its class. It is pointed out that each input has a resolution of 96 dpi. The samples are labelled on the basis of the interpretations provided by the defect recognition phase carried out by the human experts. This has been done by comparing the filtered *GPR* profiles without interpretations to the reports that included them and their interpretations.

5.2.2 Convolutional Neural Network and Transfer Learning

Among deep learning algorithms for image classification, convolutional neural networks (CNNs) stand out. Beginning in the 1980s, studies on the visual cortex of the brain have investigated CNNs. Nevertheless, it has only been in the last ten years that they have become a dominant force in the DL field due to improved processing power and access to training data [247]. Moreover, the CNNs exploits transfer learning methodology adopting pre-trained models tailored to certain tasks with fine-tuning techniques, further reducing down the computing cost [248].

ResNet-50 has been selected among the known pre-trained neural networks(e.g., AlexNet, SqueezeNet, ShuffleNet, ResNet-18, GoogLeNet, ResNet-50, MobileNet-v2, and NASNetmobile) and then used within the MATLAB programming environment to accomplish the classification problem. He et al. [249] created this *CNN* in 2015. Around 25 million parameters make up ResNet-50. There are 177 layers in all, 49 of which are convolutional and one of which is fully connected. It is pre-trained on the ImageNet Large Scale Visual Recognition Challenge (*ILSVRC*) image classification and localization dataset. Through 1,281,167 training images, 50,000 validation images, and 100,000 test images, the network is able to classify 1,000 object classes [250, 251].

In order to better understand the entire transfer learning process, it is deemed useful to take a closer look at the initial network training database and how it was constructed. Following a brief description of the ILSVRC public image dataset. The synset hierarchy of ILSVRC can be seen as a "reduction of the full ImageNet one. Therefore, a quick explanation of the ImageNet dataset is required to obtain an overall framework. Large-scale image ontology "ImageNet" was created using the WordNet structure as its foundation. The hierarchical organization of WordNet is adopted by ImageNet [252]. A "synonym set" or "synset" is the term used to represent any relevant concept in WordNet that may be expressed by several words or word phrases. For each synset in ImageNet, there are on average of 500–1000 images. There is a quality-checked and human-annotated for each images. The gathering of potential images for each synset is the initial step in the creation of ImageNet. By using multiple image search engines, the images are found on the Internet. In order to gather a reasonably precise dataset, researchers rely on people to check each candidate image gathered in the prior stage for a certain synset. This is accomplished by utilizing the Amazon Mechanical Turk (AMT) service, a website where assignments can be posted for individuals to perform and be paid. A quality check is carried out on user ratings; multiple users are asked to label the same image and a minimum level of agreement is established between them for the purpose of such labelling. The method used to build ImageNet is the same one used for the task of collecting images for ILSVRC classification [253]. Directly pulled from ImageNet are the training images. As regards the validation and test set, further images are gathered with the same methodology.

After the description of the initial database just given, the characteristics of the chosen network, ResNet-50, are discussed in more detail. ResNet-50 is characterized as a "feed forward" neural network with "residual/skip connections" that uses the Rectified Linear Unit (*ReLu*) and the softmax as activation functions. Its development arose from the identification of an unexpected phenomenon: "raising the depth of network, layers increases the chance of making the network worse". Deeper neural networks should perform better than shallower ones, or at the very least, exhibit better results during the training phase. Indeed, the overfitting phenomenon is not possible during this phase. Nevertheless, it is well recognized that as the network's depth grows, the rise in accuracy is not always validated, resulting in a degradation problem. The presence of a residual unit (skip connection) that allows ResNet to learn the differences between the input and output layers is an innovative feature that sets it apart from similar competitors. Excessive depth can be mitigated in this way. ResNet has been chosen to face the classification task for its high network depth and its fairly low computational level [254]. In detail, as mentioned above, Res-Net-50 adopted in the present study was implemented in the MATLAB2021a programming environment by adopting the pre-trained model on the ILSVRC public image dataset. By means of a fully connected layer with 1000 units and a softmax layer, the initial/baseline pre-trained ResNet-50 was capable of categorizing images into 1000 different object classes.

To fit the needs of the current investigation, it was modified. To perform the binary classification tasks for each hierarchical level, the final fully connected layer has been modified. The hyperparameters reported in 5.3 have been used to fine-tune the network to perform binary classifications.

Table 5.3 Hyperparameters

Learning rate	**Mini-bach size**	**Max epoch**
0.001	32	12

5.2.3 Multi-level damage classification

The proposed methodology for tunnel lining condition assessment has been designed in six levels, as shown in the flowchart in Figure 5.3.

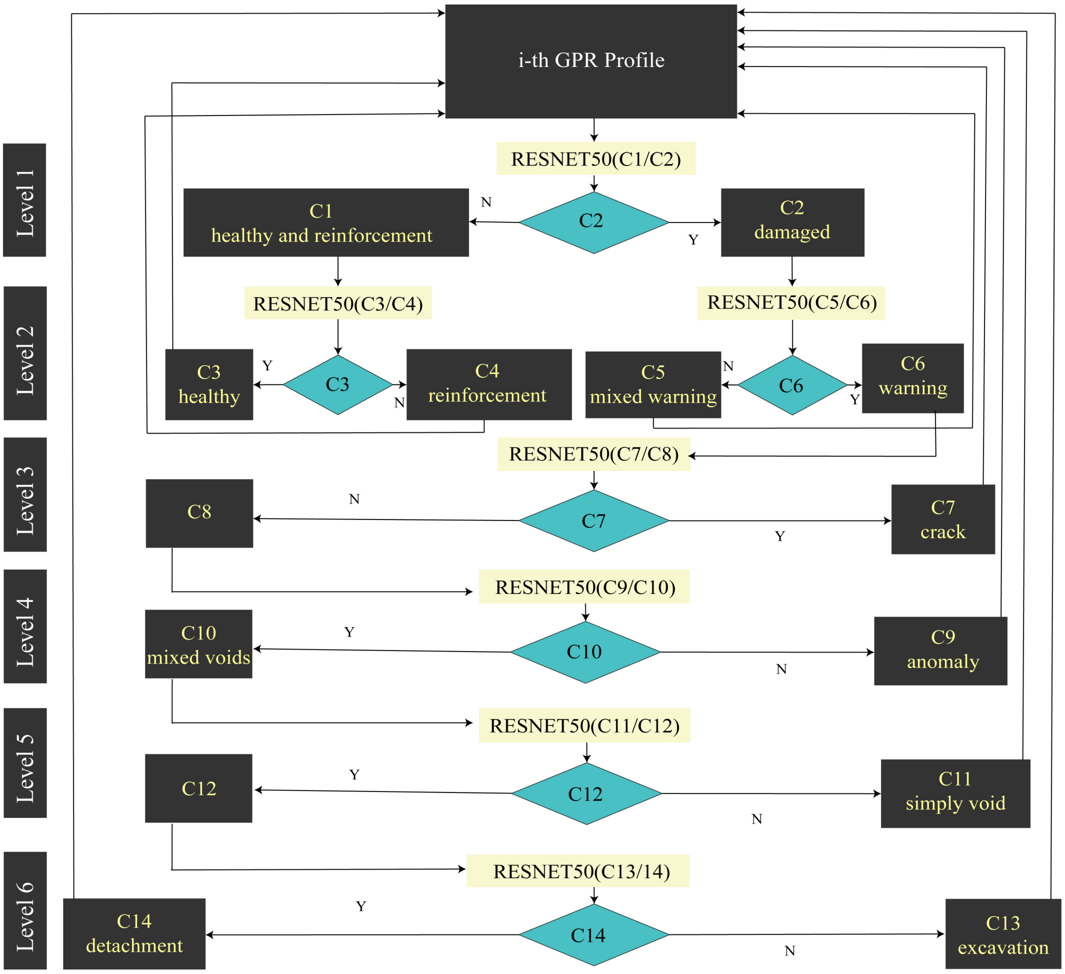

Fig. 5.3 Multi-level damage classification methodology flowchart

As illustrated by the hierarchical tree in Figure 5.4, the total number of samples for each level is progressively decreasing.

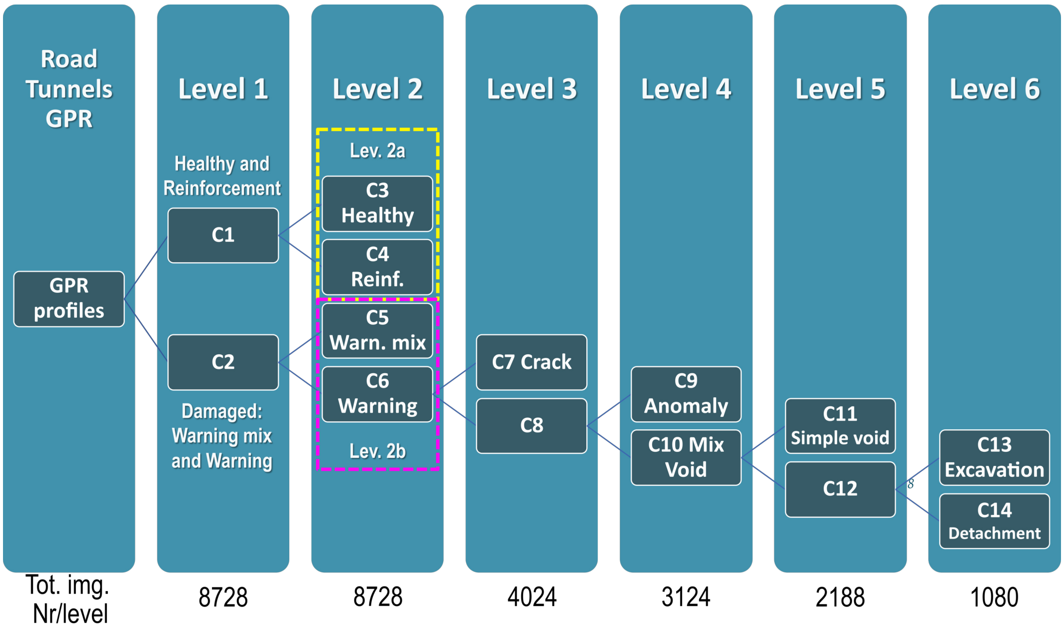

Fig. 5.4 Hierarchical tree for the multi-level approach

As reiterated and expanded upon in the Section 5.3, to obtain a good classification model, a balanced approach was forced from the class with the minimum number of samples. Table 5.4 reports the number of samples per class for each level.

Table 5.4 Samples for class.

Level	**Value**
1	4130
2a	492
3	900
4	936
5	1080
6	408

It is feasible to gain more precise knowledge regarding the presence and type of structural damage as one progresses from the lower to the higher levels. This strategy attempted to draw more attention to the important issues that required a more in-depth assessment of the current structural degradation. This idea is similar to that described in Italy's newly passed "New guidelines for the classification and management of risk, safety assessment, and monitoring of existing bridges" (2020).

When a *GPR* profile is examined, it can be classified into one of 14 categories, which are listed follows.

- C1: Healthy and Reinforcement. Images connected with a healthy structural condition and the likely presence of reinforcement, notably covering centring, make up this class;
- C2: Damaged. Images containing at least one or more types of damage are in this class;
- C3: Healthy. This class is composed by images representing healthy structural condition;
- C4: Reinforcement. Images with reinforcement, such as covering centring, are included in this class;
- C5: Mixed warning. Images in this class are characterized by the combination of two or more types of damages;
- C6: Warning. This class is formed by images showing a single type of damage. The potential damages are anomalies, cracks, simply voids, detachments or excavations;
- C7: Crack. The presence of cracks is a distinguishing feature of images in this class;
- C8: Anomalies, simply voids, detachment or excavation are the damages that can appear in the images in this class;
- C9: Anomaly. This class of images contains anomalies, such as inhomogeneity of the covering casting. Aging concrete, temperature variations, wrong with the casting, crawl spaces, and reduced injuries are among the causes of this phenomena;
- C10: Mixed voids. Voids of different nature are shown in the images of this class;
- C11: Medium-sized and deep voids characterize the images of this class;

- C12: The detachment and excavation phenomena are shown in the images in this class. The C13 and C14 classes, respectively, provide a more extensive description of such phenomena;
- C13: Detachment. This phenomenon results in an exterior void, as well as some cracks;
- C14: Excavation. This phenomenon results in a large internal void.

The proposed methodology is applied both to *GPR* profiles subjected only to the preprocessing operations described so far (Section 5.2.1) and to those subjected to a further operation consisting in the bidimensional Fourier Transform. Details and theoretical deepenings concerning this technique are reported in the Section 5.2.4.

5.2.4 Two dimensional Fourier Transform for image processing

The Fourier Transform (*FT*) is a signal processing method that decomposes a signal into its fundamental components. Furthermore, it performs domain mapping, which involves transferring the representation of the problem from the spatial or time domain to the Fourier or frequency domain. The *FT* expresses a signal as an infinite sum of harmonics distinguished by distinct frequencies and specifying the frequency content of each one for continuous phenomena. Even with the most advanced instrumentation, data is acquired discretely through a sampling procedure in the actual world. When the sampling frequency is two times the Nyquist frequency, which is the greatest signal representable frequency, any continuous signal may be reliably and uniquely reconstructed from its samples, according to the Nyquist-Shannon sampling theorem. [10] [23]. The Discrete version of the FT (*DFT*) has been created to cope with real-world sampled signals that are discrete signals. A digital image is typically represented by a matrix/tensor of pixels, with each pixel containing specific values. A gray-scale image with 8-bit precision is a matrix in which each pixel can take on an integer value between 0 and 255. A red-green-blue (*RGB*) image, on the other hand, is represented by a tensor with a depth-size of three, in which each pixel is encoded by three bytes because each color channel can take integer values ranging from 0 to 255 [255]. By examining the vertical and horizontal directions, an image can be interpreted as two-dimensional signals of pixel values without affecting generality [256]. As a result, a 2D discrete-space signal (digital image) can be decomposed into its main sinusoidal components using the *FT*. Only a specific amount of harmonics are obtained due to the sampling frequency. It must, nevertheless, be adequate to represent the information in the image [257]. Considering a digital image in the spatial domain A of size $n \times m$ with components a_{rs}, with $0 \leq r \leq n-1$, $0 \leq s \leq m-1$, the discrete 2D-FT (*2D-DFT*) is a matrix F in the Fourier domain of size $n \times m$ with components [255]:

$$f(k,l) = \sum_{r=0}^{n-1} \sum_{s=0}^{m-1} a(r,s) e^{-2\pi i\left(\frac{kr}{m}+\frac{ls}{n}\right)} \tag{5.1}$$

where: $0 \leq k \leq n-1$, $0 \leq l \leq m-1$. Essentially, the 2D-FT sums the products of the spatial image input and the sinusoidal basis functions, which are written in complex exponential form. The term $f(0,0)$ represents the direct current (*DC*) component which is the average brightness of the input image, whereas the last realization $f(n-1,m-1)$ corresponds to the maximum frequency component [257]. The inverse 2D-FT (2D-IDFT) is defined as follows:

$$a(r,s) = \frac{1}{n \cdot m} \sum_{k=0}^{n-1} \sum_{l=0}^{m-1} f(k,l) e^{2\pi i\left(\frac{kr}{m}+\frac{ls}{n}\right)} \tag{5.2}$$

To reduce the computational effort, it is possible to show that the 2D-DFT may be computed as a series of $2n$ one-dimensional FT [257], resulting in a computational complexity of $O(n^2)$. To further decrease the complexity to $O(n \log_2(n))$ [257] Fast Fourier formulations (2D-FFT) have been created. The FT operation produces a complex matrix that can be represented by real and imaginary parts, or, more commonly, by magnitude and phase. In many applications, the phase is ignored because the majority of the information is contained inside the magnitude. Nevertheless, if the original image must be reconstructed using the 2D-IDFT, the phase information is absolutely crucial to avoid corrupted image reconstruction [257]. Since the magnitude of the greatest DC component with relation to the other frequencies might be quite scattered, a logarithmic transformation is generally used to increase the information contained in low-frequency components:

$$\tilde{f}(k,l) = c \log(1 + M_{k,l}) \tag{5.3}$$

where c is a scaling factor set to unity in the present research, and

$$M_{k,l} = \sqrt{\Re(f(k,l))^2 + \Im(f(k,l))^2} \tag{5.4}$$

is the magnitude for each pixel in the frequency domain. Among the many helpful aspects of the FT, the convolution property is the most essential. Thanks to it the convolution operation in the input domain becomes a strainghtfoerward multiplication in the Fourier domain. Digital filters can be used in image processing to smooth an image by suppressing high frequencies or to detect edges by deleting low frequencies. [257]. These operations are accomplished by a filter kernel function $h(r,s)$ which slides on the image and computes a correlation between the kernel receptive field and the input image: $g(r,s) = h(r,s) * a(r,s)$. Specifically, the convolution is a correlation procedure operating with a flipped kernel $h(-r,-s)$. The above-mentioned computation, which is at the basis of convolutional neural networks (*CNN*), may be performed more effectively in the frequency domain thanks to the convolution property.

In the current study, the 2D-FFT has been adopted to perform a pre-processing of the *GPR* linings profiles described so far. This procedure may aid in data compression whereas preserving the geometric structure of the original digital image. The 2D-FFT recognizes vertical and horizontal patterns in the input image whereas keeping information about such alignments in the Fourier domain's most dominant frequency components. Additionally, as shown in Figure 5.5, the 2D-FFT enables for the removal of horizontal periodic components, characteristic of the *GPR* profiles in the depth direction. The impacts of 2D-FFT preprocessing on *GPR* profiles acquired from the road tunnel survey campaign are shown in Figure 5.5 through two examples.

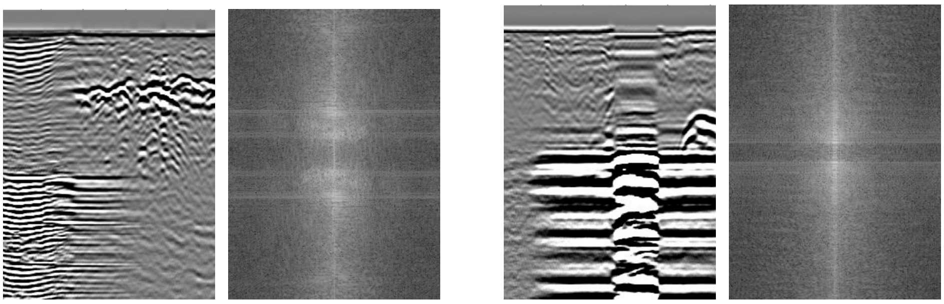
(a) (b) (c) (d)

Fig. 5.5 Two examples of 2D-FFT pre-processing of road tunnels GPR profiles. (a) and (c): samples extracted from the entire GPR profile; (b) and (d): 2D-FFT magnitude pre-processed images

5.3 Results

A confusion matrix and an accuracy value have been utilized to check the algorithm classification performance for each level. The actual classes have been shown in the rows of the confusion matrix, whereas the predicted labels in the columns. A correct classification coincides to the values placed on the diagonal of the matrix. The ratio between the confusion matrix trace and the total sum of the matrix values has been used to get the accuracy value. The displayed confusion matrices and accuracies have been calculated as an arithmetic mean based on the results of ten (as stated below) test folds obtained using a K-fold validation technique. Furthermore, an error estimation using the Root Mean Square Error (*RMSE*) index has been computed for each of the test folds, and then their average has been calculated and used as the final indicator. It is worth mentioning that the training of the algorithm for the six levels used the same number of data for both classes. With this homogeneity, no specific methodologies have been needed to address issues of class imbalance [258]. The data of each class have been randomly divided into k groups (folds) using the K-fold validation methodology, with one "fold" utilized for testing, one for validation, and (k-2) folds for training [259, 260]. The cross-validation has been performed with a split value of k equal to 10. As outlined by empirical evidence, such a value generates test error rate estimates that are free of both significant bias and wide variance [261]. Lastly, an additional tool for evaluating the models has been the convergence graph (loss/accuracy versus number of iterations). Figure 5.6 depicts the loss/accuracy versus the number of iterations for one of the ten cases related to the Level 1, using the *GPR* profile (without the bidimensional Fourier Transform) and shows the adherence of the trend to the expected behavior.

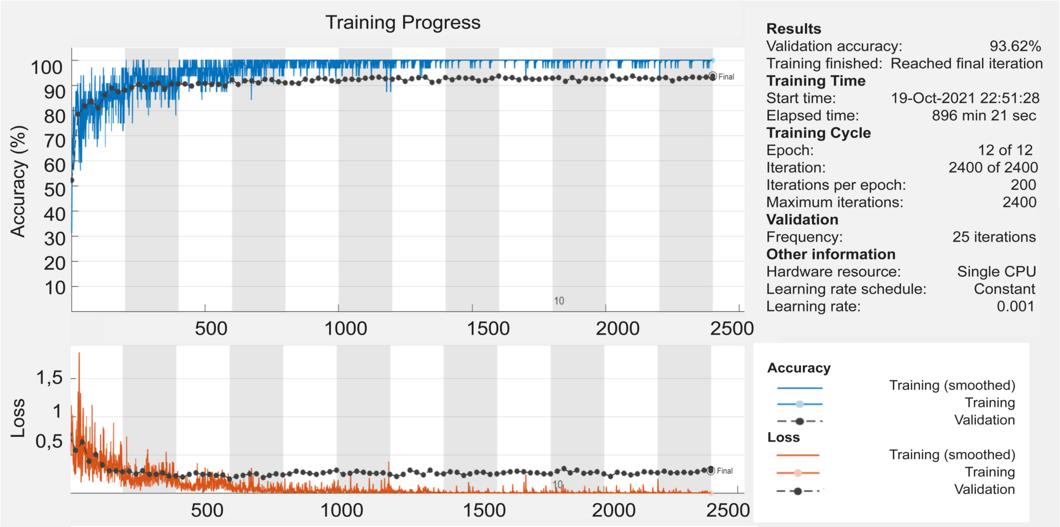

Results
Validation accuracy: 93.62%
Training finished: Reached final iteration
Training Time
Start time: 19-Oct-2021 22:51:28
Elapsed time: 896 min 21 sec
Training Cycle
Epoch: 12 of 12
Iteration: 2400 of 2400
Iterations per epoch: 200
Maximum iterations: 2400
Validation
Frequency: 25 iterations
Other information
Hardware resource: Single CPU
Learning rate schedule: Constant
Learning rate: 0.001

Fig. 5.6 Training progress, loss, and accuracy versus iterations

The results obtained with and without the application of the bidimensional Fourier transform, for each level, are shown in the Tables 5.5 and 5.6, respectively. They are expressed using the confusion matrix, the accuracy, and the *RMSE* index.

Table 5.5 Confusion Matrix for Levels 1, 2a, 2b, 3, 4, 5 and 6. without FT application

Confusion Matrix – Level 1			
Real Class	**C1: predicted**	**C2: predicted**	**Performance Metrics**
C1	93.3%	6.7%	Accuracy: 92.6%
C2	8.1%	91.9%	RMSE: 24.5%
Confusion Matrix – Level 2a			
Real Class	**C3: predicted**	**C4: predicted**	**Performance Metrics**
C3	98.4%	1.6%	Accuracy:97.3%
C4	3.9%	96.1%	RMSE: 15.7%
Confusion Matrix – Level 2b			
Real Class	**C5: predicted**	**C6: predicted**	**Performance Metrics**
C5	90.9%	9.1%	Accuracy: 90.4%
C6	10.1%	89.9%	RMSE: 17.4%
Confusion Matrix – Level 3			
Real Class	**C7: predicted**	**C8: predicted**	**Performance Metrics**
C7	92.7%	7.3%	Accuracy: 95.9%
C8	0.9%	99.1%	RMSE: 17.4%
Confusion Matrix – Level 4			
Real Class	**C9: predicted**	**C10: predicted**	**Performance Metrics**
C9	94.9%	5.1%	Accuracy: 91.8%
C10	11.3%	88.7%	RMSE: 25.6%
Confusion Matrix – Level 5			
Real Class	**C11: predicted**	**C12: predicted**	**Performance Metrics**
C11	98.8%	1.2%	Accuracy: 98.2%
C12	2.2%	97.8%	RMSE: 5.2%
Confusion Matrix – Level 6			
Real Class	**C13: predicted**	**C14: predicted**	**Performance Metrics**
C13	96.6%	3.4%	Accuracy: 95.3%
C14	5.9%	94.1%	RMSE: 17.1%

Table 5.6 Confusion Matrix for Levels 1, 2a, 2b, 3, 4, 5, and 6 with FT application

Confusion Matrix – Level 1			
Real Class	**C1: predicted**	**C2: predicted**	**Performance Metrics**
C1	87.9%	12.1%	Accuracy: 88%
C2	11.4%	88.6%	RMSE: 31.5%
Confusion Matrix – Level 2a			
Real Class	**C3: predicted**	**C4: predicted**	**Performance Metrics**
C3	79.3%	20.7%	Accuracy: 83.1%
C4	13.0%	87.0%	RMSE: 37.2%
Confusion Matrix – Level 2b			
Real Class	**C5: predicted**	**C6: predicted**	**Performance Metrics**
C5	73.5%	26.5%	Accuracy: 76.3%
C6	20.9%	79.1%	RMSE: 44.3%
Confusion Matrix – Level 3			
Real Class	**C7: predicted**	**C8: predicted**	**Performance Metrics**
C7	97.8%	0.22%	Accuracy: 94.4%
C8	9.0%	91.0%	RMSE: 20.6%
Confusion Matrix – Level 4			
Real Class	**C9: predicted**	**C10: predicted**	**Performance Metrics**
C9	83.9%	16.1%	Accuracy: 85.1%
C10	13.6%	86.4%	RMSE: 38.3%
Confusion Matrix – Level 5			
Real Class	**C11: predicted**	**C12: predicted**	**Performance Metrics**
C11	85.7%	14.3%	Accuracy: 90%
C12	5.9%	94.1%	RMSE: 28.6%
Confusion Matrix – Level 6			
Real Class	**C13: predicted**	**C14: predicted**	**Performance Metrics**
C13	92.4%	7.6%	Accuracy: 91%
C14	11.3%	88.7%	RMSE: 25.8%

The outcomes obtained after the *FT* application on the *GPR* profile showed a decrease in accuracy for all levels with respect to the results obtained without this operation. Whereas the accuracy obtained following the approach without such operation showed values greater than 90% and with an average of 94.5 % , the ones obtained with the trained ResNet-50 on FTs show values greater than 80%, unless level 2b, and with an average of 86.8%. The results shown so far highlight the reliability of the presented methodology, as well as the fact that for such types of images the pre-processing phase with the *FT* likely produces an excessive compression of the data, resulting in a decrease in the obtained accuracy levels.

5.4 In Closing

In this Chaper, a hierarchical multi-level classification approach has been proposed and discussed for tunnel lining assessment. The advantages of using it are as follows:

- the automatic classification of a large number of defects;
- the reduction in time and cost associated with using highly qualified inspectors to evaluate *GPR* patterns;
- the reduction of supplementary invasive tests to be used in conjunction with *GPR* for defect characterisation, resulting in a reduction in diagnostic invasiveness;
- the creation of a methodology that can be incorporated into a holistic maintenance strategy.

Chapter 6

Conclusions

In this thesis, structural monitoring strategies have been developed and tested for control the state of key strategic facilities, such as bridges and tunnels. Such infrastructure, subject to ageing and degradation, requires the development of timely, effective and economically sustainable control methodologies.

Nowadays, several techniques are available to recognize damage in civil engineering structures. Many researches have been developed to identify structural damage in the dynamic field, less so in the static one. Nevertheless, they have been tested to numerical case studies in the majority of cases.

The goal of this thesis has been to design approaches capable of dealing with issues related to specific structural typology, particularly those that are widely spread, attaining a high level of automation, economic resources optimization, and reliability by means of the use of real case studies and numerical simulations to validate them.

After a brief introduction on the state-of-the-art methodologies, this thesis has dedicated one chapter to a customized monitoring system for a highway arch bridge (Chapter 2), one to strategies for simply-supported prestressed concrete railway bridges assessment (Chapter 3), one to control techniques of similar and widely replicated structures such as pedestrian bridges (Chapter 4), and one to methodologies for tunnel lining assessment (Chapter 5).

Specifically, in Chapter 2, methodologies for damage detection in a highway steel arch bridge have been presented. The specific case study, representing a not so common bridge typology in Italy, provided the opportunity to analyze the structural behavior in real-time considering both static and dynamic response. In detail, the monitoring architecture and the acquisition characteristics have allowed for a greater understanding of the impact of several factors, such as data volume and environmental actions, on modal parameters estimation. Furthermore, unsupervised algorithms (K-means) have proven to be a valuable aid in the detection of damage with low severity. Further developments of this work are left for future research efforts.

In Chapter 3, two approaches, designed to be complementary, have been proposed to perform the structural assessment of simply-supported prestressed concrete bridges. The first one has been developed for long-term monitoring and the second one for periodic monitoring on the basis of safety and economic principles due to the large number of such bridges that require control. The first approach investigated the static and environmental data collected on a prestressed railway bridge during its first few years of service. Correlation models have been generated following evaluations of cause-effect relationships between the measured quantities in the healthy condition. Two aspects have been thoroughly examined: the assessment of the midspan strain of the unloaded deck and the evaluation of pier rotations and joint expansion. The strengts of such approach are the selection of features composing the correlation models, the use of pre-processing operations (z-score normalization) to give data repetitiveness over time, the exploitation of some temporal parameters to compensate for the lack of some environmental ones, the selection and the training of specific regression model, and the proposed damage index. The combination of all such factors proved to be extremely effective. The results of the signal analysis and reconstruction approach led to the creation of undamaged-condition alarm thresholds (*UCT*) and successful fault detection, which outperformed traditional thresholds (*DT*) based on design values. In the second part of this Chapter, attention has been paid to the development of a damage identification method focused on the minimization of sensors in the monitoring network, on the reduction of computational time, and on the achievement of high accuracy in localizing damage and estimating its severity. To this aim, a hybrid technique to solve the inverse problem of damage localization and severity estimation in beam structures has been proposed. The influence lines (*ILs*) are used in the first phase of the approach to obtain information about the damage location. Then, by updating a finite-element model, a genetic algorithm (*GA*), which is at the crux of the technique, exploits static parameters such as displacements and rotations at a few locations to estimate the bending stiffness along the structure. The information gathered in the first phase is used in the second one to reduce the number of *GA* design variables and, as a result, the computational time and improve the accuracy of *GA* solutions by allowing a properly trained neural network to select appropriate coefficients for the proposed cost function in the genetic algorithm. The proposed method has been successfully evaluated on a simple supported beam problem using data from a real bridge to assess its effectiveness to actual values, taking into account damage scenarios defined by localized bending stiffness reductions. Besides, numerical experiments have been also conducted to test the procedure when the beam length and geometric properties vary. The obtained outcomes look promising and encourage further developments. Although more effort is needed before real-world applications can be implemented, the proposed strategy is generalizable. Future improvements could entail the use of more refined structural models (grillage), as well as the use of influence surfaces for damage localization, other damage indicators, and the analysis of multiple damage scenarios.

In Chapter 4, the problem of managing a large number of bridges of the same type has been coped by means of Transfer Learning methods. The performance, the potential, and the limitations of such approach have been demonstrated first in a numerical basic supported beam model and then by means of the data recorded on two real pedestrian bridges. The results of these analyses have been very encouraging as they allowed the potential of this method to be effectively investigated and tested and revealed its efficient use for similar and extensively replicated structures, such as pedestrian bridges.

In Chapter 5, the research switched its focus to the assessment of the second most common engineering element in the italian infrastructural assets, namely the tunnels. The proposed hierarchical multi-level damage classification approach, based on the use of the Ground Penetrating Radar (*GPR*), provided several advantages. Among them, the automated classification of several types of defects, the time and cost savings involved with evaluating *GPR* patterns with highly qualified inspectors, the reduction in the number of supplemental invasive tests to be utilized coupled with *GPR* for defect characterization (resulting in less diagnostic invasiveness), and the development of a methodology that can be used as part of a holistic maintenance strategy.

To summarize, as might have been appreciated throughout the reading of the previous Chapters, the focus of this thesis has been directed onto the development of structural health monitoring strategies for the control of large-scale infrastructures. Such strategies have been customized to deal with the issues related to the typology to which the infrastructures belong in order to obtain reliable information about the current structural state and predict its evolution in a sustainable economic way.

References

[1] GWea Housner, Lawrence A Bergman, T Kf Caughey, Anastassios G Chassiakos, Richard O Claus, Sami F Masri, Robert E Skelton, TT Soong, BF Spencer, and James TP Yao. Structural control: past, present, and future. *Journal of engineering mechanics*, 123(9):897–971, 1997.

[2] A Emin Aktan, Daniel N Farhey, David L Brown, Vikram Dalal, Arthur J Helmicki, Victor J Hunt, and Stuart J Shelley. Condition assessment for bridge management. *Journal of Infrastructure Systems*, 2(3):108–117, 1996.

[3] Charles R Farrar and Keith Worden. An introduction to structural health monitoring. *Philosophical Transactions of the Royal Society A: Mathematical, Physical and Engineering Sciences*, 365(1851):303–315, 2007.

[4] Edoardo Cosenza and Gaetano Manfredi. Damage indices and damage measures. *Progress in Structural Engineering and Materials*, 2(1):50–59, 2000.

[5] Dan M Frangopol and James P Curley. Effects of damage and redundancy on structural reliability. *Journal of structural engineering*, 113(7):1533–1549, 1987.

[6] Mohamed Kaouk and David C Zimmerman. Structural damage assessment using a generalized minimum rank perturbation theory. *AIAA journal*, 32(4):836–842, 1994.

[7] David C Zimmerman and Mohammed Kaouk. Structural damage detection using a minimum rank update theory. 1994.

[8] K He and WD Zhu. Structural damage detection using changes in natural frequencies: theory and applications. In *Journal of Physics: Conference Series*, volume 305, page 012054. IOP Publishing, 2011.

[9] F Necati Çatbaş, Tracy Kijewski-Correa, and A Emin Aktan. Structural identification of constructed systems. *Reston (VI): American Society of Civil Engineers*, 2013.

[10] Charles R Farrar and Keith Worden. *Structural health monitoring: a machine learning perspective*. John Wiley & Sons, 2012.

[11] Branislav Kostić and Mustafa Gül. Vibration-based damage detection of bridges under varying temperature effects using time-series analysis and artificial neural networks. *Journal of Bridge Engineering*, 22(10):04017065, 2017.

[12] V Meruane and Ward Heylen. Structural damage assessment under varying temperature conditions. *Structural Health Monitoring*, 11(3):345–357, 2012.

[13] A-M Yan, Gaëtan Kerschen, P De Boe, and J-C Golinval. Structural damage diagnosis under varying environmental conditions—part ii: local pca for non-linear cases. *Mechanical Systems and Signal Processing*, 19(4):865–880, 2005.

[14] WR De Sitter. Costs of service life optimization" the law of fives". In *CEB-RILEM Workshop on Durability of Concrete Structures (Copenhagen, Denmark, May 18-20, 1983)*, pages 131–134. Comité Euro-International du Béton, 1984.

[15] Diego A Tibaduiza Burgos, Ricardo C Gomez Vargas, Cesar Pedraza, David Agis, and Francesc Pozo. Damage identification in structural health monitoring: A brief review from its implementation to the use of data-driven applications. *Sensors*, 20(3):733, 2020.

[16] Limin Sun, Zhiqiang Shang, Ye Xia, Sutanu Bhowmick, and Satish Nagarajaiah. Review of bridge structural health monitoring aided by big data and artificial intelligence: From condition assessment to damage detection. *Journal of Structural Engineering*, 146(5):04020073, 2020.

[17] Wei Fan and Albert Bifet. Mining big data: current status, and forecast to the future. *ACM SIGKDD explorations newsletter*, 14(2):1–5, 2013.

[18] Jonathan Stuart Ward and Adam Barker. Undefined by data: a survey of big data definitions. *arXiv preprint arXiv:1309.5821*, 2013.

[19] Stuart J Russell and Peter Norvig. Artificial intelligence: a modern approach. malaysia, 2016.

[20] Feng-Hsiung Hsu. *Behind Deep Blue: Building the computer that defeated the world chess champion*. Princeton University Press, 2002.

[21] Zoubin Ghahramani. Probabilistic machine learning and artificial intelligence. *Nature*, 521(7553):452–459, 2015.

[22] Miroslav Kubat and Kubat. *An introduction to machine learning*, volume 2. Springer, 2017.

[23] Thomas G Dietterich. Ensemble methods in machine learning. In *International workshop on multiple classifier systems*, pages 1–15. Springer, 2000.

[24] Yuequan Bao and Hui Li. Machine learning paradigm for structural health monitoring. *Structural Health Monitoring*, 20(4):1353–1372, 2021.

[25] Gyungmin Toh and Junhong Park. Review of vibration-based structural health monitoring using deep learning. *Applied Sciences*, 10(5):1680, 2020.

[26] Mohsen Azimi, Armin Dadras Eslamlou, and Gokhan Pekcan. Data-driven structural health monitoring and damage detection through deep learning: State-of-the-art review. *Sensors*, 20(10):2778, 2020.

[27] Majdi Flah, Itzel Nunez, Wassim Ben Chaabene, and Moncef L Nehdi. Machine learning algorithms in civil structural health monitoring: a systematic review. *Archives of computational methods in engineering*, 28(4):2621–2643, 2021.

[28] Samir Khan and Takehisa Yairi. A review on the application of deep learning in system health management. *Mechanical Systems and Signal Processing*, 107:241–265, 2018.

[29] Jian Zhang, Tadanobu Sato, Susumu Iai, and Tara Hutchinson. A pattern recognition technique for structural identification using observed vibration signals: Linear case studies. *Engineering Structures*, 30(5):1439–1446, 2008.

[30] Chang Kook Oh. *Bayesian learning for earthquake engineering applications and structural health monitoring*. California Institute of Technology, 2008.

[31] Behzad Abounia Omran, Qian Chen, and Ruoyu Jin. Comparison of data mining techniques for predicting compressive strength of environmentally friendly concrete. *Journal of Computing in Civil Engineering*, 30(6):04016029, 2016.

[32] S Lee and C Lee. Prediction of shear strength of frp-reinforced concrete flexural members without stirrups using artificial neural networks. *Engineering structures*, 61:99–112, 2014.

[33] Mohammad Hossein Rafiei and Hojjat Adeli. A novel machine learning-based algorithm to detect damage in high-rise building structures. *The Structural Design of Tall and Special Buildings*, 26(18):e1400, 2017.

[34] Hadi Salehi and Rigoberto Burgueño. Emerging artificial intelligence methods in structural engineering. *Engineering structures*, 171:170–189, 2018.

[35] Peter C Chang, Alison Flatau, and Shih-Chii Liu. Health monitoring of civil infrastructure. *Structural health monitoring*, 2(3):257–267, 2003.

[36] SJS Hakim and H Abdul Razak. Modal parameters based structural damage detection using artificial neural networks-a review. *Smart Structures and Systems*, 14(2):159–189, 2014.

[37] Wei Fan and Pizhong Qiao. Vibration-based damage identification methods: a review and comparative study. *Structural health monitoring*, 10(1):83–111, 2011.

[38] Swagato Das, P Saha, and SK Patro. Vibration-based damage detection techniques used for health monitoring of structures: a review. *Journal of Civil Structural Health Monitoring*, 6(3):477–507, 2016.

[39] Scott W Doebling, Charles R Farrar, Michael B Prime, and Daniel W Shevitz. Damage identification and health monitoring of structural and mechanical systems from changes in their vibration characteristics: a literature review. 1996.

[40] A Alvandi and C Cremona. Assessment of vibration-based damage identification techniques. *Journal of sound and vibration*, 292(1-2):179–202, 2006.

[41] Brian J Schwarz and Mark H Richardson. Experimental modal analysis. *CSI Reliability week*, 35(1):1–12, 1999.

[42] Loris Vincenzi. Identificazione dinamica delle caratteristiche modali e delle proprietà meccaniche di strutture mediante algoritmi di ottimizzazione. 2007.

[43] Carlo Rainieri and Giovanni Fabbrocino. Automated output-only dynamic identification of civil engineering structures. *Mechanical Systems and Signal Processing*, 24(3):678–695, 2010.

[44] Riccardo Mario Azzara, Anna De Falco, Maria Girardi, and Daniele Pellegrini. Ambient vibration recording on the maddalena bridge in borgo a mozzano (italy): data analysis. *Annals of Geophysics*, 2017.

[45] Ivan Roselli, Marialaura Malena, Marialuisa Mongelli, Nicola Cavalagli, Massimiliano Gioffrè, Gerardo De Canio, and Gianmarco de Felice. Health assessment and ambient vibration testing of the "ponte delle torri" of spoleto during the 2016–2017 central italy seismic sequence. *Journal of Civil Structural Health Monitoring*, 8(2):199–216, 2018.

[46] Bernardino Chiaia, Giulia Marasco, Giulio Ventura, and Cristina Zannini Quirini. Customised active monitoring system for structural control and maintenance optimisation. *Journal of Civil Structural Health Monitoring*, 10(2):267–282, 2020.

[47] OS Salawu. Detection of structural damage through changes in frequency: a review. *Engineering structures*, 19(9):718–723, 1997.

[48] Guang-Dong Zhou and Ting-Hua Yi. A summary review of correlations between temperatures and vibration properties of long-span bridges. *Mathematical Problems in Engineering*, 2014, 2014.

[49] Randall J Allemang. The modal assurance criterion–twenty years of use and abuse. *Sound and vibration*, 37(8):14–23, 2003.

[50] John J Moughty and Joan R Casas. A state of the art review of modal-based damage detection in bridges: Development, challenges, and solutions. *Applied Sciences*, 7(5):510, 2017.

[51] RO Curadelli, JD Riera, D Ambrosini, and MG Amani. Damage detection by means of structural damping identification. *Engineering Structures*, 30(12):3497–3504, 2008.

[52] E Peter Carden and Paul Fanning. Vibration based condition monitoring: a review. *Structural health monitoring*, 3(4):355–377, 2004.

[53] Edwin Reynders, Rik Pintelon, and Guido De Roeck. Uncertainty bounds on modal parameters obtained from stochastic subspace identification. *Mechanical systems and signal processing*, 22(4):948–969, 2008.

[54] Chengke Wu, Peng Wu, Jun Wang, Rui Jiang, Mengcheng Chen, and Xiangyu Wang. Critical review of data-driven decision-making in bridge operation and maintenance. *Structure and Infrastructure Engineering*, 18(1):47–70, 2021.

[55] Viet Ha Nguyen, Sebastian Schommer, Stefan Maas, and Arno Zürbes. Static load testing with temperature compensation for structural health monitoring of bridges. *Engineering Structures*, 127:700–718, 2016.

[56] Masoud Sanayei, John E Phelps, Jesse D Sipple, Erin S Bell, and Brian R Brenner. Instrumentation, nondestructive testing, and finite-element model updating for bridge evaluation using strain measurements. *Journal of bridge engineering*, 17(1):130–138, 2012.

[57] Bernard Tonnoir, Christophe Carde, and David Banant. Curvature: An indicator of the mechanical condition of old prestressed concrete bridges. *Structural Engineering International*, 28(3):357–361, 2018.

[58] Jung-Huai Chou and Jamshid Ghaboussi. Genetic algorithm in structural damage detection. *Computers & structures*, 79(14):1335–1353, 2001.

[59] CH Jenkins, L Kjerengtroen, and H Oestensen. Sensitivity of parameter changes in structural damage detection. *Shock and Vibration*, 4(1):27–37, 1997.

[60] Christopher Nonis, Christopher Niezrecki, Tzu-Yang Yu, Shafique Ahmed, Che-Fu Su, and Tim Schmidt. Structural health monitoring of bridges using digital image correlation. In *Health monitoring of structural and biological systems 2013*, volume 8695, pages 51–63. SPIE, 2013.

[61] Christopher Niezrecki, Javad Baqersad, and Alessandro Sabato. Digital image correlation techniques for non-destructive evaluation and structural health monitoring. *Handbook of Advanced Non-Destructive Evaluation*, page 46, 2018.

[62] Daniel Reagan, Alessandro Sabato, and Christopher Niezrecki. Feasibility of using digital image correlation for unmanned aerial vehicle structural health monitoring of bridges. *Structural Health Monitoring*, 17(5):1056–1072, 2018.

[63] Daniel Reagan, Alessandro Sabato, and Christopher Niezrecki. Unmanned aerial vehicle acquisition of three-dimensional digital image correlation measurements for structural health monitoring of bridges. In *Nondestructive Characterization and Monitoring of Advanced Materials, Aerospace, and Civil Infrastructure 2017*, volume 10169, pages 68–77. SPIE, 2017.

[64] Amedeo Manuello Bertetto, Davide Masera, and Alberto Carpinteri. Acoustic emission monitoring of the turin cathedral bell tower: Foreshock and aftershock discrimination. *Applied Sciences*, 10(11):3931, 2020.

[65] Amedeo Manuello, Gianni Niccolini, and Alberto Carpinteri. Ae monitoring of a concrete arch road tunnel: Damage evolution and localization. *Engineering Fracture Mechanics*, 210:279–287, 2019.

[66] Huangda Zhu, Feng Liu, Jiawei Cui, and Wangbin Peng. Research on tunnel damage process based on acoustic emission technology. In *Journal of Physics: Conference Series*, volume 2196, page 012001. IOP Publishing, 2022.

[67] Daniel Tonelli, Michele Luchetta, Francesco Rossi, Placido Migliorino, and Daniele Zonta. Structural health monitoring based on acoustic emissions: Validation on a prestressed concrete bridge tested to failure. *Sensors*, 20(24):7272, 2020.

[68] Amir M Alani and Fabio Tosti. Gpr applications in structural detailing of a major tunnel using different frequency antenna systems. *Construction and Building Materials*, 158:1111–1122, 2018.

[69] Thikra Dawood, Zhenhua Zhu, and Tarek Zayed. Deterioration mapping in subway infrastructure using sensory data of gpr. *Tunnelling and Underground Space Technology*, 103:103487, 2020.

[70] Deshan Feng, Xun Wang, and Bin Zhang. Specific evaluation of tunnel lining multi-defects by all-refined gpr simulation method using hybrid algorithm of fetd and fdtd. *Construction and Building Materials*, 185:220–229, 2018.

[71] W Al-Nuaimy, Y Huang, M Nakhkash, MTC Fang, VT Nguyen, and A Eriksen. Automatic detection of buried utilities and solid objects with gpr using neural networks and pattern recognition. *Journal of applied Geophysics*, 43(2-4):157–165, 2000.

[72] M Mahalakshmi, P Kalaivani, and E Kiruba Nesamalar. A review on genetic algorithm and its applications. *International Journal of Computing Algorithm*, 2(2):415–423, 2013.

[73] Seyedali Mirjalili, Jin Song Dong, Ali Safa Sadiq, and Hossam Faris. Genetic algorithm: Theory, literature review, and application in image reconstruction. *Nature-inspired optimizers*, pages 69–85, 2020.

[74] Agoston E Eiben and Selmar K Smit. Parameter tuning for configuring and analyzing evolutionary algorithms. *Swarm and Evolutionary Computation*, 1(1):19–31, 2011.

[75] FTK Au, YS Cheng, LG Tham, and ZZ Bai. Structural damage detection based on a micro-genetic algorithm using incomplete and noisy modal test data. *Journal of Sound and Vibration*, 259(5):1081–1094, 2003.

[76] Hong Hao and Yong Xia. Vibration-based damage detection of structures by genetic algorithm. *Journal of computing in civil engineering*, 16(3):222–229, 2002.

[77] V Meruane and W Heylen. An hybrid real genetic algorithm to detect structural damage using modal properties. *Mechanical systems and signal processing*, 25(5):1559–1573, 2011.

[78] Mehdi Nobahari and Seyed Mohammad Seyedpoor. Structural damage detection using an efficient correlation-based index and a modified genetic algorithm. *Mathematical and Computer modelling*, 53(9-10):1798–1809, 2011.

[79] Dae-Sung Jung and Chul-Young Kim. Finite element model updating of a simply supported skewed psc i-girder bridge using hybrid genetic algorithm. *KSCE Journal of Civil Engineering*, 17(3):518–529, 2013.

[80] Rong-Song He and Shun-Fa Hwang. Damage detection by an adaptive real-parameter simulated annealing genetic algorithm. *Computers & Structures*, 84(31-32):2231–2243, 2006.

[81] Rong-Song He and Shun-Fa Hwang. Damage detection by a hybrid real-parameter genetic algorithm under the assistance of grey relation analysis. *Engineering Applications of Artificial Intelligence*, 20(7):980–992, 2007.

[82] Keith Worden and Graeme Manson. The application of machine learning to structural health monitoring. *Philosophical Transactions of the Royal Society A: Mathematical, Physical and Engineering Sciences*, 365(1851):515–537, 2007.

[83] Jiawei Han, Jian Pei, and Micheline Kamber. *Data mining: concepts and techniques*. Elsevier, 2011.

[84] Jong-Woong Park, Kyoung-Chan Lee, Sung-Han Sim, Hyung-Jo Jung, and Billie F Spencer Jr. Traffic safety evaluation for railway bridges using expanded multisensor data fusion. *Computer-Aided Civil and Infrastructure Engineering*, 31(10):749–760, 2016.

[85] Yan Xu, James Mark William Brownjohn, David Hester, and Ki Young Koo. Long-span bridges: Enhanced data fusion of gps displacement and deck accelerations. *Engineering Structures*, 147:639–651, 2017.

[86] Pedro Domingos. A few useful things to know about machine learning. *Communications of the ACM*, 55(10):78–87, 2012.

[87] David JC MacKay, David JC Mac Kay, et al. *Information theory, inference and learning algorithms*. Cambridge university press, 2003.

[88] Gholamreza Ghodrati Amiri and Ehsan Darvishan. Damage detection of moment frames using ensemble empirical mode decomposition and clustering techniques. *KSCE Journal of Civil Engineering*, 19(5):1302–1311, 2015.

[89] Ling Yu, Jun-hua Zhu, and Li-li Yu. Structural damage detection in a truss bridge model using fuzzy clustering and measured frf data reduced by principal component projection. *Advances in Structural Engineering*, 16(1):207–217, 2013.

[90] James Manyika, Michael Chui, Brad Brown, Jacques Bughin, Richard Dobbs, Charles Roxburgh, Angela Hung Byers, et al. *Big data: The next frontier for innovation, competition, and productivity*. McKinsey Global Institute, 2011.

[91] Waseem Rawat and Zenghui Wang. Deep convolutional neural networks for image classification: A comprehensive review. *Neural computation*, 29(9):2352–2449, 2017.

[92] Byunghyun Kim and Soojin Cho. Automated vision-based detection of cracks on concrete surfaces using a deep learning technique. *Sensors*, 18(10):3452, 2018.

[93] Jinsong Zhu and Jinbo Song. An intelligent classification model for surface defects on cement concrete bridges. *Applied Sciences*, 10(3):972, 2020.

[94] Chuncheng Feng, Hua Zhang, Shuang Wang, Yonglong Li, Haoran Wang, and Fei Yan. Structural damage detection using deep convolutional neural network and transfer learning. *KSCE Journal of Civil Engineering*, 23(10):4493–4502, 2019.

[95] Qing Song, Yingqi Wu, Xueshi Xin, Lu Yang, Min Yang, Hongming Chen, Chun Liu, Mengjie Hu, Xuesong Chai, and Jianchao Li. Real-time tunnel crack analysis system via deep learning. *Ieee Access*, 7:64186–64197, 2019.

[96] B Patterson, G Leone, Maria Pantoja, and Anahid A Behrouzi. Deep learning for automated image classification of seismic damage to built infrastructure. In *Eleventh US National Conference on Earthquake Engineering*, 2018.

[97] Young-Jin Cha, Wooram Choi, Gahyun Suh, Sadegh Mahmoudkhani, and Oral Büyüköztürk. Autonomous structural visual inspection using region-based deep learning for detecting multiple damage types. *Computer-Aided Civil and Infrastructure Engineering*, 33(9):731–747, 2018.

[98] YouLiang Ding and AiQun Li. Temperature-induced variations of measured modal frequencies of steel box girder for a long-span suspension bridge. *International Journal of Steel Structures*, 11(2):145–155, 2011.

[99] Gabriele Comanducci, Filipe Magalhães, Filippo Ubertini, and Álvaro Cunha. On vibration-based damage detection by multivariate statistical techniques: Application to a long-span arch bridge. *Structural health monitoring*, 15(5):505–524, 2016.

[100] Shanwu Li, Shujin Laima, and Hui Li. Data-driven modeling of vortex-induced vibration of a long-span suspension bridge using decision tree learning and support vector regression. *Journal of Wind Engineering and Industrial Aerodynamics*, 172:196–211, 2018.

[101] XG Hua, YQ Ni, JM Ko, and KY Wong. Modeling of temperature–frequency correlation using combined principal component analysis and support vector regression technique. *Journal of Computing in Civil Engineering*, 21(2):122–135, 2007.

[102] Peter Moser and Babak Moaveni. Environmental effects on the identified natural frequencies of the dowling hall footbridge. *Mechanical Systems and Signal Processing*, 25(7):2336–2357, 2011.

[103] Navid Zolghadri, Marvin W Halling, and Paul J Barr. Effects of temperature variations on structural vibration properties. In *Geotechnical and Structural Engineering Congress 2016*, pages 1032–1043, 2016.

[104] David H Wolpert. The supervised learning no-free-lunch theorems. *Soft computing and industry*, pages 25–42, 2002.

[105] Milad Fallahian, Faramarz Khoshnoudian, and Viviana Meruane. Ensemble classification method for structural damage assessment under varying temperature. *Structural Health Monitoring*, 17(4):747–762, 2018.

[106] Zhuorong Li, Junqi Guo, Wenshuang Liang, Xiaobo Xie, Guangzhi Zhang, and Shenling Wang. Structural health monitoring based on realadaboost algorithm in wireless sensor networks. In *International Conference on Wireless Algorithms, Systems, and Applications*, pages 236–245. Springer, 2014.

[107] Zhe Li and Rigoberto Burgueño. Using soft computing to analyze inspection results for bridge evaluation and management. *Journal of Bridge Engineering*, 15(4):430–438, 2010.

[108] Irwanda Laory, Thanh N Trinh, Ian FC Smith, and James MW Brownjohn. Methodologies for predicting natural frequency variation of a suspension bridge. *Engineering Structures*, 80:211–221, 2014.

[109] Ding Huang, Deying Hu, Jingwu He, and Yuexi Xiong. Structure damage detection based on ensemble learning. In *2018 9th International Conference on Mechanical and Aerospace Engineering (ICMAE)*, pages 219–224. IEEE, 2018.

[110] Alberto Diez, Nguyen Lu Dang Khoa, Mehrisadat Makki Alamdari, Yang Wang, Fang Chen, and Peter Runcie. A clustering approach for structural health monitoring on bridges. *Journal of Civil Structural Health Monitoring*, 6(3):429–445, 2016.

[111] Gabriel Michau, Thomas Palmé, and Olga Fink. Fleet phm for critical systems: bi-level deep learning approach for fault detection. In *Proceedings of the European Conference of the PHM Society 2018*, volume 4, page 403. PHM Society, 2018.

[112] Qin Wang, Gabriel Michau, and Olga Fink. Domain adaptive transfer learning for fault diagnosis. In *2019 Prognostics and System Health Management Conference (PHM-Paris)*, pages 279–285. IEEE, 2019.

[113] Gabriel Michau and Olga Fink. Unsupervised fault detection in varying operating conditions. In *2019 IEEE International Conference on Prognostics and Health Management (ICPHM)*, pages 1–10. IEEE, 2019.

[114] Gabriel Michau, Yang Hu, Thomas Palmé, and Olga Fink. Feature learning for fault detection in high-dimensional condition monitoring signals. *Proceedings of the Institution of Mechanical Engineers, Part O: Journal of Risk and Reliability*, 234(1):104–115, 2020.

[115] Theanh Nguyen, Tommy HT Chan, and David P Thambiratnam. Controlled monte carlo data generation for statistical damage identification employing mahalanobis squared distance. *Structural Health Monitoring*, 13(4):461–472, 2014.

[116] Eloi Figueiredo and Elizabeth Cross. Linear approaches to modeling nonlinearities in long-term monitoring of bridges. *Journal of Civil Structural Health Monitoring*, 3(3):187–194, 2013.

[117] Marek Słoński. Gaussian mixture model for time series-based structural damage detection. *Computer Assisted Methods in Engineering and Science*, 19(4):331–338, 2017.

[118] Chang Kook Oh, Hoon Sohn, and In-Hwan Bae. Statistical novelty detection within the yeongjong suspension bridge under environmental and operational variations. *Smart materials and structures*, 18(12):125022, 2009.

[119] Ting-Hua Yi, Hong-Nan Li, Gangbing Song, and Qing Guo. Detection of shifts in gps measurements for a long-span bridge using cusum chart. *International Journal of Structural Stability and Dynamics*, 16(04):1640024, 2016.

[120] Yuan-Feng Duan, Yi Li, and Yi-Qiang Xiang. Strain-temperature correlation analysis of a tied arch bridge using monitoring data. In *2011 International Conference on Multimedia Technology*, pages 6025–6028. IEEE, 2011.

[121] Ana C Neves, Ignacio Gonzalez, John Leander, and Raid Karoumi. Structural health monitoring of bridges: a model-free ann-based approach to damage detection. *Journal of Civil Structural Health Monitoring*, 7(5):689–702, 2017.

[122] Irwanda Laory, Thanh N Trinh, Daniele Posenato, and Ian FC Smith. Combined model-free data-interpretation methodologies for damage detection during continuous monitoring of structures. *Journal of Computing in Civil Engineering*, 27(6):657–666, 2013.

[123] N Dervilis, K Worden, and EJ Cross. On robust regression analysis as a means of exploring environmental and operational conditions for shm data. *Journal of Sound and Vibration*, 347:279–296, 2015.

[124] Moisés Silva, Adam Santos, Eloi Figueiredo, Reginaldo Santos, Claudomiro Sales, and João CWA Costa. A novel unsupervised approach based on a genetic algorithm for structural damage detection in bridges. *Engineering Applications of Artificial Intelligence*, 52:168–180, 2016.

[125] Young-Jin Cha and Zilong Wang. Unsupervised novelty detection–based structural damage localization using a density peaks-based fast clustering algorithm. *Structural Health Monitoring*, 17(2):313–324, 2018.

[126] Sina Mehdinia, Younes Hamishebaharb, Maryam Bitarafc, Amir Kayvan, and Mohammad Rahimiane Ghorbani-Tanhad. Structural damage detection using k-means clus-tering algorithm under unknown environmental and operational conditions.

[127] Abd Ennour Bouzenad, Mahjoub El Mountassir, Slah Yaacoubi, Fethi Dahmene, Mahmoud Koabaz, Lilian Buchheit, Weina Ke, et al. A semi-supervised based k-means algorithm for optimal guided waves structural health monitoring: A case study. *Inventions*, 4(1):17, 2019.

[128] Robert C Tryon. Cluster analysis: correlation profile and orthometric analysis for the isolation of unities in mind and personality. *Ann Arbor: Edward Brothers*, 1939.

[129] P Gardner, X Liu, and K Worden. On the application of domain adaptation in structural health monitoring. *Mechanical Systems and Signal Processing*, 138:106550, 2020.

[130] LA Bull, PA Gardner, J Gosliga, TJ Rogers, N Dervilis, EJ Cross, E Papatheou, AE Maguire, C Campos, and K Worden. Foundations of population-based shm, part i: homogeneous populations and forms. *Mechanical Systems and Signal Processing*, 148:107141, 2021.

[131] P Gardner, LA Bull, J Gosliga, N Dervilis, and K Worden. Foundations of population-based shm, part iii: heterogeneous populations–mapping and transfer. *Mechanical Systems and Signal Processing*, 149:107142, 2021.

[132] J Gosliga, PA Gardner, LA Bull, N Dervilis, and K Worden. Foundations of population-based shm, part ii: Heterogeneous populations–graphs, networks, and communities. *Mechanical Systems and Signal Processing*, 148:107144, 2021.

[133] Sinno Jialin Pan and Qiang Yang. A survey on transfer learning. *IEEE Transactions on knowledge and data engineering*, 22(10):1345–1359, 2009.

[134] Ali Ozdagli and Xenofon Koutsoukos. Domain adaptation for structural health monitoring. In *Annual Conference of the PHM Society*, volume 12, pages 9–9, 2020.

[135] Samuel da Silva, Marcus Omori Yano, and Camila Gianini Gonsalez-Bueno. Transfer component analysis for compensation of temperature effects on the impedance-based structural health monitoring. *Journal of Nondestructive Evaluation*, 40(3):1–17, 2021.

[136] LA Bull, PA Gardner, N Dervilis, E Papatheou, M Haywood-Alexander, RS Mills, and K Worden. On the transfer of damage detectors between structures: an experimental case study. *Journal of Sound and Vibration*, 501:116072, 2021.

[137] Zhongqiu Fu, Bohai Ji, Qiudong Wang, and Yixun Wang. Cable force calculation using vibration frequency methods based on cable geometric parameters. *Journal of Performance of Constructed Facilities*, 31(4):04017021, 2017.

[138] Zhongxiang Liu, Tong Guo, Matthew H Hebdon, and Zhaolei Zhang. Corrosion fatigue analysis and reliability assessment of short suspenders in suspension and arch bridges. *Journal of Performance of Constructed Facilities*, 32(5):04018060, 2018.

[139] XU Jun, Chen Weizhen, and LIU Xue. Deterioration mechanism of cables and mechanics model of wires. *JOURNAL OF TONGJI UNIVERSITY NATURAL SCIENCE*, 7, 2008.

[140] Y Kondo. Prediction of fatigue crack initiation life based on pit growth. *Corrosion*, 45(1):7–11, 1989.

[141] Carlo Pellegrino, Giovanni Cupani, and Claudio Modena. The effect of fatigue on the arrangement of hangers in tied arch bridges. *Engineering Structures*, 32(4):1140–1147, 2010.

[142] Raimondo Betti and Bojidar Yanev. Conditions of suspension bridge cables: New york city case study. *Transportation research record*, 1654(1):105–112, 1999.

[143] Scott Calabrese Barton, Garry W Vermaas, Paul F Duby, Alan C West, and Raimondo Betti. Accelerated corrosion and embrittlement of high-strength bridge wire. *Journal of materials in civil engineering*, 12(1):33–38, 2000.

[144] Xu Jun, Li Jia, and Li Jie. Arch suspender dynamic response analysis based on support spring model. In *2014 7th International Conference on Intelligent Computation Technology and Automation*, pages 916–919. IEEE, 2014.

[145] Dongming Feng and Maria Q Feng. Identification of structural stiffness and excitation forces in time domain using noncontact vision-based displacement measurement. *Journal of Sound and Vibration*, 406:15–28, 2017.

[146] F Necati Catbas and A Emin Aktan. Condition and damage assessment: issues and some promising indices. *Journal of Structural Engineering*, 128(8):1026–1036, 2002.

[147] Bart Peeters and Guido De Roeck. Reference-based stochastic subspace identification for output-only modal analysis. *Mechanical systems and signal processing*, 13(6):855–878, 1999.

[148] P Andersen. Artemis extractor online help. *Structural Vibration Solutions A/S*, 2010.

[149] Carlo Rainieri and Giovanni Fabbrocino. Operational modal analysis of civil engineering structures. *Springer, New York*, 142:143, 2014.

[150] Peter Van Overschee and BL De Moor. *Subspace identification for linear systems: Theory—Implementation—Applications*. Springer Science & Business Media, 2012.

[151] B Peeters, G De Roeck, T Pollet, and L Schueremans. Stochastic subspace techniques applied to parameter identification of civil engineering structures. *New Advances in Modal Synthesis of Large Structure*, pages 145–156, 1997.

[152] Carlo Rainieri and Giovanni Fabbrocino. Influence of model order and number of block rows on accuracy and precision of modal parameter estimates in stochastic subspace identification. *International Journal of Lifecycle Performance Engineering 10*, 1(4):317–334, 2014.

[153] Wen-Hwa Wu, Sheng-Wei Wang, Chien-Chou Chen, and Gwolong Lai. Modal parameter identification for closely spaced modes of civil structures based on an upgraded stochastic subspace methodology. *Structure and Infrastructure Engineering*, 15(3):296–313, 2019.

[154] Edwin Reynders and Guido De Roeck. Reference-based combined deterministic–stochastic subspace identification for experimental and operational modal analysis. *Mechanical Systems and Signal Processing*, 22(3):617–637, 2008.

[155] C Priori, M De Angelis, and R Betti. On the selection of user-defined parameters in data-driven stochastic subspace identification. *Mechanical Systems and Signal Processing*, 100:501–523, 2018.

[156] Filipe Magalhaes, Alvaro Cunha, and Elsa Caetano. Online automatic identification of the modal parameters of a long span arch bridge. *Mechanical Systems and Signal Processing*, 23(2):316–329, 2009.

[157] Bart Peeters. System identification and damage detection in civil engeneering. 2000.

[158] Rune Brincker, Lingmi Zhang, Palle Andersen, et al. Modal identification from ambient responses using frequency domain decomposition. In *Proceedings of the 18th international modal analysis conference (IMAC)*, volume 1, pages 625–630. San Antonio, TX, USA, 2000.

[159] Filipe Magalhães, Álvaro Cunha, Elsa Caetano, and Rune Brincker. Damping estimation using free decays and ambient vibration tests. *Mechanical Systems and Signal Processing*, 24(5):1274–1290, 2010.

[160] Brad A Pridham and John C Wilson. A study of damping errors in correlation-driven stochastic realizations using short data sets. *Probabilistic engineering mechanics*, 18(1):61–77, 2003.

[161] Bart Peeters and Guido De Roeck. One-year monitoring of the z24-bridge: environmental effects versus damage events. *Earthquake engineering & structural dynamics*, 30(2):149–171, 2001.

[162] Hoon Sohn. Effects of environmental and operational variability on structural health monitoring. *Philosophical Transactions of the Royal Society A: Mathematical, Physical and Engineering Sciences*, 365(1851):539–560, 2007.

[163] Yinghong Cao, Jinsuk Yim, Yang Zhao, and Ming L Wang. Temperature effects on cable stayed bridge using health monitoring system: a case study. *Structural Health Monitoring*, 10(5):523–537, 2011.

[164] YQ Ni, XG Hua, KQ Fan, and JM Ko. Correlating modal properties with temperature using long-term monitoring data and support vector machine technique. *Engineering Structures*, 27(12):1762–1773, 2005.

[165] Arnaud Deraemaeker, Edwin Reynders, Guido De Roeck, and Jyrki Kullaa. Vibration-based structural health monitoring using output-only measurements under changing environment. *Mechanical systems and signal processing*, 22(1):34–56, 2008.

[166] JM Ko and Yi Qing Ni. Technology developments in structural health monitoring of large-scale bridges. *Engineering structures*, 27(12):1715–1725, 2005.

[167] Johan Maeck, B Peeters, and Guido De Roeck. Damage identification on the z24-bridge using vibration monitoring analysis. In *COST F3 conference on system identification and structural health monitoring*, pages 233–242, 2000.

[168] Bart Peeters, Johan Maeck, and Guido De Roeck. Vibration-based damage detection in civil engineering: excitation sources and temperature effects. *Smart materials and Structures*, 10(3):518, 2001.

[169] Hui Li, Shunlong Li, Jinping Ou, and Hongwei Li. Modal identification of bridges under varying environmental conditions: temperature and wind effects. *Structural Control and Health Monitoring*, 17(5):495–512, 2010.

[170] Filipe Magalhães, Álvaro Cunha, and Elsa Caetano. Vibration based structural health monitoring of an arch bridge: from automated oma to damage detection. *Mechanical Systems and Signal Processing*, 28:212–228, 2012.

[171] Michele Dilena and Antonino Morassi. Dynamic testing of a damaged bridge. *Mechanical Systems and Signal Processing*, 25(5):1485–1507, 2011.

[172] Kai-Chun Chang and Chul-Woo Kim. Modal-parameter identification and vibration-based damage detection of a damaged steel truss bridge. *Engineering Structures*, 122:156–173, 2016.

[173] Stuart Lloyd. Least squares quantization in pcm. *IEEE transactions on information theory*, 28(2):129–137, 1982.

[174] David Arthur and Sergei Vassilvitskii. k-means++: The advantages of careful seeding. Technical report, Stanford, 2006.

[175] Ismail Bin Mohamad and Dauda Usman. Standardization and its effects on k-means clustering algorithm. *Research Journal of Applied Sciences, Engineering and Technology*, 6(17):3299–3303, 2013.

[176] Mehrisadat Makki Alamdari, Thierry Rakotoarivelo, and Nguyen Lu Dang Khoa. A spectral-based clustering for structural health monitoring of the sydney harbour bridge. *Mechanical Systems and Signal Processing*, 87:384–400, 2017.

[177] Tadeusz Caliński and Jerzy Harabasz. A dendrite method for cluster analysis. *Communications in Statistics-theory and Methods*, 3(1):1–27, 1974.

[178] Peter J Rousseeuw. Silhouettes: a graphical aid to the interpretation and validation of cluster analysis. *Journal of computational and applied mathematics*, 20:53–65, 1987.

[179] David L Davies and Donald W Bouldin. A cluster separation measure. *IEEE transactions on pattern analysis and machine intelligence*, (2):224–227, 1979.

[180] Robert Tibshirani, Guenther Walther, and Trevor Hastie. Estimating the number of clusters in a data set via the gap statistic. *Journal of the Royal Statistical Society: Series B (Statistical Methodology)*, 63(2):411–423, 2001.

[181] Houbiao Ma, Yang Yang, Zheng He, Yahui Zhang, and Fei Ji. Experimental study on mechanical properties of steel under extreme cyclic loading considering pitting damage. *Ocean engineering*, 186:106091, 2019.

[182] Krzysztof Woloszyk and Yordan Garbatov. Random field modelling of mechanical behaviour of corroded thin steel plate specimens. *Engineering Structures*, 212:110544, 2020.

[183] M Maksymowicz, Paulo JS Cruz, J Bień, and Rosemarie Helmerich. Concrete railway bridges: Taxonomy of degradation mechanisms and damages identified by ndt methods. 2006.

[184] J Bień, K Jakubowski, T Kamiński, J Kmita, P Kmita, Paulo JS Cruz, and M Maksymowicz. Railway bridge defects and degradation mechanisms. 2007.

[185] Luca Sgambi, Pier Giorgio Malerba, Giordano Gotti, and Diego Ielmini. The influence of degradation phenomena on collapse modes in prestressed concrete beams. *International Journal of Lifecycle Performance Engineering*, 1(1):41–63, 2012.

[186] Zenonas Kamaitis and Z Kamaitis. The causes of shear cracking in prestressed concrete box-girder bridges. *Statyba*, 2(8):26–34, 1996.

[187] Monica Arul and Ahsan Kareem. Data anomaly detection for structural health monitoring of bridges using shapelet transform. *arXiv preprint arXiv:2009.00470*, 2020.

[188] Gaoyang Liu, Yanbo Niu, Weijian Zhao, Yuanfeng Duan, and Jiangpeng Shu. Data anomaly detection for structural health monitoring using a combination network of ganomaly and cnn. 2022.

[189] Zhiyi Tang, Zhicheng Chen, Yuequan Bao, and Hui Li. Convolutional neural network-based data anomaly detection method using multiple information for structural health monitoring. *Structural Control and Health Monitoring*, 26(1):e2296, 2019.

[190] AJ Cardini and John T DeWolf. Long-term structural health monitoring of a multi-girder steel composite bridge using strain data. *Structural Health Monitoring*, 8(1):47–58, 2009.

[191] Yuequan Bao, Zhicheng Chen, Shiyin Wei, Yang Xu, Zhiyi Tang, and Hui Li. The state of the art of data science and engineering in structural health monitoring. *Engineering*, 5(2):234–242, 2019.

[192] You-Liang Ding, Gao-Xin Wang, Peng Sun, Lai-Yi Wu, and Qing Yue. Long-term structural health monitoring system for a high-speed railway bridge structure. *The Scientific World Journal*, 2015, 2015.

[193] Sameer Al-Dahidi, Piero Baraldi, Francesco Di Maio, and Enrico Zio. Quantification of signal reconstruction uncertainty in fault detection systems. In *PHM Society European Conference*, volume 2, 2014.

[194] Ruey S Tsay. *Analysis of financial time series*. John wiley & sons, 2005.

[195] James L McClelland, David E Rumelhart, and Geoffrey E Hinton. The appeal of parallel distributed processing. *MIT Press, Cambridge MA*, pages 3–44, 1986.

[196] Tong Guo, Richard Sause, Dan M Frangopol, and Aiqun Li. Time-dependent reliability of psc box-girder bridge considering creep, shrinkage, and corrosion. *Journal of Bridge Engineering*, 16(1):29–43, 2011.

[197] Shiwei Li, Yongqing Yang, Qianhui Pu, Deng Yang, Baolin Sun, and Xiaobin Li. Three-dimensional nonlinear creep and shrinkage effects of a long-span prestressed concrete box girder bridge. *Structural Concrete*, 20(2):638–649, 2019.

[198] Roberto Liverani. *Analisi delle deformazioni di un ponte a travata continua in cemento armato*. PhD thesis.

[199] Tianqi Chen and Carlos Guestrin. Xgboost: A scalable tree boosting system. In *Proceedings of the 22nd acm sigkdd international conference on knowledge discovery and data mining*, pages 785–794, 2016.

[200] Zhi-Wei Chen, Long Zhao, Jian Zhang, Qin-Lin Cai, Jun Li, and Songye Zhu. Damage quantification of beam structures using deflection influence line changes and sparse regularization. *Advances in Structural Engineering*, 24(9):1997–2010, 2021.

[201] ZhiWei Chen, QinLin Cai, Ying Lei, and SongYe Zhu. Damage detection of long-span bridges using stress influence lines incorporated control charts. *Science China Technological Sciences*, 57(9):1689–1697, 2014.

[202] Ivana Štimac, Ante Mihanović, and Ivica Kožar. „damage detection from analysis of displacement influence lines “. In *International Conference on Bridges, Dubrovnik*, pages 1001–1008, 2006.

[203] Thomas Henry Gordon Megson. *Structural and stress analysis*. Butterworth-Heinemann, 2019.

[204] Ahmad Hassanat, Khalid Almohammadi, Esra' Alkafaween, Eman Abunawas, Awni Hammouri, and VB Prasath. Choosing mutation and crossover ratios for genetic algorithms—a review with a new dynamic approach. *Information*, 10(12):390, 2019.

[205] Fabrício José Pontes, GF Amorim, Pedro Paulo Balestrassi, AP Paiva, and João Roberto Ferreira. Design of experiments and focused grid search for neural network parameter optimization. *Neurocomputing*, 186:22–34, 2016.

[206] Muhammad Murtadha Ramadhan, Imas Sukaesih Sitanggang, Fahrendi Rizky Nasution, and Abdullah Ghifari. Parameter tuning in random forest based on grid search method for gender classification based on voice frequency. *DEStech Transactions on Computer Science and Engineering*, 10, 2017.

[207] BH Shekar and Guesh Dagnew. Grid search-based hyperparameter tuning and classification of microarray cancer data. In *2019 second international conference on advanced computational and communication paradigms (ICACCP)*, pages 1–8. IEEE, 2019.

[208] Oludare Isaac Abiodun, Aman Jantan, Abiodun Esther Omolara, Kemi Victoria Dada, Nachaat AbdElatif Mohamed, and Humaira Arshad. State-of-the-art in artificial neural network applications: A survey. *Heliyon*, 4(11):e00938, 2018.

[209] James Bergstra and Yoshua Bengio. Random search for hyper-parameter optimization. *Journal of machine learning research*, 13(2), 2012.

[210] Hatem A Fayed and Amir F Atiya. Speed up grid-search for parameter selection of support vector machines. *Applied Soft Computing*, 80:202–210, 2019.

[211] Qiujun Huang, Jingli Mao, and Yong Liu. An improved grid search algorithm of svr parameters optimization. In *2012 IEEE 14th International Conference on Communication Technology*, pages 1022–1026. IEEE, 2012.

[212] Iwan Syarif, Adam Prugel-Bennett, and Gary Wills. Svm parameter optimization using grid search and genetic algorithm to improve classification performance. *Telkomnika*, 14(4):1502, 2016.

[213] Giuseppe Lacidogna, Gianfranco Piana, Federico Accornero, and Alberto Carpinteri. Multi-technique damage monitoring of concrete beams: acoustic emission, digital image correlation, dynamic identification. *Construction and Building Materials*, 242:118114, 2020.

[214] Preetum Nakkiran, Gal Kaplun, Yamini Bansal, Tristan Yang, Boaz Barak, and Ilya Sutskever. Deep double descent: Where bigger models and more data hurt. *Journal of Statistical Mechanics: Theory and Experiment*, 2021(12):124003, 2021.

[215] Sinno Jialin Pan, Ivor W Tsang, James T Kwok, and Qiang Yang. Domain adaptation via transfer component analysis. *IEEE transactions on neural networks*, 22(2):199–210, 2010.

[216] Diego A Tibaduiza, Luis Eduardo Mujica, and Jose Rodellar. Damage classification in structural health monitoring using principal component analysis and self-organizing maps. *Structural Control and Health Monitoring*, 20(10):1303–1316, 2013.

[217] Thomas Grubinger, Adriana Birlutiu, Holger Schöner, Thomas Natschläger, and Tom Heskes. Domain generalization based on transfer component analysis. In *International Work-Conference on Artificial Neural Networks*, pages 325–334. Springer, 2015.

[218] Yaoliang Yu and Csaba Szepesvári. Analysis of kernel mean matching under covariate shift. *arXiv preprint arXiv:1206.4650*, 2012.

[219] Jinane Harmouche, Claude Delpha, and Demba Diallo. Incipient fault detection and diagnosis based on kullback–leibler divergence using principal component analysis: Part i. *Signal processing*, 94:278–287, 2014.

[220] Arthur Gretton, Karsten M Borgwardt, Malte J Rasch, Bernhard Schölkopf, and Alexander Smola. A kernel two-sample test. *The Journal of Machine Learning Research*, 13(1):723–773, 2012.

[221] Bernhard Schölkopf. The kernel trick for distances. *Advances in neural information processing systems*, 13, 2000.

[222] Giona Matasci, Michele Volpi, Mikhail Kanevski, Lorenzo Bruzzone, and Devis Tuia. Semisupervised transfer component analysis for domain adaptation in remote sensing image classification. *IEEE Transactions on Geoscience and Remote Sensing*, 53(7):3550–3564, 2015.

[223] Keith Worden, Graeme Manson, and Nick RJ Fieller. Damage detection using outlier analysis. *Journal of Sound and vibration*, 229(3):647–667, 2000.

[224] TC Huang. The effect of rotatory inertia and of shear deformation on the frequency and normal mode equations of uniform beams with simple end conditions. 1961.

[225] JA Loya, L Rubio, and J Fernández-Sáez. Natural frequencies for bending vibrations of timoshenko cracked beams. *Journal of sound and vibration*, 290(3-5):640–653, 2006.

[226] Alan Showkati, Hossein Salari-rad, and Mousa Hazrati Aghchai. Predicting long-term stability of tunnels considering rock mass weathering and deterioration of primary support. *Tunnelling and Underground Space Technology*, 107:103670, 2021.

[227] Fei Ye, Nan Qin, Xing Liang, Aohui Ouyang, Zhou Qin, and Enjie Su. Analyses of the defects in highway tunnels in china. *Tunnelling and Underground Space Technology*, 107:103658, 2021.

[228] Kang-Hyun Kim, No-Hyeon Park, Ho-Jong Kim, and Jong-Ho Shin. Modelling of hydraulic deterioration of geotextile filter in tunnel drainage system. *Geotextiles and Geomembranes*, 48(2):210–219, 2020.

[229] Cheng-lu Gao, Zong-qing Zhou, Wei-min Yang, Chun-jin Lin, Li-ping Li, and Jing Wang. Model test and numerical simulation research of water leakage in operating tunnels passing through intersecting faults. *Tunnelling and Underground Space Technology*, 94:103134, 2019.

[230] Leijin Xiong, Dingli Zhang, and Yu Zhang. Water leakage image recognition of shield tunnel via learning deep feature representation. *Journal of Visual Communication and Image Representation*, 71:102708, 2020.

[231] Zhang Xuefu and Zhang Yaonan. Study on a new-styled measure for treating water leakage of the permafrost tunnels. *Tunnelling and underground space technology*, 21(6):656–667, 2006.

[232] ITA Working Group on Maintenance et al. Report on the damaging effects of water on tunnels during their working life. *Tunnelling and underground space technology*, 6(1):11–76, 1991.

[233] Yanbin Luo and Jianxun Chen. Research status and progress of tunnel frost damage. *Journal of Traffic and Transportation Engineering (English Edition)*, 6(3):297–309, 2019.

[234] WL Wang, TT Wang, JJ Su, CH Lin, CR Seng, and TH Huang. Assessment of damage in mountain tunnels due to the taiwan chi-chi earthquake. *Tunnelling and underground space technology*, 16(3):133–150, 2001.

[235] Graham Parkinson and Csaba Ékes. Ground penetrating radar evaluation of concrete tunnel linings. In *12th international conference on ground penetrating radar, Birmingham, UK*, volume 11, 2008.

[236] G Grandjean, JC Gourry, and A Bitri. Evaluation of gpr techniques for civil-engineering applications: study on a test site. *Journal of applied geophysics*, 45(3):141–156, 2000.

[237] Gokhan Kilic and Levent Eren. Neural network based inspection of voids and karst conduits in hydro–electric power station tunnels using gpr. *Journal of Applied Geophysics*, 151:194–204, 2018.

[238] Ch Trela, Th Kind, and Marcus Schubert. Detection of air voids in concrete by radar in transmission mode. In *2015 8th International Workshop on Advanced Ground Penetrating Radar (IWAGPR)*, pages 1–4. IEEE, 2015.

[239] Siow Wei Jaw and Mazlan Hashim. Accuracy of data acquisition approaches with ground penetrating radar for subsurface utility mapping. In *2011 IEEE International RF & Microwave Conference*, pages 40–44. IEEE, 2011.

[240] Wenbin Shao, Abdesselam Bouzerdoum, Son Lam Phung, Lijun Su, Buddhima Indraratna, and Cholachat Rujikiatkamjorn. Automatic classification of ground-penetrating-radar signals for railway-ballast assessment. *IEEE Transactions on Geoscience and Remote Sensing*, 49(10):3961–3972, 2011.

[241] Peter A Torrione, Kenneth D Morton, Rayn Sakaguchi, and Leslie M Collins. Histograms of oriented gradients for landmine detection in ground-penetrating radar data. *IEEE transactions on geoscience and remote sensing*, 52(3):1539–1550, 2013.

[242] Allen G Davis, Malcolm K Lim, and Claus Germann Petersen. Rapid and economical evaluation of concrete tunnel linings with impulse response and impulse radar non-destructive methods. *NDT & E International*, 38(3):181–186, 2005.

[243] E Cardarelli, C Marrone, and L Orlando. Evaluation of tunnel stability using integrated geophysical methods. *Journal of Applied Geophysics*, 52(2-3):93–102, 2003.

[244] HyunJun Jo, Yong-Ho Na, and Jae-Bok Song. Data augmentation using synthesized images for object detection. In *2017 17th International Conference on Control, Automation and Systems (ICCAS)*, pages 1035–1038. IEEE, 2017.

[245] Zhun Zhong, Liang Zheng, Guoliang Kang, Shaozi Li, and Yi Yang. Random erasing data augmentation. In *Proceedings of the AAAI conference on artificial intelligence*, volume 34, pages 13001–13008, 2020.

[246] Zeshan Hussain, Francisco Gimenez, Darvin Yi, and Daniel Rubin. Differential data augmentation techniques for medical imaging classification tasks. In *AMIA annual symposium proceedings*, volume 2017, page 979. American Medical Informatics Association, 2017.

[247] Tools Concepts. Techniques to build intelligent systems. *Sebastopol, CA, USA*, 2017.

[248] A Sai Bharadwaj Reddy and D Sujitha Juliet. Transfer learning with resnet-50 for malaria cell-image classification. In *2019 International Conference on Communication and Signal Processing (ICCSP)*, pages 0945–0949. IEEE, 2019.

[249] Kaiming He, Xiangyu Zhang, Shaoqing Ren, and Jian Sun. Deep residual learning for image recognition. In *Proceedings of the IEEE conference on computer vision and pattern recognition*, pages 770–778, 2016.

[250] Olga Russakovsky, Jia Deng, Hao Su, Jonathan Krause, Sanjeev Satheesh, Sean Ma, Zhiheng Huang, Andrej Karpathy, Aditya Khosla, Michael Bernstein, et al. Imagenet large scale visual recognition challenge. *International journal of computer vision*, 115(3):211–252, 2015.

[251] John Markoff. For web images, creating new technology to seek and find. *New York Times*, 2012.

[252] George A Miller. *WordNet: An electronic lexical database*. MIT press, 1998.

[253] Jia Deng, Wei Dong, Richard Socher, Li-Jia Li, Kai Li, and Li Fei-Fei. Imagenet: A large-scale hierarchical image database. In *2009 IEEE conference on computer vision and pattern recognition*, pages 248–255. Ieee, 2009.

[254] Antonino Ventura. *Estrazione di relazioni semantiche frequenti tra oggetti in immagini segmentate*. PhD thesis, Politecnico di Torino, 2020.

[255] S Allen Broughton and Kurt Bryan. *Discrete Fourier analysis and wavelets: applications to signal and image processing*. John Wiley & Sons, 2018.

[256] Jae S Lim. Two-dimensional signal and image processing. *Englewood Cliffs*, 1990.

[257] Robert Fisher, Simon Perkins, Ashley Walker, and Erik Wolfart. Hypermedia image processing reference. *England: John Wiley & Sons Ltd*, pages 118–130, 1996.

[258] Rushi Longadge and Snehalata Dongre. Class imbalance problem in data mining review. *arXiv preprint arXiv:1305.1707*, 2013.

[259] Juan D Rodriguez, Aritz Perez, and Jose A Lozano. Sensitivity analysis of k-fold cross validation in prediction error estimation. *IEEE transactions on pattern analysis and machine intelligence*, 32(3):569–575, 2009.

[260] KA Ross, CS Jensen, R Snodgrass, CE Dyreson, CS Jensen, R Snodgrass, and L Chen. Cross-validation. encyclopedia of database systems, 2009.

[261] James Gareth, Witten Daniela, Hastie Trevor, and Tibshirani Robert. *An introduction to statistical learning: with applications in R*. Spinger, 2013.